# Evaluating the thermal resistance of a vacuum insulation panel wall assembly containing thermal bridges using industry standard calculation methods and numerical simulation techniques

by

Travis V. Moore

A thesis submitted to the Faculty of Graduate and Postdoctoral Affairs in partial fulfillment of the requirements for the degree of

Master of Applied Science

in

Mechanical Engineering

Carleton University
Ottawa, Ontario

## Abstract

This thesis investigates the accuracy of industry standard calculation methods, and two and three-dimensional numerical simulation techniques, to predict the thermal resistance of a wall assembly containing vacuum insulation panels (VIPs) and thermal bridges. The calculation methods and numerical simulations were used to predict the thermal resistance of a wall assembly that was tested in a guarded hot box. The calculation methods and two-dimensional simulation scenarios which did not include VIP edge thermal bridges resulted in a minimum overestimation of 38%. Accounting for the thermal bridges using the average joint width between panels reduced the minimum overestimation to 13% (modified zone calculation method) and 20% (two-dimensional simulations). The three-dimensional simulations overestimated the thermal resistance by 14%. Overall, the most reliable predictions of thermal resistance were determined through 3D simulations and the modified zone method in combination with the thermal bridge effect due to the average joint width between VIPs.

## Acknowledgements

First and foremost, I would like to thank my family for supporting me. To my wife, Heidi, you are my most steadfast supporter, never wavering in your belief that this is something I could and should do. Your diligence and dedication to your own degree inspired me to new levels of dedication required to complete this thesis. Thank you to my children, Charlotte and Logan, both of you have shared your dad with a computer screen for the entirety of your known lives, as you were both born during the pursuit of this degree.

I also wish to thank my colleagues Michael, and Nathan. Nathan, you were the person who inspired me to start this journey, and I thank you for it. Michael, thank-you for your support and belief in me throughout my career at NRC and your willingness to trust me with many critical projects over the years; you have truly made this thesis possible.

To my other colleagues at NRC, Carsen, and Michal, thank you for your willingness to provide insight and take time out of your lives to discuss and help me complete this.

Finally, to my graduate supervisors, Ian and Cynthia, I sincerely thank both of you for your graciousness in taking on a part time student who you barely knew, and your patience in helping me find a path to complete this thesis.

# Table of Contents

## List of Tables

## List of Figures

## Nomenclature

| Symbol | Description | Units |
|---|---|---|
| $\lambda$ | Thermal conductivity of the material | W/mK |
| $U$ | Thermal transmittance | W/m$^2$K |
| $\psi(d)$ | Linear thermal transmittance of the joint | W/mK |
| $L$ | Length | m |
| $\chi$ | Point thermal transmittance | W/K |
| $A$ | Surface area normal to direction of heat transfer | m$^2$ |
| $d$ | Depth | m |
| $pt$ | Perimeter of the panel | m |
| $Q$ | Energy transferred due to heat transfer | W |
| $T$ | Temperature | °C |
| $I$ | Current supplied to the heater | A |
| $V$ | Voltage supplied to the heater | V |
| $W$ | Effective zone width | m |
| $zf$ | Zone factor | |
| $R$ | Thermal resistance | m$^2$K/W |
| $p$ | Weighting factor | m$^2$K/W |
| $w$ | Steel stud flange width | mm |
| $st$ | Steel stud spacing | mm |
| $dy$ | Distance between nodes in y direction | m |
| $h$ | Average surface heat flux coefficient | W/m$^2$K |

| | | |
|---|---|---|
| $r$ | Thermal resistivity | mK/W |
| $q"$ | Heat flux | W/m$^2$ |
| $Ra$ | Rayleigh number | |
| $g$ | Gravity | m/s$^2$ |
| $\beta$ | Thermal expansion coefficient | 1/K |
| $\nu$ | Kinematic viscosity of air | m/s$^2$ |
| $Pr$ | Prandtl number | |

## Subscripts

| | |
|---|---|
| app | apparent |
| eff | effective |
| cv | convection heat transfer in the gas phase of VIP |
| sd | conduction heat transfer in the solid phase of VIP |
| g | conduction heat transfer in the gas phase of VIP |
| r | Radiation through VIP core |
| cop | Centre of panel |
| t | Total or combined |
| o | Clear field |
| cl | Characteristic length |
| sf | Stud flange |
| sp | Specimen |
| in | Input |
| fl | Flanking loss |

| | |
|---|---|
| $mb$ | Metering box |
| $amb$ | Ambient air |
| $h$ | Interior |
| $c$ | Exterior |
| $s$ | specimen surface average |
| $y$ | Surface element y direction |
| $y-1$ | Element previous to the surface element in y direction |
| $x$ | Surface element x direction |
| $x-1$ | Element previous to the surface element in x direction |
| $\infty$ | Ambient |
| $max$ | Maximum |
| $min$ | Minimum |
| $air\ to\ air$ | Air to air |
| $surf\ to\ surf$ | Surface to surface |
| $A$ | Exterior sheathing combined |
| $ins$ | Cavity insulation |
| $B$ | Interior sheathing |
| $met$ | Steel stud |
| $I$ | Stud flange geometry section |
| $II$ | Stud web depth geometry section |

# 1 Chapter: Introduction

Increasing financial and environmental costs of energy production have resulted in many countries seeking to decrease energy demands in all sectors. Currently in Canada, there has been an increased desire to decrease the country's energy budget, both costly generation, as well as carbon emissions into the atmosphere.

The Canadian government has recently produced the Pan Canadian Framework on Clean Growth and Climate Change (Canada, 2017) to help the world meet the target of limiting greenhouse gas (GHG) emissions as outlined in the Paris Agreement (Nations, 2015). The specific Canadian target outlined in the Framework is a 30% reduction in national greenhouse gas emissions by 2030.

Several sectors were identified in the Framework as areas in which energy savings are required, including reducing the heating and cooling load in buildings. It estimates that 12% of national GHG emissions are accounted for in the heating and cooling of buildings. An even higher 17% is estimated if emissions from electricity production are accounted for in heating and cooling losses.

Reduction of heating and cooling losses in buildings can be accomplished in several ways. The most common method is to increase the thermal resistance of the building envelope. Unless the building has little or no insulation, increasing thermal resistance is usually accomplished through either changing the building insulation to higher performing insulation materials or adding more insulation to the building envelope by increasing the thickness of the walls. Increased wall thickness can present problems for designers, especially when the design incorporates windows, doors and other thin elements that bridge the building envelope. The increased thickness also becomes an issue in areas in which

space is at a premium. Therefore, thin high-performance insulation technologies are likely to see increased use by designers either for retrofit applications, or new build designs where space is at a premium. One thin insulation type that is currently being used in areas in which space is at a premium (such as Europe and Japan) is vacuum insulation panels (VIP) (H.Simmler, 2005).

The VIPs thermal performance is derived from an open cell microporous core which is depressurized to a partial vacuum pressure of ~1 mbar (H.Simmler, 2005). The core is wrapped in a gas barrier envelope which maintains the vacuum in atmospheric conditions. The vacuum condition in the core material essentially eliminates gas convection and conduction heat transfer through the porous core material (Simmler, et al., 2005). Heat transfer is then due to conduction through the solid core material and radiation in the pores. Selection of low solid conductivity core materials and opacifier additives decrease the contributions of the solid conductivity and radiation which further increases the thermal resistance of the VIP.

The quoted potential performance of VIPs is quite remarkable, especially considering the thickness to insulation ratio. It is estimated that most common insulation materials would require 4-5 times the thickness of a VIP to achieve similar insulation capacity (H.Simmler, 2005). However, this claim should be investigated with caution as the quoted performance is idealized as the centre of panel thermal conductivity for VIP's (Van Den Bossche, Moens, Janssens, & Delvoye, 2010). Investigation of the technology indicates that the actual performance of VIPs in an assembly is overestimated if the effect of heat transfer around the perimeter of the panel is not accounted for (Schwab, Stark, Wachtel, Ebert, & Fricke, 2005). The heat transfer rates at the edges of panels (including

joints between panels) are significantly higher than the centre of panel values. This is due to thermal bridges caused by the materials in the gas barrier film and joints having higher lower thermal resistance than the core material. The thermal bridge heat transfer paths are depicted for a representative wall construction containing VIPs in Figure 1.

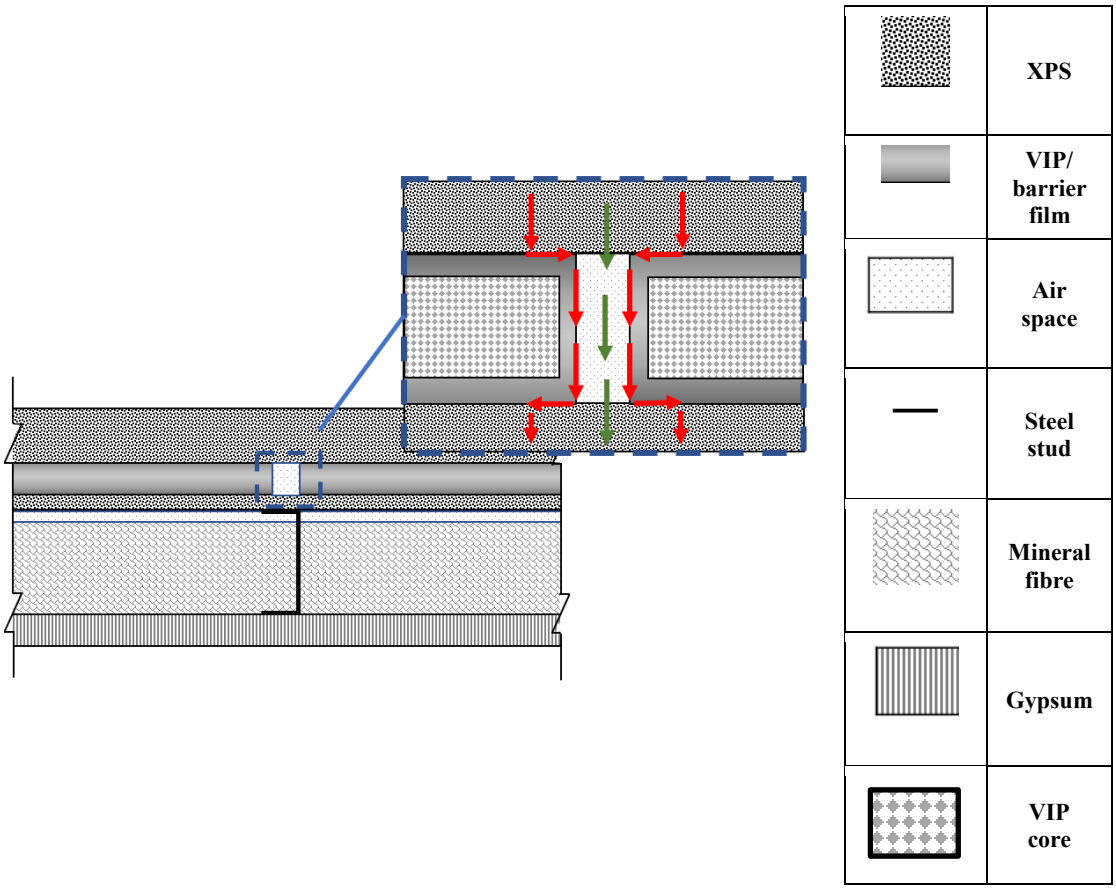


**Figure 1: Sketch depicting the thermal bridges that occur at the edge of the VIP panel and joints between panels in wall assemblies. The red arrows represent heat transferring along the barrier film. The green arrows represent the heat transferring through the air joint. In both cases heat transfer occurs around the VIP core.**

Unfortunately, the best materials to reduce gas transmission across the barrier envelope are metals, which have significantly higher thermal conductivities than the core structure. Optimizing the performance of VIP's requires minimizing the thickness of the metal portions, however this comes at a cost of higher rates of gas and moisture transfer across the barrier. To minimize the metal component in the barrier film it is spray deposited

in several layers, which can leave microscopic gaps in which atmospheric gases are able to permeate over time (Figure 2). It is therefore expected that over time the thermal resistance of a VIP decreases, due to the migration of atmospheric gases across the barrier envelope. Atmospheric gas migration increases the pore pressure of the core material, which increases the heat transfer rate across the pores by increasing gas conduction. Migration of water vapour increases the solid conduction of the core material due to the presence of adsorbed moisture (Brunner & Wakili, 2014). The time over which a VIP maintains thermal performance above a specified value is termed the service life.

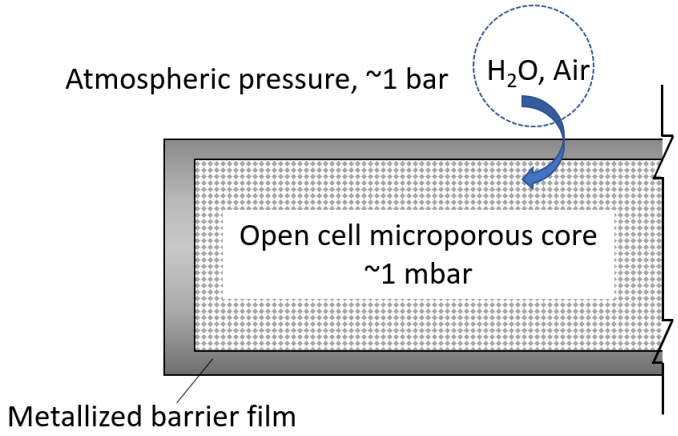


**Figure 2: Representative vacuum insulation panel sketch, depicting the open cell microporous core and barrier envelope. The pressure difference between the atmosphere and the partial vacuum pressure in the core material drives atmospheric gases through microscopic gaps in the metal in the barrier envelope.**

The performance of VIP assemblies has been investigated in several studies to demonstrate the effect of edges on the overall thermal performance. These investigations have been completed using both field monitoring as well as laboratory testing using a guarded hot box (GHB) test apparatus. The edge and joint effect on the thermal performance of VIPs has also been investigated on smaller scale tests using a heat flow meter apparatus. Simulations have also been conducted which account for and demonstrate

the increased heat transfer at the edge effect on overall VIP thermal performance (H.Simmler, 2005; Brunner, Stahl, & Wakili, Single and double layered vacuum insualtion panels of the same thickness comparison, 2012; Lorenzati, Fantucci, Capozzoli, & Perino, 2014; Tenpierik, van der Spoel, & Cauberg, 2007; Van Den Bossche, Moens, Janssens, & Delvoye, 2010). These studies indicate that the heat transfer effects due to thermal bridges in VIPs cause significant lateral heat transfer effects which can not be captured with one-dimensional calculation methods. Studies on thermal bridges have also indicated that using one-dimensional calculation methods to determine the thermal resistance of wall assemblies containing thermal bridges can lead to significant overestimation (ISO, 2007b; Morris and Hershfield Ltd., 2011). However, regulatory energy codes, such as the National Energy Code of Canada for Buildings (NRC, 2016), reference one dimensional calculation methods as acceptable methods to determine the thermal resistance of wall assemblies.

The objective of this thesis is to determine the accuracy of using industry standard one-dimensional calculation methods, and two and three-dimensional numerical simulations to determine the steady state thermal resistance of a wall assembly containing VIPs for building envelope design. Additionally, the thesis investigates methods to increase the accuracy of the calculation and numerical simulation methods by using VIP effective thermal conductivities which account for the increased heat transfer rates at the edges of the panel due to the metallized barrier film and joint thermal bridges.

To accomplish this, a representative wall assembly containing VIPs was built, and the steady state thermal response of the wall assembly was determined using a GHB. Thereafter, the steady state thermal response of the wall assembly was characterized using industry standard calculation methods and two and three dimensional numerical

simulations. The accuracy of each calculation method in predicting the thermal resistance of the wall assembly was then compared with the GHB test results.

The VIPs investigated in this thesis were at the beginning of their service life. The rate of decrease in thermal performance of VIPs due to gas migration across the barrier envelope is not considered, and therefore service life of the wall assembly is not estimated.

## 1.1 Thesis outline

The work in this thesis is divided into the following sections: the literature review (which defines the calculation and experimental methods used to characterize the VIP wall performance), the results of the experiments, the results of the calculation methods, comparison of the calculation results to the experiment results, and conclusions and future work. Uncertainties of the experiment and calculation results are also analyzed and presented in the results sections.

This thesis is divided into the following chapters:

1 Chapter: Introduction

2 Chapter: Literature review and background

3 Chapter: Results of guarded hot box characterization experiments

4 Chapter: Guarded hot box experiment set up and results

5 Chapter: Guarded hot box experiment uncertainty

6 Chapter: Industry standard calculation method results

7 Chapter: Two and three-dimensional numerical simulations set up

8 Chapter: Numerical simulation results and uncertainty

9 Chapter: Conclusions and future work

# 2 Chapter: Literature review and background

The literature review was focused on three principal areas: vacuum insulation panel (VIP) use in the building sector, guarded hot box testing, and the industry standard calculation methods available for building envelope designers to determine thermal resistance of wall assemblies.

## 2.1 Vacuum insulation panels

This section presents background information on the requirements of VIP components in the building sector, followed by experiments that have been used to demonstrate and characterize the performance of VIPs in building envelopes. This includes the methods by which the edge and joint effects can be determined for use in industry standard and numerical simulation calculation methods.

### 2.1.1 Vacuum insulation technology for building applications

Vacuum technology for insulation purposes has been used since the early 1900's (Fricke, 2005) . In the earliest use, vacuum technology was utilized by creating a vacuum between the walls of two concentric metal cylinders (Fricke, 2005). The use of the concentric cylinders allowed for the vacuum to be supported by the container walls, with no filler material. This was possible due to the high failure limits of hoop stress in cylindrical objects (Fricke, 2005). Vacuum insulation panels have also been used in other industries to insulate industrial furnaces and freezers. The use of VIPs in these sectors is

not usually applicable to building technologies due to the tightly controlled environments in which these items are built and are operated (H.Simmler, 2005).

The use of cylinders in building envelope design is limited; instead rectangular structures are used. Rectangular structures cannot depend on hoop stress to maintain the structural integrity when a vacuum is applied and as such require a filler or 'core' material (Fricke, 2005) surrounded by an envelope is necessary.

The requirements of a VIP core material are that it is open cell, microporous, with a fractal composition and compressive strength high enough to maintain its shape when under partial vacuum (~1 mbar). The open cell enables the removal of atmospheric gas from the pores during depressurization, which greatly reduces heat transfer due to gas conduction and gas convection. The fractal composition of the solid structure interrupts pathways for solid conduction. The combination of these factors reduces the apparent thermal conductivity of the core material.

Apparent thermal conductivity is defined as the total thermal transmission rate across a material, accounting for combined effects of conductive, radiative, and convective heat transfer (ASTM, 2010). Annex 39 (Simmler, et al., 2005) defines the components of the apparent thermal conductivity ($\lambda_{\mathrm{app}}$) of a VIP with Equation 1.

$$\lambda_{app} = \lambda_{cv} + \lambda_{sd} + \lambda_{g} + \lambda_{r} \qquad \textbf{Equation 1}$$

$\lambda_{cv}$ - convection in the gas phase
$\lambda_{sd}$ - conductivity through the solid phase
$\lambda_{g}$ – conductivity through the gas phase.
$\lambda_{r}$ - radiation

Caution must be taken when using the apparent thermal conductivity in calculations, as representing the radiative and convective heat transfer mechanisms as conduction is only valid for the specific temperature boundary conditions under which the apparent thermal conductivity is determined. This is due to the dependency of radiation and convection heat transfer rates on the surface temperatures of the corresponding faces over which the heat is transferring.

It is generally estimated that a partial vacuum of 1 mbar in the core material reduces contributions of gaseous conduction and convection to negligible values, and the core apparent thermal conductivity is due to radiation (~$1*10^{-3}$ W/mK) and conduction of the solid structure (~$3*10^{-3}$ W/mK) (Simmler, et al., 2005).

The partial vacuum in the core material is maintained in atmospheric conditions by a gas barrier film. The gas barrier film is designed to limit the migration of atmospheric gases and water vapour to the interior of the core material. Unfortunately, currently the best materials for reduction of gas and vapour transmission are metals. The metal in the gas barrier film creates a significant thermal bridge around the edges of the VIP, which decreases the effective thermal conductivity of the VIP. The effective thermal conductivity of the VIP includes the apparent thermal conductivity of the core material, and the contribution of the thermal bridge due to the gas barrier film (Schwab, Stark, Wachtel,

Ebert, & Fricke, 2005). It is conventional in the building industry to relate two and three-dimensional heat transfer effects (such as those occurring at the panel edges) to a one-dimensional heat transfer effect on a uniform surface, and describe this as the 'effective thermal conductivity' of the panel.

### 2.1.2 Vacuum insulated panel performance in the building envelope

While the use of metal decreases the rate of gas transmission across the barrier envelope, it also decreases the thermal performance of the VIP. VIPs have a high centre of panel thermal resistance, however, overall thermal performance of the panels cannot be considered without accounting for the edge thermal bridge effect due to the gas barrier film and joint material between individual VIPs (Van Den Bossche, Moens, Janssens, & Delvoye, 2010; Schwab, Stark, Wachtel, Ebert, & Fricke, 2005; Lorenzati, Fantucci, Capozzoli, & Perino, 2014; Brunner, Stahl, & Wakili, Single and double layered vacuum insualtion panels of the same thickness comparison, 2012; Tenperik & Cauberg, 2007; Wakili, Bundi, & B.Binder, 2004). The centre of panel thermal conductivity is defined as the idealized one-dimensional thermal conductivity through the centre of the panel (far away from the edges) and excludes effects of edges and joints.

Testing has shown that the edge thermal bridge can be dominant in the thermal performance of a VIP system due to the drastic difference between thermal conductivity of the core material (~$4*10^{-3}$ W/mK) and the thermal conductivity of the metal in the barrier film (aluminum ~160 W/mK, steel ~15-17 W/mK) and joint material (Sprengard & Holm, 2014). This discrepancy can result in an 'effective thermal conductivity' of the VIP several

hundred percent higher than the centre of panel value (Schwab, Stark, Wachtel, Ebert, & Fricke, 2005).

Brunner et al. (Brunner, Stahl, & Wakili, 2012) conducted GHB tests to compare two wall assemblies with 40mm of VIP layer thickness. However, one layer consisted of a double layer of 20mm VIPs, and the other consisted of a single 40mm layer of VIPs. The test results indicated that the double layer wall had approximately 13% less thermal transmission than the single layer wall. The increase in performance was attributed to the decreased thermal bridge at the edges of the VIP panel in the double layer VIP wall assembly. The decrease was accomplished by offsetting the second layer of VIPs such that the thermal bridges from the edges and joints did not line up with edges and joints in the second layer. These results demonstrate the importance of designing to minimize VIP edge effects to increase thermal resistance of a wall assembly incorporating VIPs.

### 2.1.3 Vacuum insulated panel effective thermal conductivity due to edge and joint thermal bridge

Accurate calculation of the thermal performance of a wall assembly incorporating VIPs for building design requires accounting for the effective thermal conductivity of a VIP in an assembly, including the edge and joint effects. Although physical testing of VIPs can be used to determine the effective thermal conductivity of individual VIP panels (Alam, 2011; Lorenzati, Fantucci, Capozzoli, & Perino, 2014; Van Den Bossche, Moens, Janssens, & Delvoye, 2010; Wakili, Bundi, & B.Binder, 2004), it is unlikely that building designers will be able to conduct testing on all variety of VIPs they wish to use in a building

design. Therefore, a method is required by which a designer can calculate the effective thermal conductivity of the VIP, and implement it in industry standard calculation methods.

Many small-scale tests and analytical methods have aimed to predict the thermal bridge effects of the joints and edges of VIPs on the effective thermal conductivity of the VIP. Unfortunately, fully characterizing the edge and joint effect on the effective thermal conductivity of a VIP assembly is complex. To fully characterize the effective thermal conductivity the following information would be required of each VIP used in the assembly: the location of the barrier film edge folds, the type of edge fold, gaps between abutting panels which can be filled with air or various insulation types, VIP depth and the core thermal transmittance rate (Van Den Bossche, Moens, Janssens, & Delvoye, 2010).

The most common method to describe a general equation to represent the effective thermal conductivity of a VIP panel including edge thermal bridges from experiments is through the thermal transmittance method. In this method, the thermal transmittance is determined for the edge and joint per unit length, and this value is multiplied by the perimeter length of the VIP to determine the effective thermal conductivity of the panel.

The thermal transmittance method has been used to determine performance of wall assemblies incorporating thermal bridges through the summation of linear and point transmittances of thermal bridges coupled with opaque wall R-value calculation in several instances. This method is well described by ISO 6946 (ISO, 2007c), ISO 10211 (ISO, 2007a), ISO 14683 (ISO, 2007b), and Morris and Hershfield in ASHRAE RP-1365 (Morris and Hershfield Ltd., 2014; ASHRAE, 2011). The linear and point thermal transmittances are determined through use of benchmarked three-dimensional heat transfer simulation software or GHB testing. The simulation software or tests are used to determine the effects

of thermal bridges by determining the U-value (total thermal transmittance rate) of a structure with and without thermal bridges in place. The difference between the two U-values determines the normalized linear or point transmittance for that thermal bridge type in the specific wall configuration simulated. The general equation referenced for a wall assembly containing thermal bridges is presented in Equation 2. The thermal transmittance method is used in this thesis to determine the effective thermal conductivity of the VIP, considering heat transfer due to the thermal transmittance of the barrier foil and joint material at the edges.

$$U_{\mathrm{t}} = \frac{\sum(\psi(d) * L) + \sum \chi}{A} + U_o \qquad \textbf{Equation 2}$$

$U_{\mathrm{t}}$ – total thermal transmittance including anomalies [W/(m$^2$K)]
$\psi(d)$ – linear thermal transmittance [W/(mK)]
$L$ – characteristic length of linear transmittance
$\chi$ – point transmittance [W/K]
$A$ –surface area normal to direction of heat transfer[m$^2$]
$U_o$ – clear field thermal transmittance (assembly) [W/(m$^2$K)]

The equation for the effective thermal conductivity of VIPs using the thermal transmittance approach is shown in Equation 3 (Wakili, Bundi, & B.Binder, 2004). Corners

are considered to create a negligible thermal bridge compared to the edges, so are not accounted for in the equation (Tenperik & Cauberg, 2007).

$$\lambda_{\text{eff}} = \lambda_{\text{cop}} + \Delta_{\text{edge}} = \lambda_{\text{cop}} + \psi(d) * d * \frac{pt}{A} \qquad \textbf{Equation 3}$$

$\lambda_{\text{cop}}$ – centre of panel thermal conductivity (W/mK)
$\psi(d)$ – linear thermal transmittance of the joint (W/mK)
$d$ – thickness of the VIP (m)
$A$ – surface area perpendicular to the direction of heat transfer ($m^2$)
$pt$ - perimeter of the panel (m)

Equation 3 is used to determine the effective thermal conductivity of the VIPs studied in this thesis to increase the accuracy of industry standard calculation methods in predicting the thermal transmittance of a wall assembly containing VIPs. The linear thermal transmittances used in this thesis found in literature for differing VIP joints are provided in the following paragraphs.

Wakili et al. (Wakili, Bundi, & B.Binder, 2004) tested VIP's with fumed silica cores and various barrier films made up of both multiple layer metallized films and metal foils for both centre of panel thermal conductivity and effective thermal conductivity of the panel. The centre of panel values were determined for 500mm x 500mm panels and the edge effect was determined for two 500mm x 250mm panels.

The thermal transmittance of the edge for two panels with different thickness of aluminum in the metalized polymer barrier are presented in Table 1. These results were determined from a numerical simulation which was benchmarked to the test results, for a panel of 1m by 1m. The numerical modelling was conducted by combining the multiple

thin barrier layers (metal and polymers) into a single layer, and therefore authors caution the use of these results for VIPs of different barrier foil types.

**Table 1: Thermal transmittance of VIP edge as per Wakili et al. (Wakili, Bundi, & B.Binder, 2004).**

| VIP barrier | Edge thermal transmittance $\psi(d)$ [W/mK] |
|---|---|
| **Aluminum 90nm total thickness** | 6.96 (±1.63) $*10^{-3}$ |
| **Aluminum 300nm total thickness** | 9.19 (±1.63) $*10^{-3}$ |

Other uncertainties associated with these results occur due to the air gaps present between abutting VIP's during the edge heat transfer testing. Measurements of the air gaps are not described in the work. Instead the air gaps were 'adjusted' in the numerical simulations to tune the numerical results to the experiment results. This could cause errors in using these values to assess VIP designs, as variations in the air gap would change the linear thermal transmittance of the edge and joint.

Tenperik et al. (Tenperik & Cauberg, 2007) present work on a method to analytically calculate the corresponding edge thermal transmittance of VIPs. The analytical equation assumes steady state heat transfer using assumed boundary conditions. The analytical model uses the following inputs to calculate the edge effect: the heat transmission coefficient at the boundary surface, the thickness of the VIP, the thickness of the laminate, the thickness of the laminate at the panel edge and the thermal conductivity of the laminate. This model assumes that the centre of panel thermal conductivity is equal to zero; therefore, it only applies while the ratio of the centre of panel to the edge thermal conductivities is very high. The analytical equation is compared to numerical modelling

results and the accuracy is claimed at 5%. However, no experimental comparisons are completed. The model does not account for air gaps that occur between two abutting VIPs.

The details required regarding the laminate were not available for the VIP's investigated in this thesis, and as such Tenperik's analytical equation was not used to determine effective thermal conductivity for the calculation methods. Nonetheless it is a method that could be used to characterize the thermal bridge due to barrier foil at the edge of a VIP panel, if details of the barrier film are known.

Van Den Bossche et al. (Van Den Bossche, Moens, Janssens, & Delvoye, 2010) provide a review of the work completed by Wakili, Tenperik and many others on quantifying the effective thermal conductivity of VIPs when considering edge thermal bridges. The work conducts experiments to both evaluate the accuracy of the analytical equations proposed by Tenperik and to validate their own numerical heat transfer model for quantifying effective thermal conductivity of VIPs. The experimental method consisted of evaluating the contribution of the gas barrier film to the effective thermal conductivity by separately evaluating the VIP and the barrier film. This was completed by enveloping XPS (extruded polystyrene) panels of known thermal conductivity with the same barrier foil as that on the VIPs being tested. Testing was conducted on both XPS wrapped with and without the barrier foil to determine the thermal transmittance contribution of the barrier foil at edges and centre of panel. Centre of panel and thermal transmittance of edge values were also reported. For both XPS and VIP experiments, the air gap was varied and results determined that models which do not take account of the air gap between abutting VIPs are not reliable. Comparison of the experiment results to Tenperik's equations determined that the equations overestimated the thermal transmittance of the edge values

by approximately 8% for a 20mm thick panel and 23% for a 30mm thick panel. The thermal transmittance of the edge for the VIPs measured in this work was 0.007 W/mK, which included the thermal transmittance due to a 4mm air space between panels.

Lorenzati et al. (Lorenzati, Fantucci, Capozzoli, & Perino, 2014) evaluated 20mm VIPs with three different metallized barriers and four different materials in the joint between abutting VIPs. The joints evaluated included air, XPS, MDF and rubber. The linear thermal transmittance of the edge and joints for each case were determined using a heat flow meter apparatus. The linear thermal transmittance of various air gap joint widths, plus the edge barrier foil determined by Lorenzati et al. are presented in Table 2.

**Table 2: Linear transmittance of VIP edge accounting for air gap thickness (Lorenzati, Fantucci, Capozzoli, & Perino, 2014).**

| Air gap thickness (mm) | $\psi(d)$ (W/mK) |
|---|---|
| 1.97 | 0.0255 |
| 3.47 | 0.0284 |
| 5.6 | 0.0391 |
| 6.67 | 0.0519 |

For application to various VIP sizes and air gap widths, the results were normalized by perimeter to area ratio. Normalized results for a VIP measuring 600mmx1200mm (the size used in the wall assembly investigated in this thesis) are presented in Table 3.

**Table 3: Lorenzati et al. (Lorenzati, Fantucci, Capozzoli, & Perino, 2014) edge effect on overall thermal conductivity of VIPs.**

| Air gap thickness (mm) | % increase on $\lambda_{cop}$ when including edge effects |
|---|---|
| 1.97 | 22% |
| 3.47 | 24% |
| 5.6 | 30% |
| 6.67 | 36% |

These results, in combination with measurements of the air gaps between VIP panels in the wall assembly investigated in this thesis, were used to approximate the effective thermal conductivity of the combined VIP and air joint layer in the wall assembly. The accuracy of using this method is evaluated by comparing industry standard calculation methods and numerical simulations for determining thermal resistance of wall assemblies to GHB test results.

## 2.2 Guarded hot box test method

The accuracy of using industry standard calculation methods, as well as two and three-dimensional heat transfer simulations, to determine the thermal transmittance of a wall assembly containing VIPs was evaluated by comparing the calculated results to results of a GHB test. A GHB is a test apparatus which subjects a wall assembly to a steady state temperature difference and determines the corresponding heat transfer rate through the specimen. The temperature difference and heat transfer rate measured in the GHB test are

used to calculate the thermal resistance of the wall assembly. The GHB used in this thesis was is owned by and resides at the National Research Council Canada, in Ottawa Ontario. This GHB has been extensively used in the past to conduct heat transfer research on walls and windows (Brown & Stephenson, 1993; Brown & Ullett, 1992; Maref, et al., 2012; Bowen & Solvason, 1987; Simko, Elmahdy, & Collins, 1998; Brown & Schwartz, 1987).

**Figure 3: GHB at National Research Council Canada.**

This section describes the use of GHBs in evaluating the thermal transmittance of wall assemblies, calibration methods, the GHB apparatus, and the ASTM C1363 (ASTM, 2013) test method.

### 2.2.1 Guarded hot box use for developing and validating calculation methods

Due to the expense of physical testing significant work has been conducted to develop calculation methods which predict the thermal performance of building components and assemblies. Calculation methods can either be developed from first principles, or as correlations based on laboratory tests. Typically, the laboratory tests used to develop correlations or validate the calculation methods are completed in a GHB test apparatus.

Ullet et al. (J. M. Ullet, 1995) used a GHB to compare parallel path and isothermal planes calculation methods to GHB test results for steel stud walls. The parallel path and isothermal planes calculation methods are described in the industry standard calculation methods section. The results of the GHB testing were used to determine an averaging technique to describe the thermal performance of wall assemblies containing steel studs.

Doran & Gorgolewski (S. Doran, 2002; Gorgolewski, 2007) developed a method for BRE 465 to calculate the effect of steel studs on the thermal resistance of wall assemblies, and compared it to tests completed in a GHB. This method is also further described in the industry standard calculation method section.

Kosny (Kosny, 1995) developed the modified zone method to calculate thermal resistances of wall assemblies that contain steel stud assemblies, by comparing it to a series of GHB tests. The results from the GHB testing were used to determine an 'effective zone' over which the steel stud influences the thermal performance of the wall assembly.

Morris and Hershfield (Morris and Hershfield Ltd., 2011; 2014) used GHB testing to validate three-dimensional heat transfer simulation software used to determine thermal transmittance of thermal bridges in buildings. The software was used to develop a catalogue of thermal transmittance values for thermal bridges in a variety of wall assembly types. The thermal transmittances can be used in conjunction with the thermal transmittance method to determine the effective thermal resistance of building envelopes for whole building energy simulation software. The thermal transmittance method has also been compared with GHB tests in several ISO standards (ISO, 2007a; 2007b; 2007c).

Energy codes (ASHRAE, 2016; NRC, 2016) refer to GHB as a direct method for characterizing thermal resistance of building envelopes. The energy codes also require that

any calculation methods used should be validated with GHB test results. Additionally, it is recognized that physical testing of assemblies using a GHB is required to characterize thermal performance of building envelopes when calculation methods do not yet exist, especially in the case of new or novel insulation technologies.

These examples demonstrate the validity of using GHB test results to assess the accuracy of thermal performance calculation methods, as was completed in this thesis.

### 2.2.2 ASTM C1363

The GHB test method followed in this thesis was ASTM C1363 (ASTM, 2013). This test method defines calibration and characterizations that are required to produce reliable GHB results. The characterization tests are detailed in the following sections. Although the type of measurements and information gathered from an ASTM C1363 test may vary, a general test for any specimen is conducted in the following sequence:

1. Specimen is installed into the insulated mask, taking care to ensure that the wall assembly is sealed to the specimen mask such that mass exchange between the metering box and the cold side chamber is not possible.
2. Specimen surfaces (both warm and cold sides) are instrumented with thermocouples. The pattern of thermocouples needs to be specifically designed to capture the temperature variations that could occur across the specimen surface.
3. Metering box and room side chambers are then sealed to the interior side of the specimen.
4. Temperature control in each chamber is then initiated. The control setpoints consist of room side and metering box air temperatures of 21°C, and cold side

air temperatures of -20°C, and -35°C in two separate tests. Air temperature is monitored in each chamber via thermocouples suspended in the air, approximately 175 mm from the specimen surfaces.

5. The apparatus is monitored until steady state thermal conditions (ASTM C168) have occurred. For the testing in this thesis steady state was assumed when the average sensor readings (heat input to metering box, surface temperature thermocouples, air temperature thermocouples) over three separate consecutive six-hour periods did not vary by more than the standard deviation of the sensors.
6. At steady state conditions, the sensors are monitored for a period of six hours, and calculations are completed based on the average data for each sensor over that six-hour period.

The following sections describe the GHB apparatus and characterization experiment method used in this thesis. Additionally, the method by which the average surface heat transfer coefficients that occur during the GHB tests are determined is described. The coefficients are used as the boundary conditions in the numerical modelling conducted in this thesis.

### 2.2.3 Guarded hot box

A GHB is a test apparatus designed to determine the effective steady state thermal transmittance rate of a wall assembly by subjecting it to a temperature difference and measuring the heat input required to maintain interior temperature conditions. The steady state thermal transmittance is represented as a one-dimensional value, as the boundary conditions during the test are averaged over the wall surfaces, and the heat transfer is characterized to only include that which occurs through the wall assembly. A schematic of

a GHB is presented in Figure 4. A detailed general description of a GHB is presented in ASTM C1363 (ASTM, 2013); a brief description of the GHB is included in this section.

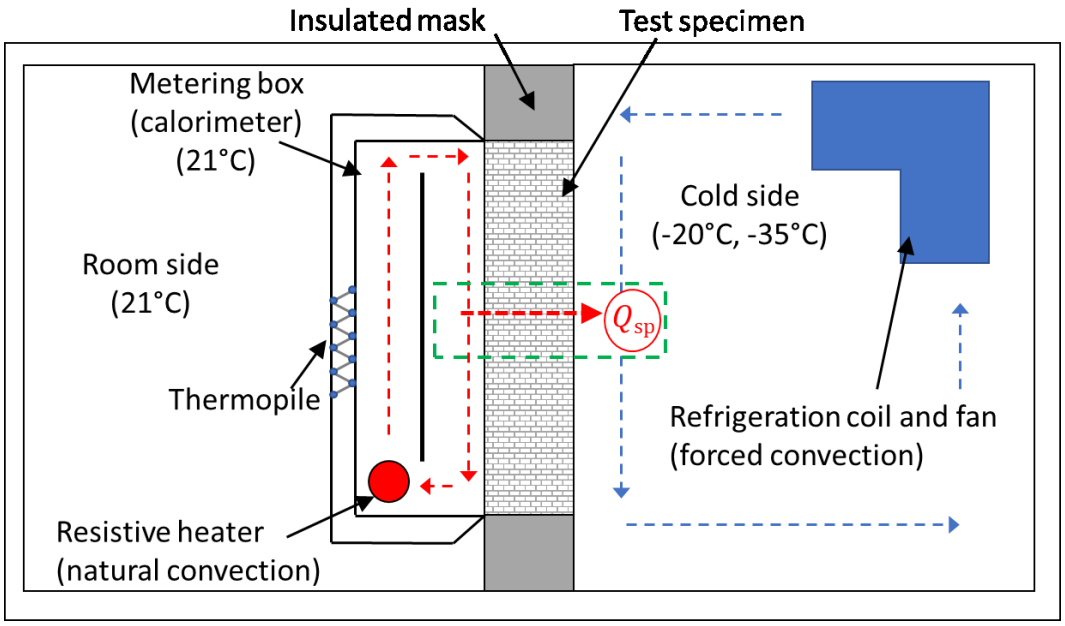


**Figure 4: Guarded hot box test facility.**

A GHB consists of three environmental chambers designed to maintain steady state air temperature conditions on either side of a test specimen, and measure the corresponding heat transfer rate occurring through the wall assembly given that temperature difference. The results from a GHB test are generally given as the effective one-dimensional thermal transmittance rate, or it's reciprocal the effective thermal resistance, of the test specimen for a given temperature difference. The cold side (weather side) of the test apparatus is designed to maintain a steady state cold side air temperature. The GHB used in this thesis maintains the cold side air temperature using a screw pump compressor to cool a refrigerant, which is then pumped through a refrigeration coil inside the cold chamber. A fan circulates air over the coil to achieve the set point temperature. The metering box (calorimeter) is designed to maintain a steady state interior air temperature and measure

the corresponding heat input required to maintain this condition. The room side (warm side) is designed to maintain steady state conditions which match those maintained on the interior of the metering box. Ideally this creates an isothermal boundary between the metering box and the room side. A thermopile is wired between the interior (specimen side) and exterior (room side) surfaces of the metering box (Figure 4). A thermopile is a set of thermocouples wired in series which generate a voltage when subjected to a temperature difference through the thermoelectric effect. The voltage generated by the thermopile is minimized during a test to ensure as close to isothermal conditions between the room side air and metering box air. The thermocouple in the GHB used in this thesis consists of twenty thermocouples wired in series, with the nodes spread out to account for all surfaces of the metering box.

The effective one-dimensional thermal resistance rate is expressed in two forms: the “air to air” effective thermal resistance, or the “surface to surface” effective thermal resistance. An illustration demonstrating the “air to air” and “surface to surface” thermal resistances is shown in Figure 5.

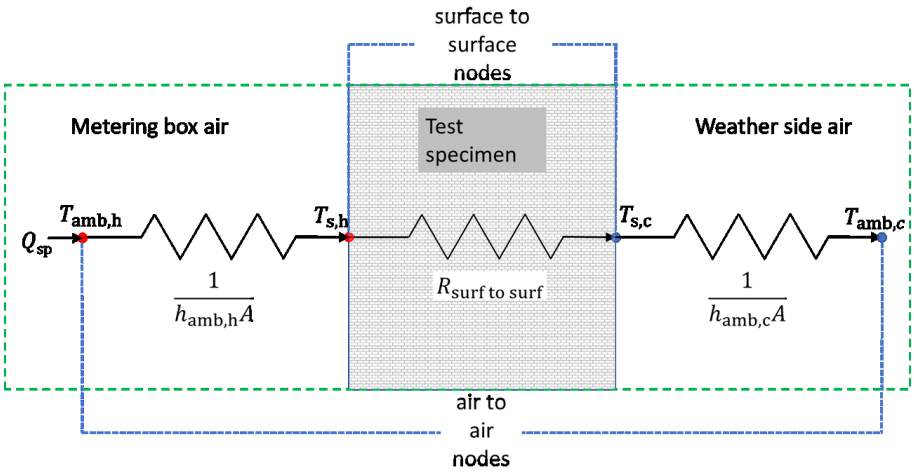


**Figure 5: Schematic of "air to air" and "surface to surface" thermal transmittance rates.**

The "air to air" effective thermal resistance is the thermal resistance of the wall assembly including the average thermal resistance of the air films on each side of the specimen. The equation corresponding to the "air to air" thermal resistance is presented in Equation 4.

$$R_{\text{air to air}} = \frac{A(T_{\text{amb,h}} - T_{\text{amb,c}})}{Q_{\text{sp}}} \qquad \textbf{Equation 4}$$

$Q_{\text{sp}}$ – heat transfer through the test specimen due to the temperature difference [W].
$A$ - specimen surface area perpendicular to the direction of heat transfer [$m^2$]
$T_{\text{amb,h}}$ - metering box air temperature [°C]
$T_{\text{amb,c}}$ – weather side air temperature [°C]

The "surface to surface" effective thermal resistance determines the thermal resistance based on the average surface temperature of the interior and exterior surfaces of the specimen. From Figure 5 the surface to surface thermal resistance is determined using Equation 5.

$$R_{\text{surf to surf}} = \frac{A(T_{\text{s,h}} - \text{T}_{\text{s,c}})}{Q_{\text{sp}}} \qquad \textbf{Equation 5}$$

$T_{\text{s,h}}$ – average specimen surface temperature on the metering box side [°C]
$T_{\text{s,c}}$ – average specimen surface temperature on the weather side [°C]

For wall assemblies, the more common metric is the "air to air" effective thermal transmittance rate, as the surface temperatures of the specimen are typically too variable to allow the average surface temperature on each side of the specimen to be determined (ASTM, 2013).

The effective thermal transmittance (or effective thermal resistance) represents the summation of all the apparent thermal transmittance rates (combined conduction, radiation and convection effects expressed only as conduction) of each individual material to the assembly thermal transmittance. Therefore, the effective thermal transmittance results for an assembly are accurate only for the temperature conditions specified.

### 2.2.4 Guarded hot box characterizations

The heat transfer paths during a test in a GHB are shown in Figure 6 (ASTM, 2013). The GHB measures the heat transfer through a test specimen, given steady state boundary conditions averaged over the interior (warm) and exterior (cold) surfaces of the specimen. The physical measurements that occur in a GHB test can vary, but at minimum consist of measuring the air temperature in the metering box, the surface temperature of the specimen on the metering box side, the surface temperature of the specimen on the weather side, the air temperature on the cold side, and the heat required to maintain the metering box temperature.

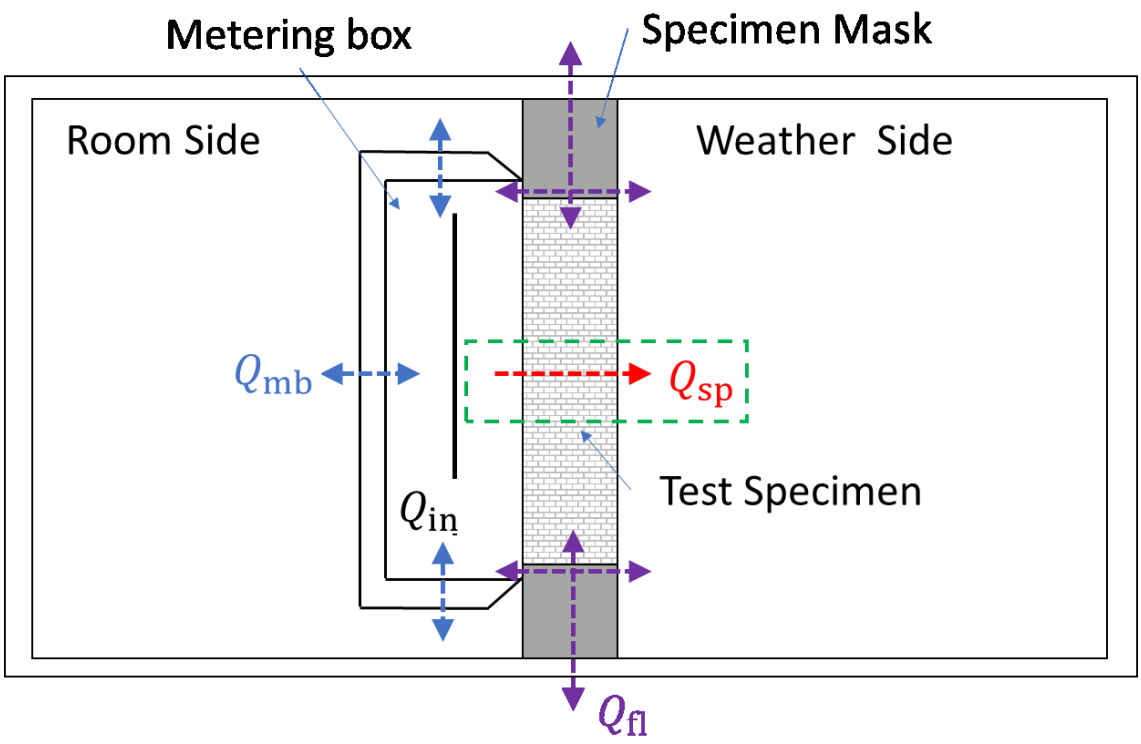


**Figure 6: Heat transfer characterization in a guarded hot box.**

The heat required to maintain the metering box air temperature is provided through a resistive heater, designated by $Q_{in}$ in Figure 6. Ideally all the heat input by the resistive heater would be transferred through the specimen; however, some portion will transfer between the metering box and the room side chamber, and between the specimen and the mask. The blue arrows in Figure 6 represent the heat transfer that can occur through the metering box, referred to as the metering box loss. The green arrows represent the heat transfer that can occur from the specimen to the mask, referred to as the flanking loss.

As stated, the air temperature in the metering box is maintained through a resistive heater. The rate of heat input to the calorimeter is monitored by measuring the voltage dissipation across a calibrated resistor (determines the current being supplied to the heater) in series with the heater, and the voltage drop across the heater itself. Measurement of the

current and voltage being supplied to the heater allows calculation of the wattage being dissipated by the heater through Equation 6.

$$Q_{\text{in}} = I * V \qquad \textbf{Equation 6}$$

$Q_{\text{in}}$ – is the heat input to the metering box [W]
$I$ – current supplied to the heater [A]
$V$ – voltage supplied to the heater [V]

To isolate the heat transfer through the specimen ($Q_{\text{sp}}$) from the total heat being supplied by the heater ($Q_{\text{in}}$), several heat transfer routes are required to be characterized. The heat transfer paths consist of the heat transfer that can occur between the metering box and the guard ($Q_{\text{mb}}$), between the specimen and the mask ($Q_{\text{fl}}$), and finally through the specimen ($Q_{\text{sp}}$). The relationship between these heat flows are shown in Equation **7**. The method by which these heat transfer paths are characterized is presented in the following section.

$$Q_{\text{in}} = Q_{\text{mb}} + Q_{\text{fl}} + Q_{\text{sp}} \qquad \textbf{Equation 7}$$

### 2.2.5 Combined flanking and metering box heat transfer

Although ideally the room side temperature matches the metering box temperature exactly, in practice this is seldom possible, and some heat exchange occurs between the two chambers (ASTM, 2013). Likewise, although the insulated specimen mask ideally eliminates flanking heat transfer, in practice some occurs. The combined effect of the metering box heat transfer rate and flanking heat transfer rate were characterized for the GHB used in this thesis. The characterization consisted of determining the heat transfer rates in relation to the voltage generation of the thermopile wired between the walls of the

metering box which separate the metering box air and the room side air. This characterization method is described in Annex A6 of ASTM C1363 (ASTM, 2013).

The characterization test requires a homogenous test specimen of known thermal properties to be installed in the GHB. This test specimen is referred to as a "characterization specimen" (ASTM, 2013). The characterization specimen thermal properties are determined through testing a representative section of the material in a heat flow meter or guarded hot plate. For this thesis, a characterization specimen made entirely of XPS (extruded polystyrene) was used. The thermal resistance of this material for a variety of mean temperatures had been determined through previous testing not conducted during this thesis (Kumaran, 2006), using a heat flow meter.

A series of ASTM C1363 tests were completed on the characterization specimen. Each test was conducted with the metering box and cold side air temperatures held at the set point at which future specimens would be evaluated (21°C, - 20°C and -35°C respectively). The room side chamber air temperature is then varied in each successive test to induce heat transfer through the metering box walls. The room side chamber temperature is varied to ensure that temperatures occur both above and below the metering box air temperature This is done to capture situations of heat transfer from the room side into the metering box, and from the metering box into the room side chamber. This situation also induces flanking heat transfer from the specimen to the insulated mask, as the temperature profile through the insulated mask is expected to change slightly with changing room side chamber temperature.

The resulting thermopile voltage, heat rate input to the calorimeter, metering box air temperature, warm and cold side specimen surface temperatures, and cold side air

temperature are all recorded during the steady state conditions at each room side temperature test. Since the characterized specimen thermal resistance is known, and the surface temperatures of the specimen are monitored during each test, the rate of heat transferring through the specimen ($Q_{\mathrm{sp}}$) can be calculated. The resulting difference between the total heat input to the metering box ($Q_{\mathrm{in}}$) and the heat transfer rate through the specimen ($Q_{\mathrm{sp}}$) equals the combined effect of the metering box and flanking heat transfer paths at each condition of the metering box thermopile voltage. The slope of the difference between heat transfer through the specimen and heat input to the metering box is then determined for each condition, and used in future calculations to define the combined losses.

After the slope has been determined, the zero offset of the thermopile is determined. The zero offset of the thermopile is the residual heat loss that occurs due to the combined effect of metering box loss and flanking loss when the thermopile reads zero. The zero offset for the thermopile is determined by subtracting the heat transfer rate measured when the thermopile voltage is zeroed out from the expected ASTM C518 result.

### 2.2.6 Surface heat transfer coefficients

The surface heat transfer coefficients represent the combined heat transfer effect, including the effects of radiation, conduction, and convection, that occur between the air and specimen surfaces on hot and cold sides of the GHB during a test. The surface heat transfer coefficients can be required for several reasons. They can be used to determine the "surface to surface" thermal resistance of a specimen from the "air to air" thermal resistance measured in a GHB, or for boundary conditions for numerical modelling a GHB test. Additionally, to fully comply with the ASTM C1363 standard, the surface heat transfer

coefficients are required to be within a specified range. The surface heat transfer coefficients ($h_{\mathrm{amb}}$) for the warm and cold sides are determined using Equation 8 and Equation 9.

$$h_{\mathrm{amb,h}} = \frac{Q_{\mathrm{sp}}}{A * (T_{\mathrm{amb,h}} - T_{\mathrm{s,h}})} \qquad \textbf{Equation 8}$$

$$h_{\mathrm{amb,c}} = \frac{Q_{\mathrm{sp}}}{A * (T_{\mathrm{s,c}} - T_{\mathrm{amb,c}})} \qquad \textbf{Equation 9}$$

$Q_{\mathrm{sp}}$ - heat transfer through the specimen [W]
$A$ - specimen surface area perpendicular to the direction of heat transfer [$m^2$]
$T_{\mathrm{amb,h}}$ , $T_{\mathrm{amb,c}}$ - average metering box (h) air and cold side (c) air temperatures [°C]
$T_{\mathrm{s,h}}$ , $T_{\mathrm{s,c}}$ – average specimen metering box side surface and average cold side surface temperatures [°C]

The surface heat transfer coefficients are determined using the test results on the characterization specimen at each specified exterior temperature required to be tested on future specimens. The average surface temperatures on the warm and cold sides during the test, and the thermal resistance of the characterization specimen are known. Therefore, heat flow rate through the specimen is determined by solving Equation **5** for $Q_{\mathrm{sp}}$. Area of the specimen and the average air temperatures in the metering box and the cold side are also known from the test results. The surface heat transfer coefficients based on average steady state conditions on each side of the specimen during the test can then be calculated. The average surface heat transfer coefficients are assumed to be transferrable to the VIP wall assembly and are used as boundary conditions in the numerical modelling in this thesis.

## 2.3 Industry standard calculation methods

The purpose of this thesis is to investigate the accuracy of industry standard calculation methods in predicting the effective thermal transmittance of a wall assembly containing VIPs when compared to results of GHB tests. This section describes the industry

standard calculation methods that were evaluated in this thesis. The calculation methods described in this section include the following:

1. Parallel path method
2. Isothermal planes method
3. Modified zone method
4. BRE 465 method
5. Thermal transmittance method

### 2.3.1 Parallel path method

The parallel path calculation method assumes that all heat transfer occurs parallel to the interior to exterior temperature gradient (ASHRAE, 2013). As such it does not account for any two- or three-dimensional heat transfer including lateral heat flows that occur in the wall.

In general, the method consists of dividing the frontal areas of the wall into sections based on their substructure differences or anticipated differences in thermal resistance value (R-value). A one-dimensional conduction resistance calculation is conducted based on an analogous electrical circuit of resistors in series for all materials along the division paths (Incopera, 2006). The R-values of each wall division are summated in an area weighted average based on the wall divisions frontal area relation to the total frontal area. The frontal area division used for the wall assembly investigated in this thesis is presented in Figure 7.

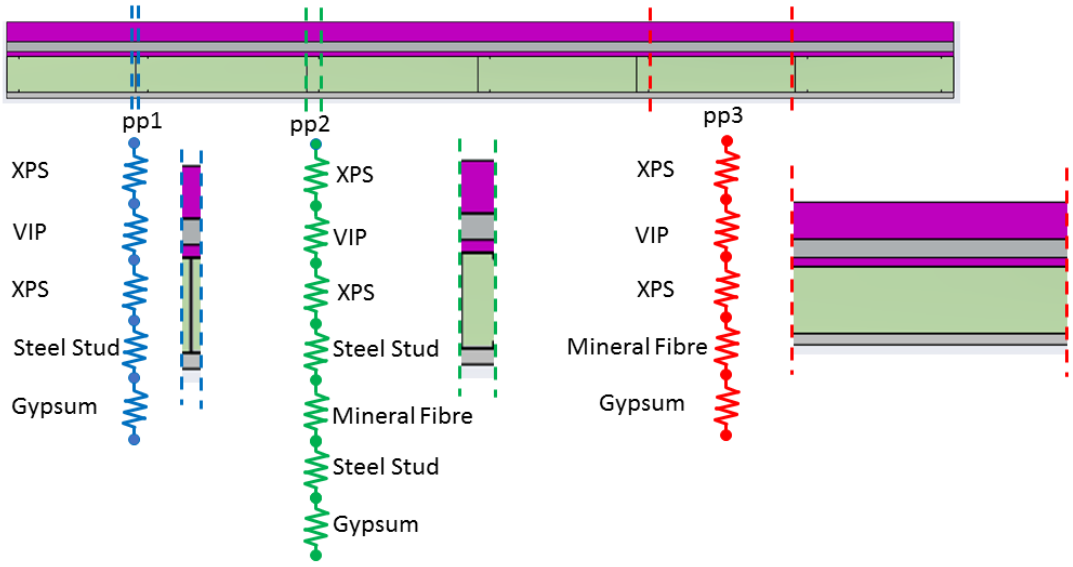


**Figure 7: Parallel path method.**

### 2.3.2 Isothermal planes method

The isothermal planes method assumes that all heat transfer occurs primarily laterally throughout each layer to form isotherms, then layer by layer in the direction of the thermal gradient. The method consists of dividing the wall into isothermal planes perpendicular to the interior to exterior temperature gradient. This method again uses the analogous electrical circuit, but this time divides the wall into sections which make use of the summation of resistors in parallel (Incopera, 2006) for each layer. The layers are solved first to determine the overall thermal resistance for each plane, then the planes are summated as resistors in series to determine the overall wall thermal resistance. Figure 8 depicts the isothermal planes method plane divisions for the wall assembly evaluated in this thesis.

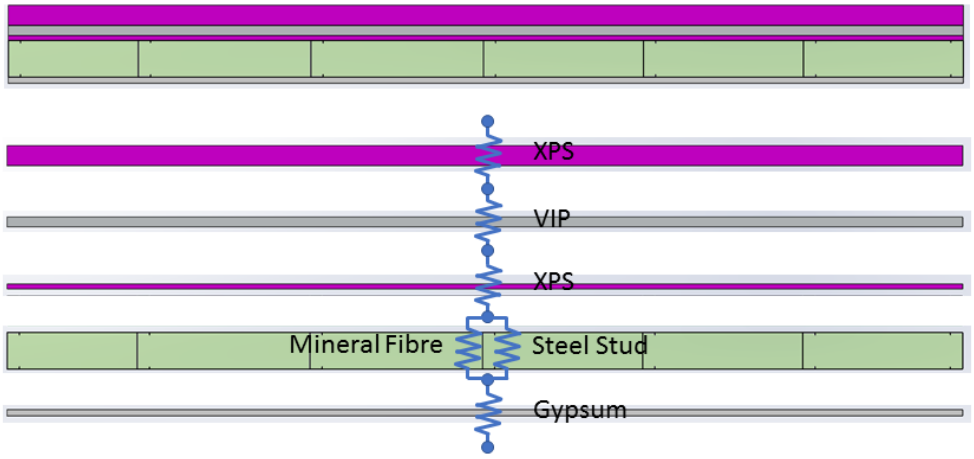


**Figure 8 : Isothermal planes method.**

### 2.3.3 Modified zone method

The modified zone calculation method (Kosny, 1995) was developed to account for the effects of steel studs on the thermal resistance of the wall assembly. It uses the "thermally effected zone" as the area for the parallel path calculation method rather than just the physical area of the component. The thermally effected zone is determined as the area to which the high thermal transmittance element effects the lower thermal transmittance elements around it.

The modified zone ($W$) is a function of the stud flange size ($L$), the thickness of material layers in the section including studs ($d_{\mathrm{i}}$), and the zone factor ($z_{\mathrm{f}}$). The equation for the thermally effected zone is presented in Equation 10.

$$W = L_{sf} + z_{\mathrm{f}} * \sum_{\mathrm{i}=1}^{\mathrm{n}} d_{\mathrm{i}} \qquad \textbf{Equation 10}$$

$L_{sf}$ - stud flange size [m]
$d_{\mathrm{i}}$ - thickness of material layers in the section including studs, sheathing board, etc. [m]
$z_{\mathrm{f}}$ - zone factor

The zone factor is defined as the ratio between the thermal resistivity of the combined materials in the first 25mm from the stud towards the exterior of the sheathing material and the thermal resistivity of the cavity insulation. The zone factor is given in the ASHRAE Handbook of Fundamentals (ASHRAE, 2013). The zone factor in this work was determined by transcribing this figure and fitting a curve to the resulting data, shown in Figure 9.

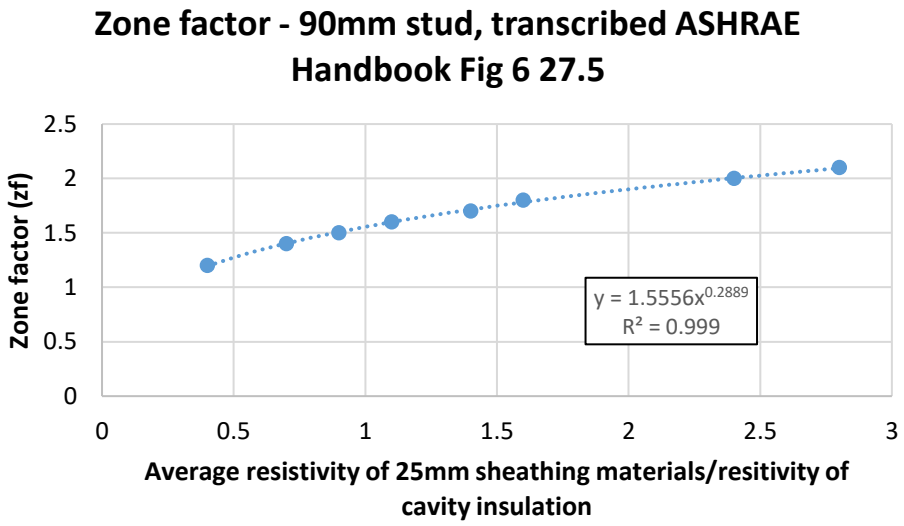


**Figure 9: Extrapolation of zone factor chart.**

### 2.3.4 Building Research Establishment Digest 465 method

The Building Research Establishment (BRE) Digest 465 method (S. Doran, 2002; Gorgolewski, 2007) was also developed to determine the thermal resistance of wall assemblies containing steel studs. It consists of a weighted average method using the results

from the isothermal planes ($R_{min}$) and parallel path ($R_{max}$) calculation methods. The weighted average depends on a weighting factor ($p$) that is used to determine the contributions of the isothermal planes and parallel path calculation methods to the effective thermal resistance of the wall assembly. The estimated wall R-value ($R_t$) for light steel framing is determined from Equation 11.

$$R_{\mathrm{t}} = p * R_{\mathrm{max}} + (1 - p) * R_{\mathrm{min}} \qquad \textbf{Equation 11}$$

The weighting factor ($p$) is a correlation that was determined from the results of 52 different wall configurations that were simulated using a validated simulation program. The weighting factor is a function of the thermal resistance as calculated by the isothermal planes ($R_{\mathrm{min}}$) and the parallel path method ($R_{\mathrm{max}}$), the flange width ($w$), the stud spacing ($s$) and the stud depth ($d$). It is presented in Equation 12.

$$p = 0.8 * \left(\frac{R_{\mathrm{min}}}{R_{\mathrm{max}}}\right) + 0.44 - 0.1 * \left(\frac{w}{40\ \mathrm{mm}}\right) - 0.2 * \left(\frac{600\ \mathrm{mm}}{s}\right) - 0.04\left(\frac{d}{100\ \mathrm{mm}}\right) \qquad \textbf{Equation 12}$$

# 3 Chapter: Results of guarded hot box characterization experiments

This section presents the results for the heat flow path characterization tests, and the surface heat transfer coefficients in the GHB.

## 3.1 Heat flow path characterization results

As discussed, the heat flow path characterization for heat transfer through the metering box walls and between the specimen and mask ("flanking loss") were determined in a combined fashion, following the procedure detailed in Annex 6 of ASTM C1363. This procedure consists of varying the room side temperature to produce different heat transfer conditions across the metering box walls. The results are then correlated to the corresponding voltage ($E_0$) generated by the thermopile wired between the metering box walls.

The correlation for the metering box heat exchange related to the thermopile voltage for each exterior temperature are shown in Figure 10 and Figure 11. Plots of the experimental data for each test condition are presented in Appendix A .

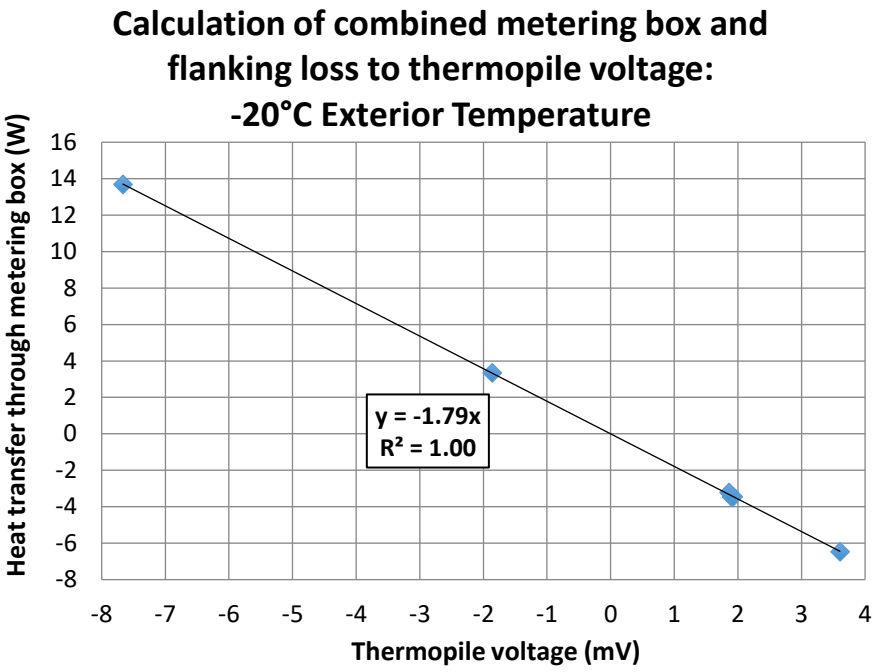


Figure 10: Thermopile voltage calibration, -20°C.

**Table 4: Thermopile characterization -20°C**

| $E_0$ [mV] | Power [W] |
|---|---|
| 1.90 | -3.46 |
| 1.92 | -3.45 |
| -1.86 | 3.34 |
| -7.67 | 13.69 |
| 3.60 | -6.48 |
| 1.86 | -3.22 |

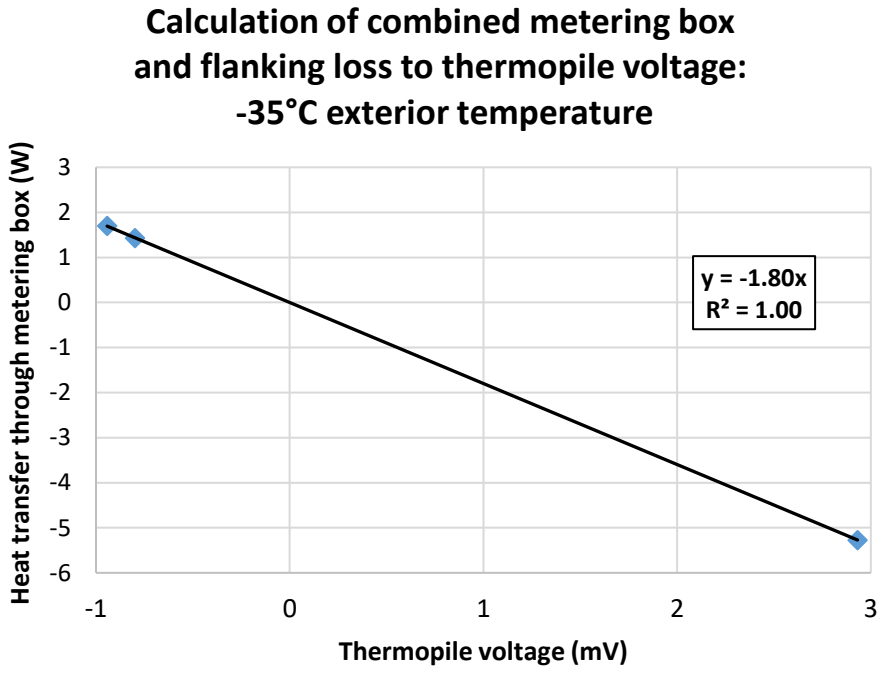


Figure 11: Thermopile voltage calibration, -35°C.

**Table 5: Thermopile characterization -35°C**

| $E_0$ [mV] | Power [W] |
|---|---|
| 2.93 | -5.27 |
| -0.94 | 1.70 |
| -0.80 | 1.42 |

The results shown in Figure 10 and Figure 11 for the relationship between the combined metering box and flanking losses and the thermopile voltage are very close for the two-different exterior temperatures. This is expected for the metering box loss, as it is much more dependent on the temperature difference between the metering box air and the room side air. The flanking loss should be slightly dependent on exterior temperature, as the temperature profile across the wall specimen and the mask changes for varying exterior temperature.

The difference between the ASTM C1363 test value, and expected result calculated from the ASTM C518 test at each exterior temperature is considered the zero offset ($E_0$=0). The results for the zero offset at each temperature are shown in are shown in Table 6. The difference in slopes is likely due to experimental error.

**Table 6: Zero offset for combined metering box loss and flanking loss at thermopile voltage $E_0$=0.**

| Exterior temperature | Zero offset [W] |
|---|---|
| **-20°C** | -1.6 |
| **-35°C** | 4.2 |

### 3.1.1 Combined metering box and flanking loss equations

The combined equation for the metering box and flanking loss characterization for each exterior temperature is presented in Table 7.

**Table 7: Metering box and flanking loss equation for each exterior temperature**

| Exterior temperature | Combined metering box and flanking loss |
|---|---|
| **-20°C** | -1.79($E_0$) - 1.6 |
| **-35°C** | -1.80($E_0$) + 4.2 |

## 3.2 Surface heat transfer coefficients

The surface heat transfer coefficients were determined using the procedure outlined previously. It consisted of conducting an ASTM C1363 test on a characterization specimen, and calculating the surface heat flux coefficients for each side of the specimen based on the difference between the surface and air temperatures, and the heat flow through the wall. The resulting values for each temperature test are shown in Table 8.

**Table 8: Convection heat transfer coefficient calculation results**

| | Convection heat transfer coefficient [$m^2K/W$] | |
|---|---|---|
| | **Exterior surface** | **Interior surface** |
| **-20°C** | -60.8 | 8.9 |
| **-35°C** | -50.4 | 7.5 |

These average values are assumed to be consistent in the VIP wall test. The values are used as heat flux boundary conditions in the industry standard calculation methods and the numerical simulations to enable comparison to the GHB experiment results.

# 4 Chapter: Guarded hot box experiment set up and results

This chapter describes the wall assembly that was tested in the GHB. The wall assembly materials and configuration are first described, followed by the locations in the wall assembly that were instrumented for temperature measurement. Following the description of the wall assembly the instrumentation locations and results of the GHB tests are presented.

## 4.1 Wall assembly description and instrumentation locations

The wall assembly consisted of a 2.44 m x 2.44 m x 0.20 m (8 ft x 8 ft x 8 in) specimen including both steel studs and VIP's. The materials and dimensions used in the wall assembly are listed in Table 9 and a sketch of the layers of the wall assembly is shown in Figure 12.

**Table 9: Summary of wall assembly materials and dimensions.**

| Layer | Description |
|---|---|
| **1** | 15.875 mm (5/8 in) gypsum board |
| **2** | 10 mil polyethylene |
| **3** | Mineral fibre insulation (89 mm, 3.50 in) |
| **4** | 26 awg. Steel stud, with fiberglass clips for mounting VIP sandwich panels. |
| **5** | XPS-VIP-XPS sandwich panel (from interior to exterior) – 12.7 mm (1/2 in) XPS, 25 mm (1 in) VIP panel, 50 mm (2 in) XPS. |

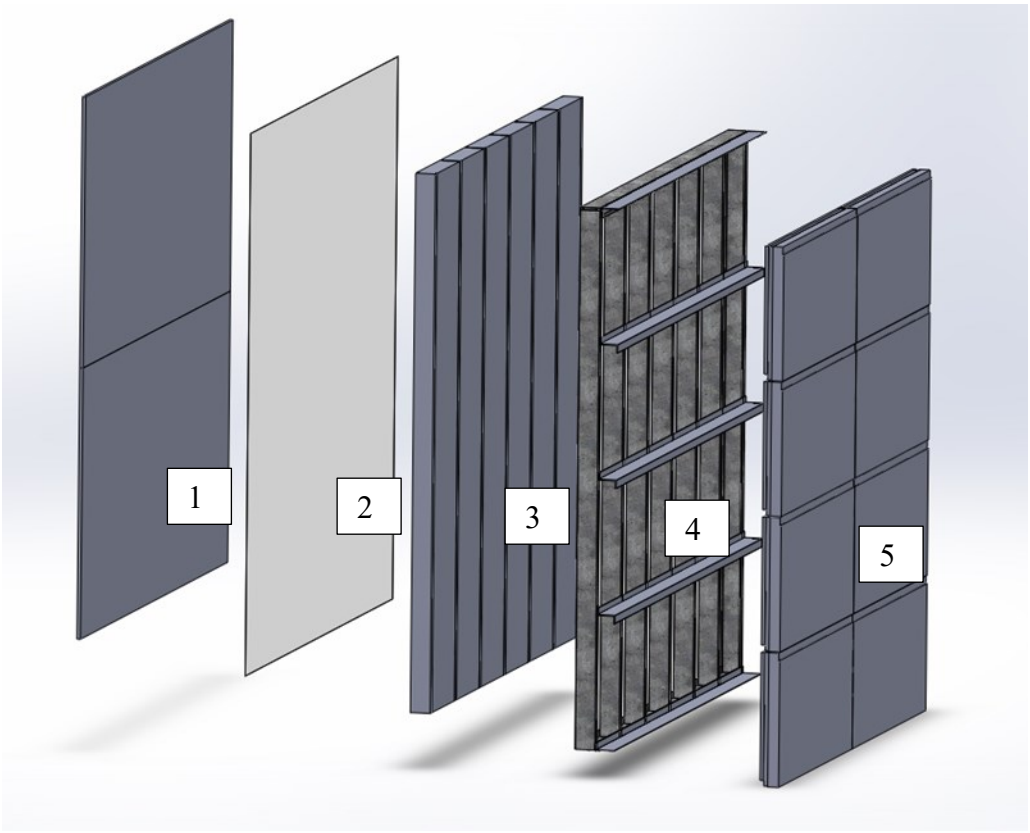


**Figure 12: Schematic of wall assembly layers.**

Figure 12 layer 5 represents the XPS-VIP-XPS sandwich layer, which were made by adhering XPS to the interior and exterior side of 600 mm x 1200 mm x 25 mm VIP panels. The XPS layers were added to the VIP panel to protect the VIP surface from coming in to contact with sharp or abrasive surfaces in the wall assembly. These abrasive surfaces included the surface and edges of the steel studs, the fiberglass clips holding the panels in place and the fasteners from the exterior strapping or cladding.

The XPS panels were slightly oversized (>600 mm high, >1200 mm wide) in each sandwich assembly compared to the VIP dimensions to ensure that adjacent VIP edges would not be in contact in the wall assembly. Due to construction tolerances and the

oversized XPS portions of the sandwich assembly, the butt jointed panels resulted in slight air gaps. To eliminate the effect of the vertical air gap between XPS panels, caulking was added to the vertical joints. The horizontal air gaps between the rows of sandwich panels were not filled and therefore air gaps remained during testing. All seams were sealed on the exterior surface with tape to ensure that air exchange did not occur between these air joints and the exterior environment during testing. Representative photos of the butt joint, air gaps present in the assembly and the final taped exterior surface are shown in Figure 13.

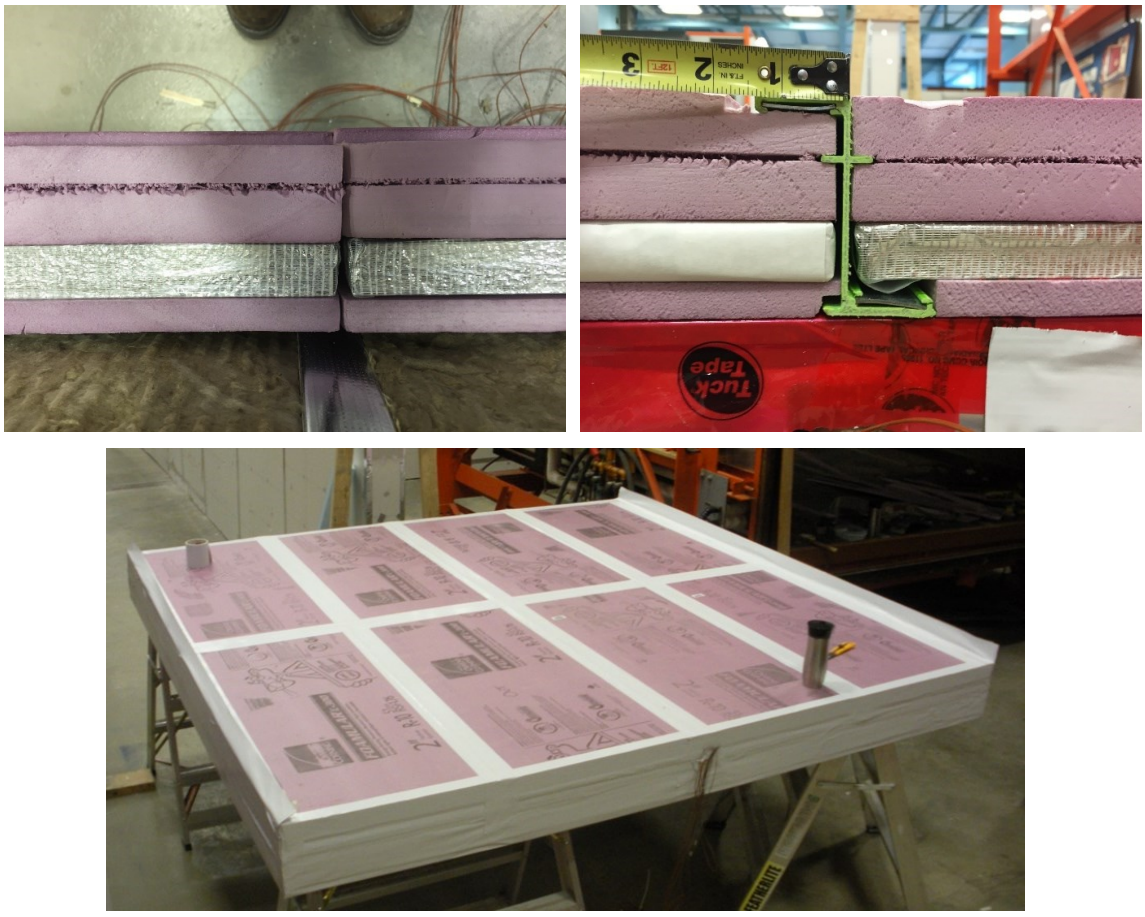


**Figure 13: Photos depicting the assembly air gaps that existed between XPS-VIP-XPS sandwich panels and the taped exterior surface to eliminate air exchange with the cold exterior.**

The air temperatures in the metering box (interior) and the cold side (exterior) chambers are monitored by up to 10 thermocouples suspended in mid-air from a sensor stand, spaced approximately 0.175 m from the specimen surface. The wall assembly instrumentation is further described in a following section.

The specimen was instrumented with Type T thermocouples to determine the interior (warm side) wall surface temperature, exterior (cold side) wall surface temperature and the temperature of several areas of interest in the wall assembly. The thermocouples were adhered to the surfaces of the wall assembly with two layers of tape. The first layer of tape was aluminum duct tape. It was used to ensure that the thermocouple tip was held in precise contact with the surface it was measuring. The thermocouple was adhered to the wall using the aluminum tape for at least 100 mm (~4 in) of its length to avoid the thermocouple adversely affecting the temperature at the location of measurement at the tip junction. The aluminum sheathing tape was covered by a second layer of white masking tape to shield the taped area from radiation effects.

The interior surface of the wall assembly was instrumented to account for surface temperature variations with twenty thermocouples. The thermocouples were arranged to account for variations in surface temperature between the centre of stud cavity and steel stud thermal bridge locations. The thermocouple instrumentation pattern is shown in Figure 14. The exterior surface was instrumented in the mirror image of the interior surface.

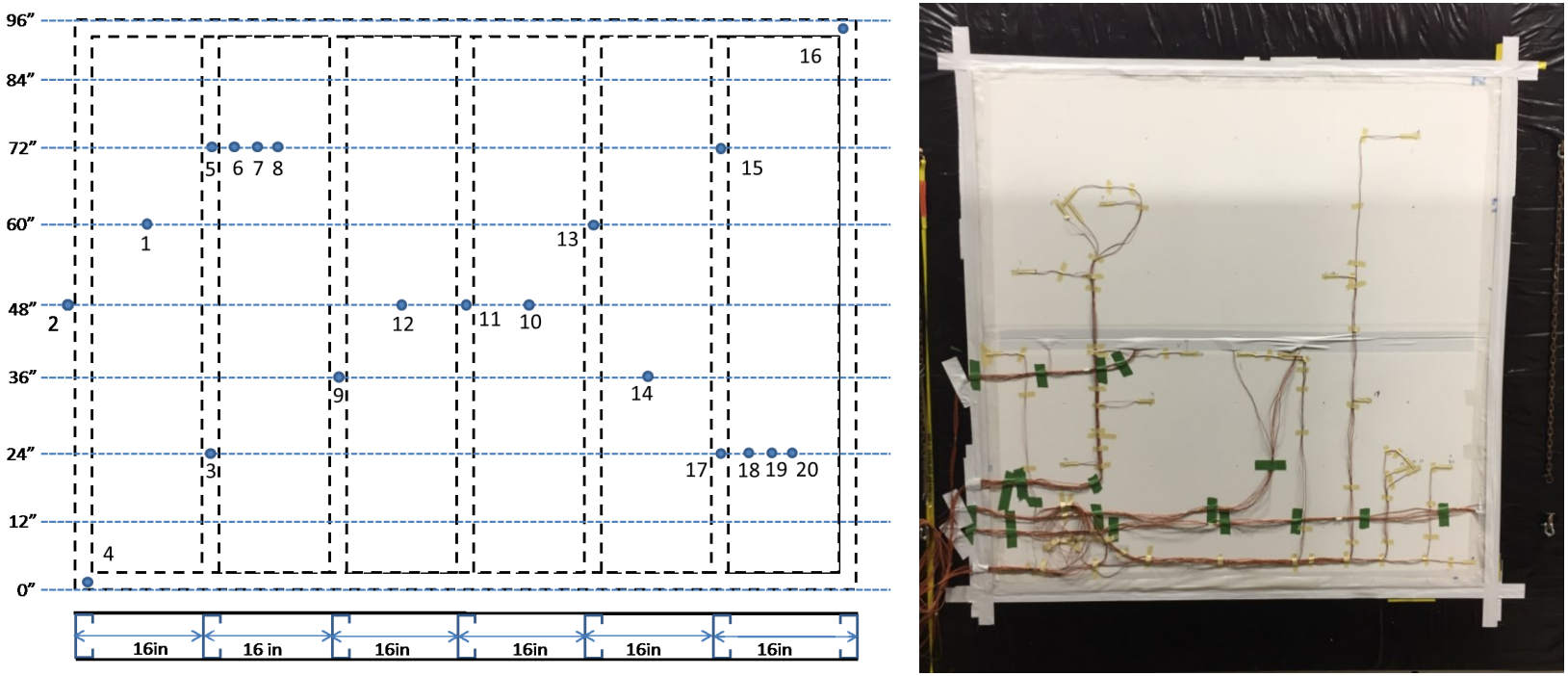


**Figure 14: Interior surface thermocouple instrumentation map.**

The surface thermocouples were installed to determine the effect of the steel stud on the interior temperature. The thermocouple locations on the surface by thermocouple number from Figure 14 are given in Table 10. It is estimated that the thermocouples were installed within ±5 mm (~0.20 in) of the nominal location.

**Table 10: Surface thermocouple locations**

| Thermocouple location | Thermocouple label |
|---|---|
| Centre of stud cavity (single) | 1, 10, 12, 14 |
| Centre of steel stud flange (single) | 3, 9, 11, 13, 15 |
| Centre of steel stud flange | 5, 17 |
| 1 in (~25 mm) from centre steel stud flange | 6, 18 |
| 2 in (~50 mm) from centre steel stud flange | 7, 19 |
| 8 in (~200 mm) from centre steel stud flange/centre cavity | 8, 20 |
| Corner | 4, 16 |
| Edge | 2 |

In addition to the thermocouples on the surface of the wall assembly, several areas of interest within the wall assembly were monitored. The areas of interest in the wall assembly were designed to measure the temperature from interior to exterior in the mineral fibre insulation at the centre of the stud cavities and the temperature distribution from the centre to the edge of the VIP interior and exterior surfaces.

### 4.1.1 Temperature profile through the depth of mineral fibre

Three sets of four thermocouples (12 total) were installed to measure the temperature profile through the mineral fibre insulation at the centre of the stud cavity. The thermocouple sets were located at three different heights in the stud cavity, nominally at 24 in (600 mm), 48 in (1200 mm) and 72 in (1800 mm) from the bottom.

The four thermocouples in each set were aligned and spaced to measure the temperature profile of the mineral fibre from interior to exterior. The first thermocouple

was placed at the mineral fibre/gypsum sheathing interface, the second nominally located at 25 mm (~1 in) from the gypsum, the third 50 mm (~2 in) from the gypsum and the fourth 75 mm (~3 in) from the gypsum. The instrumentation locations for the thermocouples in the mineral fibre are shown in Figure 15. It is estimated that the thermocouples were installed within ±5 mm (~±0.20 in) of the nominal location.

The thermocouples were held in place by taping them to a small metal wire suspended in the mineral fibre. The mineral fibre was cut at the locations for each thermocouple tree, directly below the location of the thermocouple installation, such that the mineral fibre insulation also supported the thermocouples in their position. Mineral fibre was then press fit above the thermocouples and pressed down on to the thermocouple tree to ensure that no air gap existed at the mineral fibre joint.

The values of the temperature profile through the mineral fibre at the centre of the stud cavity were used for validating the two and three-dimensional numerical heat transfer models completed in this thesis.

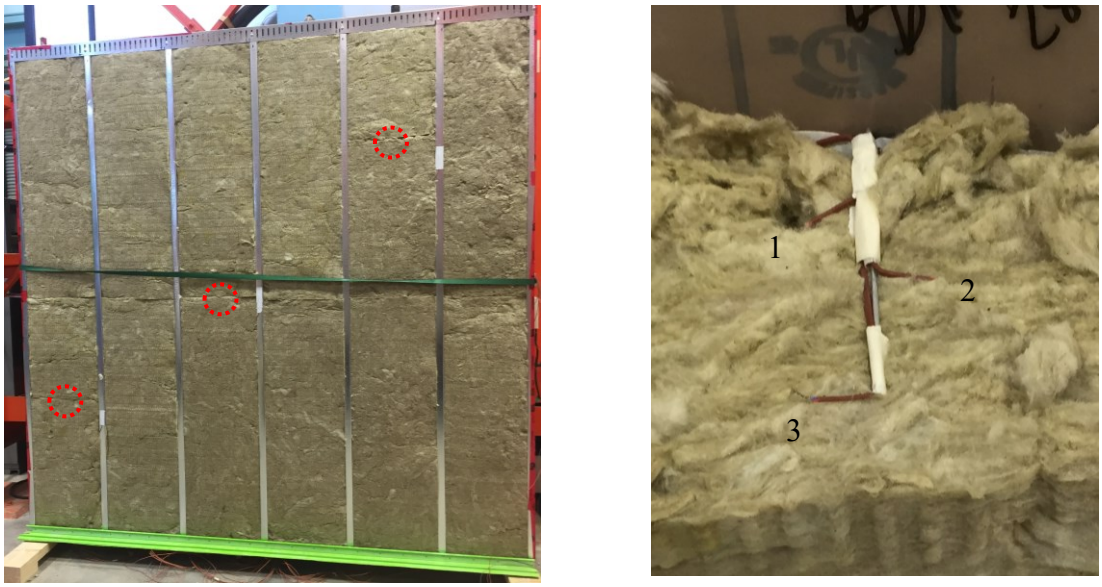


**Figure 15: Thermocouple locations in the mineral fibre insulation. The red circle in the left photo indicates the instrumentation locations for the thermocouples at the centre of the stud cavities, through the depth of the mineral fibre insulation. The photo on the right is a close-up top view of the thermocouples through the depth of the mineral fibre at each location, located at 1in, 2in and 3 in from the gypsum board.**

### 4.1.2 Centre to edge temperature distribution on vacuum insulated panel surface

The interior and exterior surfaces of a single VIP were instrumented to determine the difference in temperature between the centre of the panel and edge of panel during the test. The thermocouple locations for the VIP panel are shown in Figure 16.

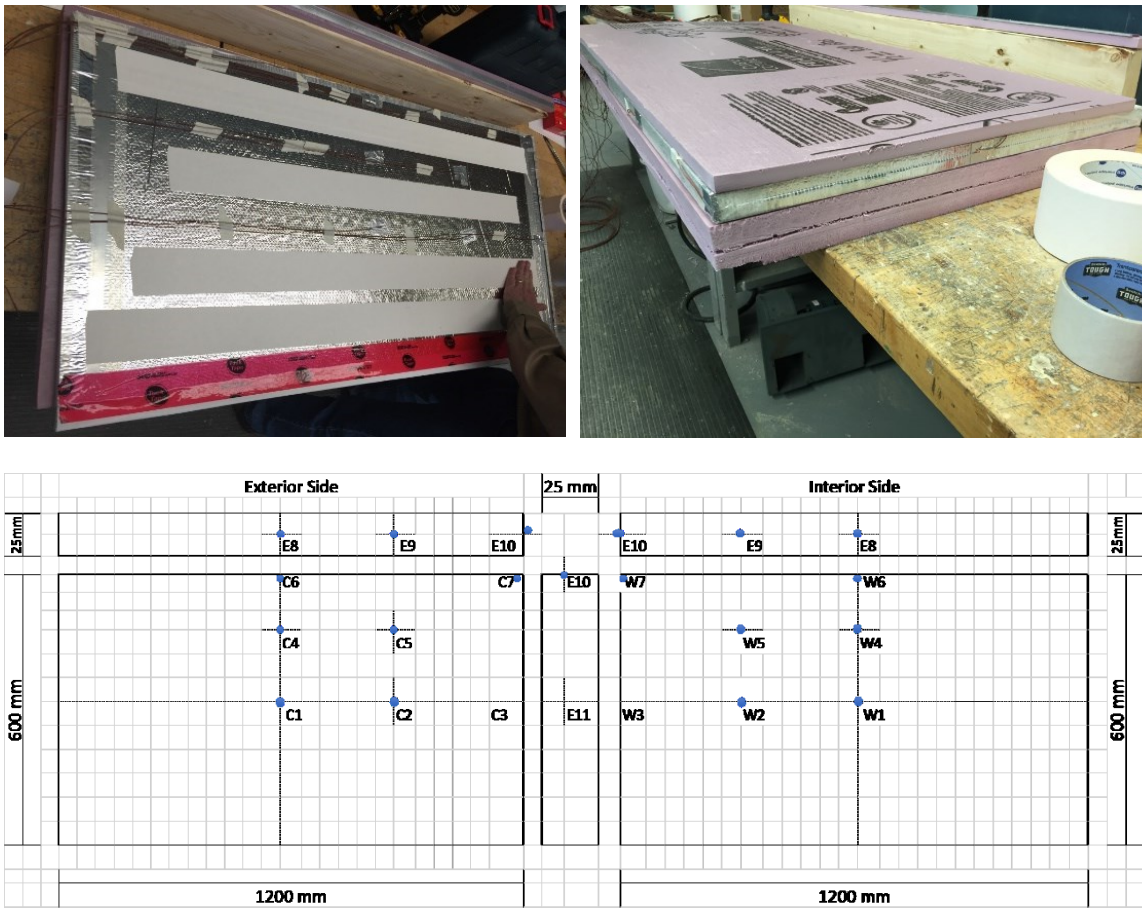


**Figure 16: Thermocouple locations on the VIP. The top left photo depicts the thermocouples instrumented on the VIP on the exterior (cold) surface of the VIP. The top right photo depicts the sandwich panel assembly and shows the edge thermocouples. The bottom photo is a graphical representation of the location of all thermocouples installed on the interior (warm, 'W') surface, exterior (cold, 'C') surface, and edge ('E') of the VIP.**

## 4.2 Experiment results

The steady state thermal resistance of the wall assembly was characterized for two weather side temperatures. The first temperature was -21°C, and the second was -35°C. The metering box temperature was maintained at 21°C during both tests. The test results

were used to determine the accuracy of industry standard calculation methods (ASHRAE, 2013), and two- and three-dimensional numerical simulations.

The following sections present the calculated "air to air" thermal resistance, the effect of the steel stud thermal bridge on the gypsum surface temperature, the temperature distribution through the mineral fibre insulation and the temperature distribution between the centre and edge of the VIP panels. Plots of the raw data measured during the experiments are presented in Appendix C and Appendix D .

### 4.2.1 ASTM C1363 results: Exterior temperature of -20°C and -35°C

The experiment results of the "air to air" thermal resistance calculation for each exterior temperature test are presented in Table 11.

**Table 11: Thermal resistance calculation results.**

| | -20°C | -35°C |
|---|---|---|
| R value (RSI, $m^2K/W$) | 6.86 | 6.84 |
| R value ($hrft^{2\circ}F/Btu$) | 38.9 | 38.9 |

The results presented in Table 11 show that there is insignificant change in R-value for the decrease in exterior temperatures. This is most likely due to the VIPs, which account for the majority of the R-value in the wall assembly, not varying in thermal resistance for the two exterior temperatures evaluated.

#### 4.2.1.1 Effect of steel stud thermal bridge on gypsum surface temperature

The interior surface of the gypsum sheathing board was instrumented to determine the effect of the steel stud thermal bridge on surface temperature. The surface temperature of the interior sheathing board is an important performance factor for several reasons. These include differences in temperature on the surface relate to the amount of heat being

transferred through the sheathing board, colder sections can be at risk to condensation and the surface temperature relates to how comfortable a room feels.

The effect of the steel stud thermal bridge on the interior surface temperature of the gypsum was measured using thermocouples adhered to the gypsum surface. The thermocouples were installed in a horizontal line, extending away from the centre of the steel stud flange steel stud towards the centre of the stud cavity. The interior surface temperature in proximity to the steel stud results for each exterior temperature are shown in Figure 17. The grey dotted line represents the steel stud location in relation to the surface thermocouples.

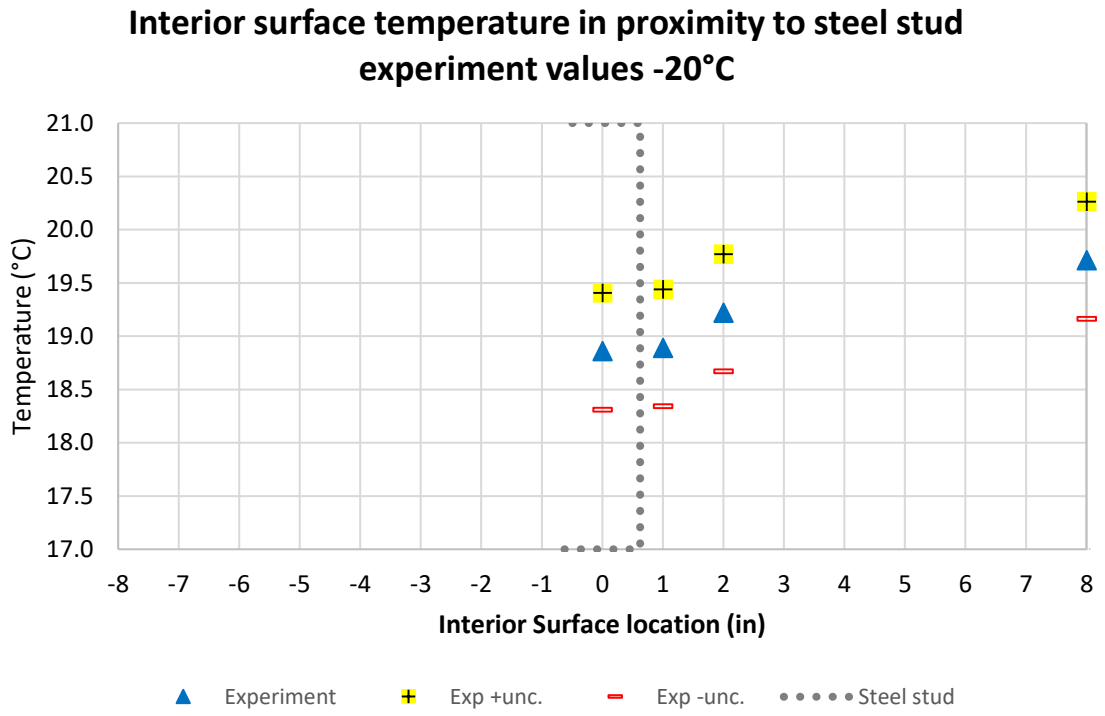


**Figure 17: Interior gypsum surface temperature around steel stud at -20°C exterior temperature.**

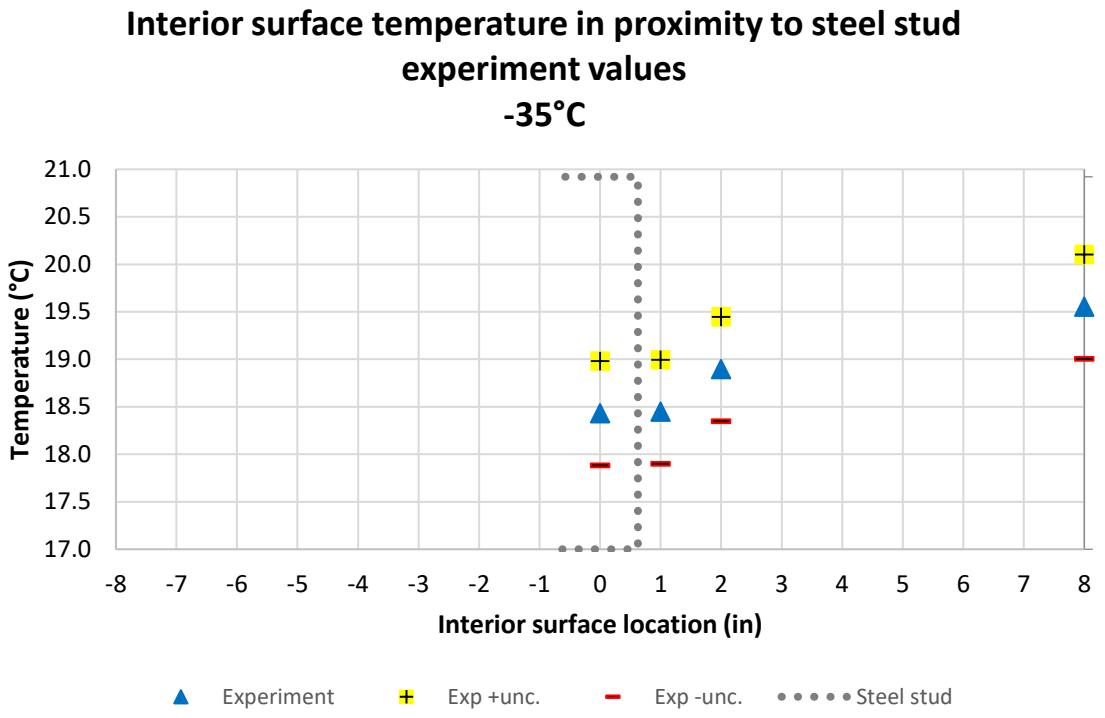


**Figure 18: Interior gypsum surface temperature around steel stud at -35°C exterior temperature.**

The results show that the thermal bridge effective area is larger than the physical contact area between the stud and the gypsum board. This effect is well documented for thermal bridges (ASHRAE, 2011; Kosny, 1995; Morris and Hershfield Ltd., 2014; S. Doran, 2002). Calculation methods that do not account for thermal bridges potentially underestimate heat transmission by 20% to 70% (Morris and Hershfield Ltd., 2014). This effect is of note in highly insulated walls, as thermal bridges can be the most significant contributors to heat transfer.

In addition to heat transfer effects, it is important to consider the effect of thermal bridges on the surface temperature of the gypsum to assess the condensation risk of the wall assembly (ASHRAE, 2016; Morris and Hershfield Ltd., 2011; National Research Council Canada, 2015). Although the effect of the steel stud thermal bridge is evident on

the surface temperature in this wall assembly (and correspondingly the thermal resistance), the potential for localized condensation at the steel stud contact area is low, as the interior humidity at 21°C would have to be above RH70% for condensation to occur. Therefore, in this wall assembly, while the steel stud effects the interior surface temperature of the gypsum it does not cause a condensation risk.

#### 4.2.1.2 Mineral fibre temperature distribution

The temperature distribution through the mineral fibre was monitored in three separate locations in the centre of the stud cavity. The average results for each depth these three locations are presented in Table 12.

**Table 12: Temperature distribution along the depth of the mineral fibre insulation**

| | 0 mm | 25 mm | 50 mm | 75 mm |
|---|---|---|---|---|
| **-20°C** | 19.4 | 16.1 | 13.8 | 9.4 |
| **-35°C** | 19.1 | 14.7 | 11.6 | 5.7 |

As expected, the temperature decreases from interior to exterior and each depth location temperature decreases with decreasing exterior temperature. These results were used to validate symmetry assumptions in the thermal modelling.

#### 4.2.1.3 Vacuum insulated panel temperature distribution

A representative VIP panel was instrumented on the interior and exterior surfaces to determine the temperature variation from centre of the panel to the edges. The results for each exterior temperature are shown in Figure 19 (-20°C), Figure 20 (-35°C) and Table 13.

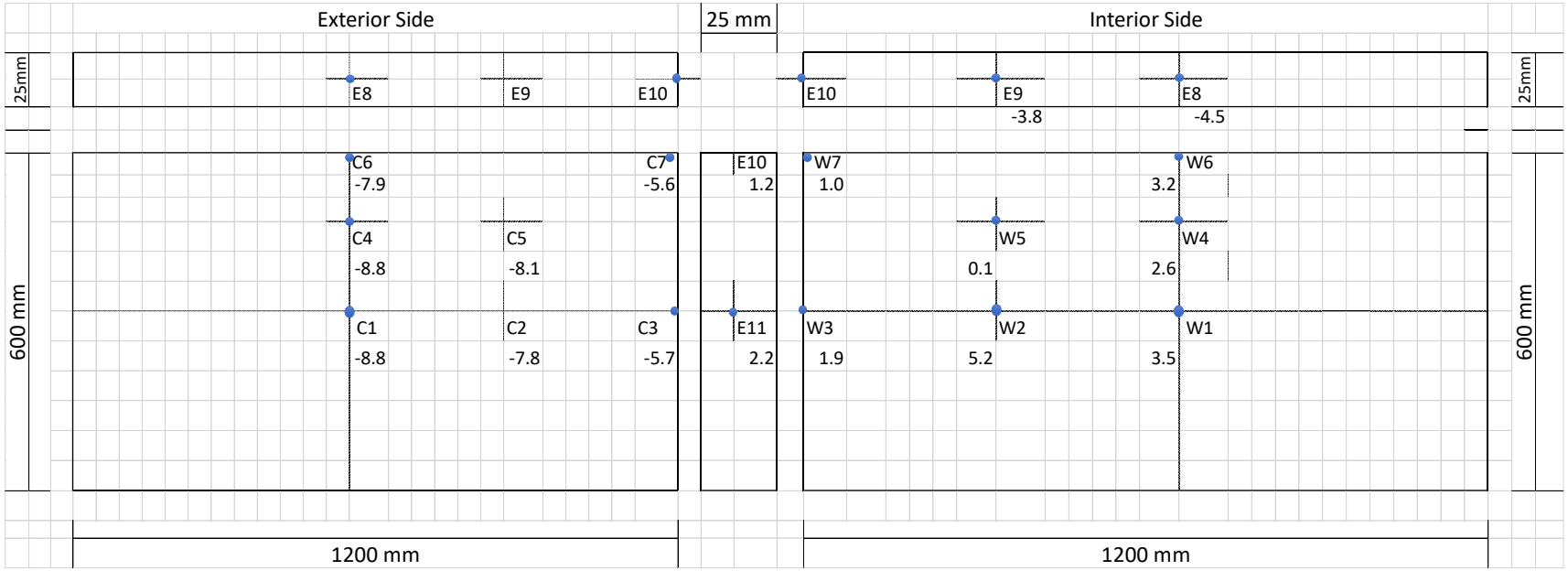


**Figure 19: Temperature distribution on interior (W) and exterior (C) surfaces of VIP panel during -20°C test.**

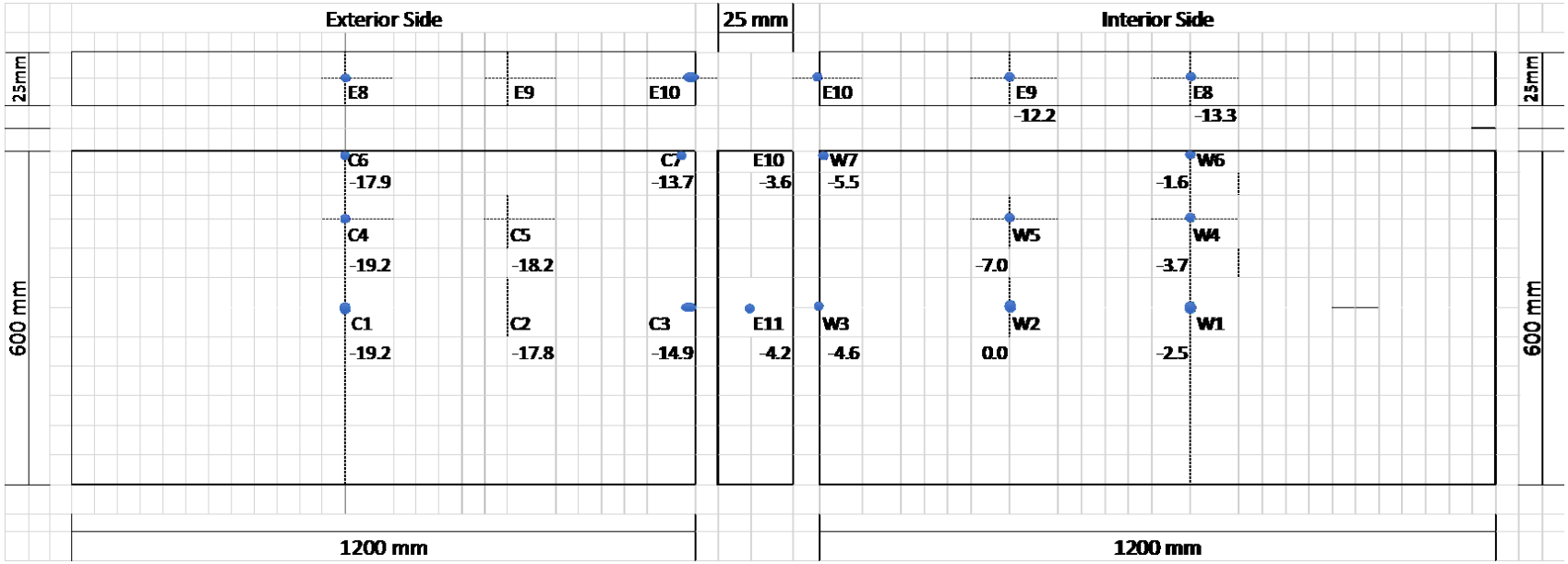


**Figure 20: Temperature distribution on interior (W) and exterior (C) surfaces of VIP panel during -35°C test.**

**Table 13: Interior and exterior VIP surface temperature for exterior temperatures of -20°C and -35°C. The thermocouples are labelled for interior side (W), exterior side (C) and edge (E), numbers as per Figure 16.**

| | -20°C | -35°C | | -20°C | -35°C | | -20°C | -35°C |
|---|---|---|---|---|---|---|---|---|
| **W1** | 3.5 | -2.5 | **C1** | -8.8 | -19.2 | **E8** | -4.5 | -13.3 |
| **W2** | 5.2 | 0 | **C2** | -7.8 | -17.8 | **E9** | -3.8 | -12.2 |
| **W3** | 1.9 | -4.6 | **C3** | -5.7 | -14.9 | **E10** | 1.2 | -3.6 |
| **W4** | 2.6 | -3.7 | **C4** | -8.8 | -19.2 | **E11** | 2.2 | -4.2 |
| **W5** | 0.1 | -7.0 | **C5** | -8.1 | -18.2 | | | |
| **W6** | 3.2 | -1.6 | **C6** | -7.9 | -17.9 | | | |
| **W7** | 1.0 | -5.5 | **C7** | -5.6 | -13.7 | | | |

The results presented in Figure 19 and Figure 20, for the exterior temperatures of -20°C and -35°C respectively, generally indicate that a higher rate of heat transfer is occurring through the edges than through the centre of the panel. For the exterior (cold, C) surfaces, this trend is evident with the temperature in the centre being the coldest and getting warmer towards the edges.

For the -20°C exterior temperature, this results in an exterior surface centre of panel temperature of -8.8°C (C1) increasing to -5.7°C (C3), -5.6°C (C7) and -7.6°C (C6) at the edges. The intermediate temperatures measured at C2, C4 and C5 also indicate a warming trend compared to the centre of panel value, with C4 exhibiting the same temperature as the centre of the panel.

This trend is more evident at the -35°C temperature test, with a centre of panel value of -19.2°C (C1), increasing to -14.9°C (C3), -13.7°C (C7) and -17.9°C (C6) at the edges. Again, the intermediate temperatures measured at C2, C4 and C5 also indicate a warming

trend compared to the centre of panel value, with C4 again measuring the same as the centre of panel temperature.

The interior (warm, W) surface shows less consistent trends. The centre of panel value for the -20°C exterior temperature was 3.5°C (W1), with edge temperatures of 1.9°C, 1.0°C and 3.2°C. This decrease in temperature would also indicate higher heat transfer rates at the edge. The intermediate locations exhibit temperatures that do not follow the trends, where W4 and W5 indicate temperatures which are less than both the centre panel and the edge temperatures, and W2 measuring at a higher temperature than both the centre of panel value and edge temperatures. The -35°C temperatures exhibit slightly greater disparity, with a centre of panel temperature of -2.5°C (W1), and edge temperatures of -4.6°C (W3), -5.5°C (W7) and -1.6°C (W6). The temperatures measured at W3 and W7 follow the trend; however, W6 is warmer than W1, which would indicate less heat transfer is occurring at that edge than the centre of panel. The intermediate values are also inconsistent with W4 and W5 being colder than the centre panel value, while W2 is warmer.

The most likely reason for the inconsistencies on the interior side temperature is the presence of steel studs. The steel studs would cause discrepancies in the temperature trends from centre to edge, by creating a warmer temperature (thermal bridge from the interior) at thermocouples which are closer to the stud. To investigate this more instrumentation would be required, especially in the region of the steel stud area.

Although the interior is not as consistent as the exterior surface in demonstrating the increased heat transfer at the edge versus the centre of the panel, there is still evidence for this phenomena in most centre to edge comparisons. The inability to further resolve the

effect of the steel stud on the interior temperature increases the uncertainty of the interior trends. Using the more consistent exterior side, the effect of the edge is clearly exhibited and experimentally demonstrates that designing wall assemblies with VIP's without accounting for edge and joint heat transfer is likely to lead to underestimations in heat transfer rate calculations.

# 5 Chapter: Guarded hot box experiment uncertainty

The uncertainty of the GHB test results is determined for the temperature measurements and the thermal resistance calculation. The temperature measurements are dependent on the uncertainties of the thermocouples. The thermal resistance uncertainty is due to the combined uncertainty of the thermocouples, heat input to the metering box, the specimen area, and the characterization experiments, as described in Equation 13.

$$R = \frac{A * \left(T_{\text{env,h}} - T_{\text{env,c}}\right)}{Q_{\text{t}} - (Q_{\text{mb}} + Q_{\text{fl}})} \qquad \textbf{Equation 13}$$

$R$ – thermal resistance of the specimen [m$^2$K/W]
$A$- Specimen area [m$^2$]
$T_{\text{amb,h}}$ – Interior Air Temperature [°C]
$T_{\text{amb,c}}$ – Exterior Air Temperature [°C]
$Q_{\text{t}}$ – Total heat added to the calorimeter [W]
$(Q_{\text{mb}} + Q_{\text{fl}})$ – combined heat loss through the metering box to the room side guard and from the specimen to the mask (flanking loss) [W]

The following sections describe the uncertainty estimation for each parameter in Equation 13. The combined uncertainty for the RSI of the wall specimen determined for each exterior temperature evaluated in this thesis is estimated using the method described in Moffat (Moffat, 1988).

## 5.1 Thermocouple uncertainty

The thermocouple measurement has uncertainty due to the uncertainty of the thermocouple material, uncertainty of the cold junction reference temperature, and the uncertainty of the data acquisition. The data acquisition uncertainty is applied to both the thermocouple reading, and the cold junction reference reading. The total uncertainty for

the thermocouples used in these experiments is considered as the summation of the uncertainties for each component listed.

Temperatures were measured using Omega Special Limits of Error (SLE) 24-gauge type T Class 1 thermocouples. The manufacturer quoted thermocouple accuracy is ±0.5°C (OMEGA Engineering inc., 2017). This accuracy is assumed to be the 95% confidence interval (2σ) based on the material composition of the thermocouple, and its accuracy in relation to the IT90 calibration curve for a T type thermocouple (Nicholas & White, 1994).

The thermocouples are measured using an Agilent 34970a data acquisition unit. The range accuracy and reading accuracy for this digital multimeter are ±0.004% and ±0.005% respectively for the 100mV range. The range accuracy is the accuracy of the unit over the full range, in this case 100mV. The reading accuracy is the accuracy of the unit for the given sensor reading. The range and reading results are added to determine the total uncertainty for a given reading. Combining the range and reading accuracy for the DAQ unit corresponds to a maximum uncertainty of ±4.1μV expected on a T-type thermocouple from -50°C to +50°C (Nicholas & White, 1994). In this range, the T-type thermocouple is expected to have a calibration slope of approximately 38.6 μV/°C. Combining these results the total uncertainty for the DAQ on a thermocouple reading is ±0.10°C.

The thermocouple measurement method also requires comparison with a cold junction reference temperature. The cold junction reference in the GHB consists of an aluminum block in lab conditions maintained at 23±2°C. The aluminum block temperature is measured with an Omega Class A RTD (100 Ω), with an uncertainty of ±0.20°C. The same Agilent DAQ is used for the cold junction and adds an uncertainty of ±0.011Ω on the

RTD reading. This corresponds to an additional uncertainty of ±0.04°C in the temperature range of 21°C to 25°C for the RTD used.

The thermocouple material, DAQ, and cold junction uncertainties are summated to give a combined thermocouple uncertainty of ±0.55°C.

### 5.2 Metering box heat input uncertainty

The GHB monitors the heat input to the metering box by measuring the current supplied to and voltage dissipation of a DC heater. The current is determined by measuring the voltage dissipation across a calibrated resistor in series with the DC heater. The voltage dissipation of the DC heater is directly measured across the heater.

The voltage dissipation across the calibrated resistor is measured using the same Agilent DAQ as the thermocouples. The calibrated resistor is a 0.5Ω resistor, with an accuracy of 0.05%. The heater is provided power from a Kenwood PD56-10 power supply, which supplies a maximum of 10A and 56 V to the heater. The voltage dissipation across the heater is also measured using the Agilent DAQ. Combining the measurement accuracy of the DAQ with the resistor uncertainty results in an uncertainty of ±0.008W for the heat input to the heater.

### 5.3 Combined metering box and flanking loss uncertainty

As described previously, the combined metering box and flanking losses are determined through measuring the voltage generation of a thermopile wired between the metering box walls, and comparing the GHB results with the expected calibrated specimen results. The uncertainty of this characterization is the combined uncertainty of the thermocouples on each surface of the specimen, the DAQ measurement of the thermopile

voltage, the heater uncertainty, and the calibrated specimen uncertainty. The thermocouple and heater uncertainty have been defined in the previous sections.

The thermopile to watts calibration has uncertainty due to the DAQ measurement of the thermopile voltage, the heater measurement uncertainty, and the uncertainty of the calibrated specimen results. From the thermocouple uncertainty analysis, the DAQ unit uncertainty in the millivolt range is ±4.1μV, which results in an uncertainty of ±0.007W for both -20°C and -35°C exterior temperatures.

The calibrated specimen uncertainty is the uncertainty of the ASTM C518 heat flow meter apparatus. The heat flow meter uncertainty for the calibration specimen used is ±2% (Lackey, Normandin, Marchand, & Kumaraman, 1994).

Combining the uncertainties of the thermocouples, DAQ, heater, and calibrated specimen gives an overall uncertainty for the metering box and flanking loss characterizations of ±1.39W for both exterior temperatures.

### 5.4 Specimen area measurement uncertainty

The specimen area is determined through multiplying measurements of the length and the width of the specimen. The measurements are taken with a standard metric tape measure with the smallest units being millimeters. The uncertainty for each measurement is taken as ±0.01m. The total area uncertainty is then ±1.0E-4$m^2$.

### 5.5 Thermal resistance combined uncertainty

The uncertainties of each component in Equation 13 are combined using the method described in Moffat (Moffat, 1988) for zeroth order constant odds. The uncertainty

on the calculated RSI from the GHB experiments conducted in this thesis are ±4.5% and ±3.3% for exterior temperatures of -20°C and -35°C respectively.

This result is low compared to that of Elmahdy (Elmahdy, 1992) and Elmahdy & Haddad (Elmahdy & Haddad, 2000), who estimated that the uncertainties for testing fenestration systems and sky lights in the same GHB used in this thesis were ±6.5% and ±6% respectively. The differences in uncertainty is due to the estimation of thermocouple uncertainty. The two references estimated an uncertainty of ±1.0°C for the thermocouples, whereas the uncertainty for thermocouples in this thesis is ±0.55°C. The references did not specify any uncertainty analysis of the DAQ or cold junction compensation.

The calculations for each uncertainty value, and the corresponding overall RSI uncertainty are given in Appendix E . The values for the uncertainties of each component used in the overall uncertainty calculation (Equation 13) are presented in Table 14 and Table 15.

**Table 14: -20°C Uncertainty parameters**

| | Experiment | Uncertainty (+/-) | Uncertainty max |
|---|---|---|---|
| **Exterior air temperature [°C]** | -20.08 | 0.55 | -20.63 |
| **Interior air temperature [°C]** | 20.83 | 0.55 | 21.37 |
| **Total heat added to the calorimeter [W]** | 40.35 | 0.01 | 40.36 |
| **Specimen area [$m^2$]** | 5.95 | 0.00 | 5.95 |
| **Combined metering box and flanking loss [W]** | -1.36 | 1.39 | -2.75 |

**Table 15: -35°C Uncertainty values**

| | Experiment | Uncertainty (+/-) | Uncertainty Max |
|---|---|---|---|
| **Exterior air temperature [°C]** | -34.87 | 0.55 | -35.42 |
| **Interior air temperature [°C]** | 20.88 | 0.55 | 21.43 |
| **Total heat added to the calorimeter [W]** | 55.73 | 0.01 | 55.74 |
| **Specimen area [$m^2$]** | 5.95 | 0.00 | 5.95 |
| **Combined metering box and flanking loss [W]** | 4.28 | 1.39 | 5.67 |

# 6 Chapter: Industry standard calculation method results

The industry standard calculation methods were used to calculate the thermal resistance of the wall assembly evaluated in the GHB tests. Section 2.1 outlined several methods by which the two and three-dimensional heat transfer at the edge of VIP panels could be approximated in one dimension. This chapter combines the industry standard calculation methods with the methods to incorporate increased heat transfer at the edges and joints of the VIPs, and compares the calculated results to the GHB test results. The calculations for each method are presented in more detail in Appendix F to Appendix I .

The material properties used in the calculation methods, and an estimation of their uncertainty are first presented. Thereafter the one-dimensional approximations for the VIP thermal conductivity including the heat transfer effect of the joints and edges are described. Finally, the thermal resistance is determined for each calculation method using each VIP thermal conductivity.

## 6.1 Material properties

The industry standard calculation methods used two material properties, thickness and thermal conductivity. The thickness values for each material did not change across all calculation methods. The thermal conductivities were constant throughout calculations, except for the VIPs.

The thermal conductivity for all components was not measured. For all components other than the VIPs, the thermal conductivity was obtained from either the ASHRAE Handbook of Fundamentals (ASHRAE, 2013), or manufacturer literature. The VIP thermal conductivities were obtained from manufacturer literature in combination with the thermal transmittance method to account for edge and joint effects. The thermal conductivities of

all components were not measured as a goal of the thesis was to obtain the accuracy of the calculation and simulation methods using the same information that would typically be available to a building designer or architect.

The VIP thermal conductivity was determined for six scenarios. The first scenario consisting of the manufacturer advertised centre of panel thermal conductivity at the beginning of service life. The second scenario consisted of the manufacturer advertised effective thermal conductivity accounting for edges and service life aging (termed the design value by the manufacturer). Scenarios three to five consisted of three thermal conductivities that were determined for the VIPs using the air gaps measured in the constructed specimen and the correlation proposed by Lorenzati et al. (Lorenzati, Fantucci, Capozzoli, & Perino, 2014). The final two scenarios consisted of two thermal conductivities determined for the VIPs based on the linear transmittance of the barrier foil quoted by Wakili et al. (Wakili, Bundi, & B.Binder, 2004).

The material properties used for the industry standard calculations and numerical simulations are presented in Table 16. The various in VIP thermal conductivity are described in more detail in the following sections.

**Table 16: Material properties used in calculation methods.**

| Material | Reference | Thickness [m] | Apparent thermal conductivity [W/mK] |
|---|---|---|---|
| **XPS (0.5 in, 2 in)** | ASHRAE Handbook of Fundamentals | 0.013, 0.051 | 0.029 |
| **VIP (1 in)** | Manufacturer | 0.025 | 0.0042 |
| | Manufacturer | 0.025 | 0.0061 |
| | Lorenzati, min. gap between VIP's | 0.025 | 0.0053 |
| | Lorenzati avg. gap between VIP's | 0.025 | 0.0058 |
| | Lorenzati max. gap between VIP's | 0.025 | 0.0072 |
| | Wakili 90nm Alu – 90nm | 0.025 | 0.0051 |
| | Wakili 300nm Alu – 300nm | 0.025 | 0.0053 |
| **Steel stud (0.0179in)** | ASHRAE Handbook of Fundamentals | $4.55*10^{-4}$ | 48.0 |
| **Mineral fibre (3.625 in)** | Manufacturer | 0.089 | 0.036 |
| **Gypsum (5/8 in)** | ASHRAE Handbook of Fundamentals | 0.016 | 0.16 |

### 6.1.1 VIP thermal conductivity

The calculated thermal resistance of the wall assembly was determined for the different VIP effective thermal conductivities. The methods by which the effective thermal conductivities were determined are described in the following sections. The sections are divided into the manufacturer quoted thermal conductivities, the effective thermal conductivities determined including the air gaps, and the effective thermal conductivities determined based on the barrier foil thickness.

### 6.1.2 Manufacturer thermal conductivity

There are two values which the manufacturer lists for the VIP panels used in the wall assembly evaluated in this thesis. The thermal conductivities are referred to by the

manufacturer as the centre of panel thermal conductivity, and the design thermal conductivity.

The centre of panel thermal conductivity is the lowest thermal conductivity used in the calculations, and it represents an idealized value which does not account for edge, joint effects, or service life effects. The value is listed as 0.0042 $W/m^2K$, and results which use this thermal conductivity in later sections are titled “004 w_air”.

The design thermal conductivity is listed by the manufacturer as an effective thermal conductivity, which accounts for edge and service life effects. No details are provided as to how this value is determined, and if it accounts for joints between panels. The value is listed as 0.0061 and calculations using this thermal conductivity in later sections are titled “Manufacturer max”.

### 6.1.3 Vacuum insulated panel effective thermal conductivity – Lorenzati

The Lorenzati work determined a correlation to estimate the effective thermal conductivity of a VIP given details of the perimeter to area ratio and the joint width and material between abutting panels. The perimeter to area ratio was taken for that of a 1200 mm wide by 600 mm tall panel. The air gaps between VIPs were measured in several locations, however were found to vary, due to both construction tolerances, and irregularities in the edges of the VIPs. An example of the air gap variation is shown in Figure 21. The average, maximum and minimum air joint width determined from measurements are shown in Table 17.

**Figure 21: Example of joint width variation between VIPs in wall assembly.**

**Table 17: Air joint size variation.**

| | Gap width (mm) |
|---|---|
| **Minimum joint width** | 4.44 |
| **Average joint width** | 7.20 |
| **Maximum joint width** | 11.07 |

The minimum, average and maximum air joint widths were used to determine the corresponding effective thermal conductivity of the VIPs using the Lorenzati et al. values from Table 3. The values from Table 3 were plotted to determine a correlation between the

air joint width, and the corresponding increase in centre of panel thermal conductivity accounting for the air joints for the 1200mm x 600mm panels. The effective thermal conductivity for each joint width in Table 17 was calculated by multiplying the corresponding percent increase in Figure 22 by the manufacturer advertised centre of panel thermal conductivity at the beginning of service life.

The plot of the values from Table 3 and the corresponding effective thermal conductivity for the minimum, average and maximum joint width of the wall assembly are given in Figure 22 and Table 18. The results derived from using the minimum joint width, average joint width and maximum joint width effective thermal conductivities in the following sections are referred to as "Lorenzati minimum", "Lorenzati average" and "Lorenzati maximum" respectively.

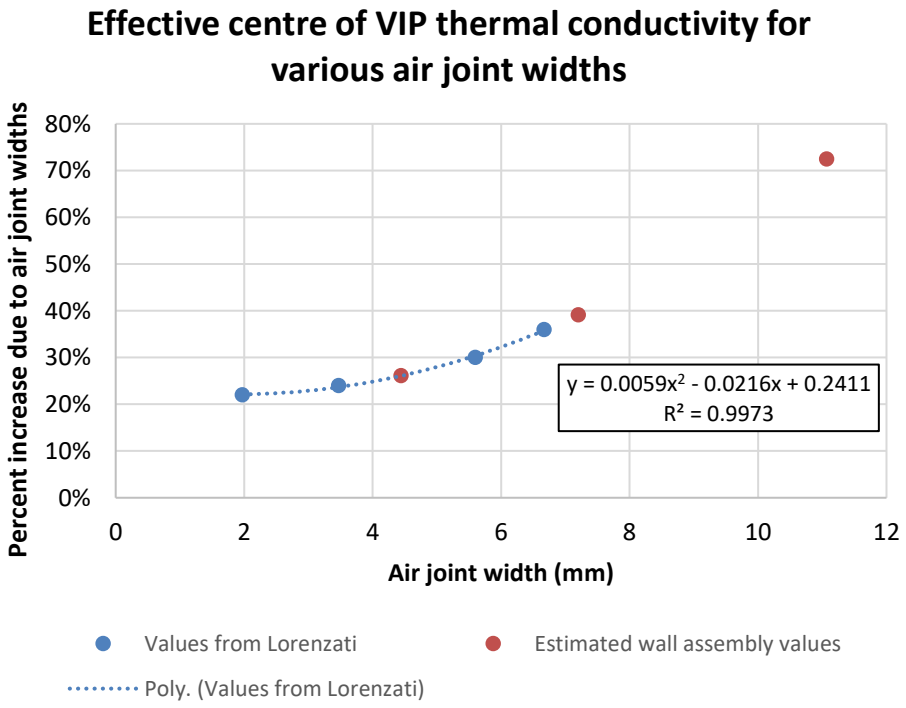

**Figure 22: Increase in centre of panel thermal conductivity**

**Table 18: Effective thermal conductivity of VIP from Lorenzati correlation**

| Measured joint width | Increase in centre of panel thermal conductivity | Effective thermal conductivity of VIP (W/mK) |
|---|---|---|
| **Minimum** | 26% | 0.0053 |
| **Average** | 39% | 0.0058 |
| **Maximum** | 72% | 0.0072 |

### 6.1.4 Vacuum insulated panel effective thermal conductivity – Wakili

The VIP effective thermal conductivity was also estimated using the linear thermal transmittance method, and values for the linear thermal transmittance of the barrier edge foil from Wakili et al. (Wakili, Bundi, & B.Binder, 2004). The values for thermal transmittance considered are for barrier foils that contain two different thickness of the metalized layer. The two thicknesses are 90nm and 300nm.

The manufacturer advertised centre of panel value at the beginning of service life and the linear transmittance values for each barrier foil type from Table 1 were used in Equation 3 to determine the effective thermal conductivity of the VIPs. The resulting effective thermal conductivities are given in Table 19.

**Table 19: Effective thermal conductivity of VIP using thermal transmittance**

| Barrier foil thickness [nm] | Effective thermal conductivity [W/mK] |
|---|---|
| **90 nm** | 0.0051 |
| **300 nm** | 0.0053 |

The results in the following sections derived from using the effective thermal conductivities determined by the thermal transmittance published by Wakili et al. (Wakili, Bundi, & B.Binder, 2004) are referred to as “90nm” and “300nm”.

## 6.2 Industry standard calculation methods – Uncertainty

The uncertainty for the industry standard calculation methods is assumed to be due to the uncertainty in the material properties, and the effective thermal conductivity calculation methods. None of the material properties are listed in the various literature locations with uncertainties. To estimate the uncertainty, it was assumed that all the material properties quoted in Table 16 were measured using a heat flow meter (ASTM C518), with an uncertainty of ±2% (Lackey, Normandin, Marchand, & Kumaraman, 1994).

The calculations for effective thermal conductivity using the published values of Lorenzati et al. (Lorenzati, Fantucci, Capozzoli, & Perino, 2014) and Wakili (Wakili, Bundi, & B.Binder, 2004) are correlations derived using tests from a heat flow meter. Again, the minimum uncertainty in these values is estimated at ±2%. The effective thermal conductivities are calculated for the VIP only. Using the centre of cavity thermal resistance, the VIP accounts for just over 50% of the nominal thermal resistance of the assembly. Therefore, it is estimated that the calculation methods add an additional uncertainty of ±1% to the overall thermal resistance value of the wall.

For the results of the hand calculation methods, the uncertainty of the material properties applies in all calculations. The additional uncertainty due to the effective thermal conductivity calculations applies to only the cases for which an effective thermal conductivity is used. Therefore, it is estimated that the uncertainty of the calculation methods that use the 004 w_air and Manufacturer max thermal conductivity have an uncertainty of ±2%. Calculation methods which use the remaining effective thermal conductivities are assumed to have an uncertainty of ±3%. This result is derived as a

conservative uncertainty estimate, as it uses the direct addition of the material property uncertainty and the effective thermal conductivity calculation method uncertainty.

### 6.3 Industry standard calculation methods – Results

The industry standard calculation methods were completed with the various VIP thermal conductivities and compared to the results of GHB tests. The industry standard calculation methods calculated the surface to surface thermal resistance and the GHB determined the air to air thermal resistance results. To compare the results of both methods the average surface heat flux coefficients from the GHB characterization were added to the industry standard calculation results.

The added thermal resistance due to the surface heat flux coefficients added to the industry standard calculation results was determined by summating the inverse of each surface heat flux coefficient from Table 8. This resulted in an additional 0.14 $m^2K/W$, and 0.16 $m^2K/W$ for the -20°C and -35°C exterior temperatures respectively. Due to the similarity in the thermal resistance results from the GHB tests the results are compared for the -20°C exterior temperature only.

The industry standard calculation methods thermal resistance results are presented in Table 20. The calculation steps for each method are shown in Appendix F to Appendix I .

**Table 20: Results comparison of industry standard calculation methods to -20°C exterior temperature GHB test results.**

| **Industry standard calculation method results - RSI [$m^2K/W$]** | | | | |
|---|---|---|---|---|
| **Experiment result** | **6.86** | | | |
| | **Parallel path** | **Isothermal planes** | **BRE 465** | **Modified zone** |
| **0.004 w_air** | 11.1 | 10.78 | 11.03 | 9.47 |
| **Lorenzati min** | 9.85 | 9.55 | 9.79 | 8.22 |
| **Lorenzati average** | 9.41 | 9.10 | 9.35 | 7.77 |
| **Lorenzati max** | 8.58 | 8.28 | 8.52 | 6.93 |
| **Manufacturer max** | 9.85 | 9.55 | 9.79 | 8.22 |
| **90nm** | 10.06 | 9.76 | 10.00 | 8.43 |
| **300nm** | 9.81 | 9.50 | 9.75 | 8.17 |
| **Industry standard calculation method results [$hrft^2°F/BTU$]** | | | | |
| **Experiment result** | **38.9** | | | |
| | **Parallel path** | **Isothermal planes** | **BRE 465** | **Modified zone** |
| **0.004 w_air** | 63.0 | 61.2 | 62.6 | 53.8 |
| **Lorenzati min** | 55.9 | 54.2 | 55.6 | 46.7 |
| **Lorenzati average** | 53.4 | 51.7 | 53.1 | 44.1 |
| **Lorenzati max** | 48.7 | 47.0 | 48.4 | 39.3 |
| **Manufacturer max** | 55.9 | 54.2 | 55.6 | 46.7 |
| **90nm** | 57.2 | 55.4 | 56.8 | 47.9 |
| **300nm** | 55.7 | 54.0 | 55.4 | 46.4 |

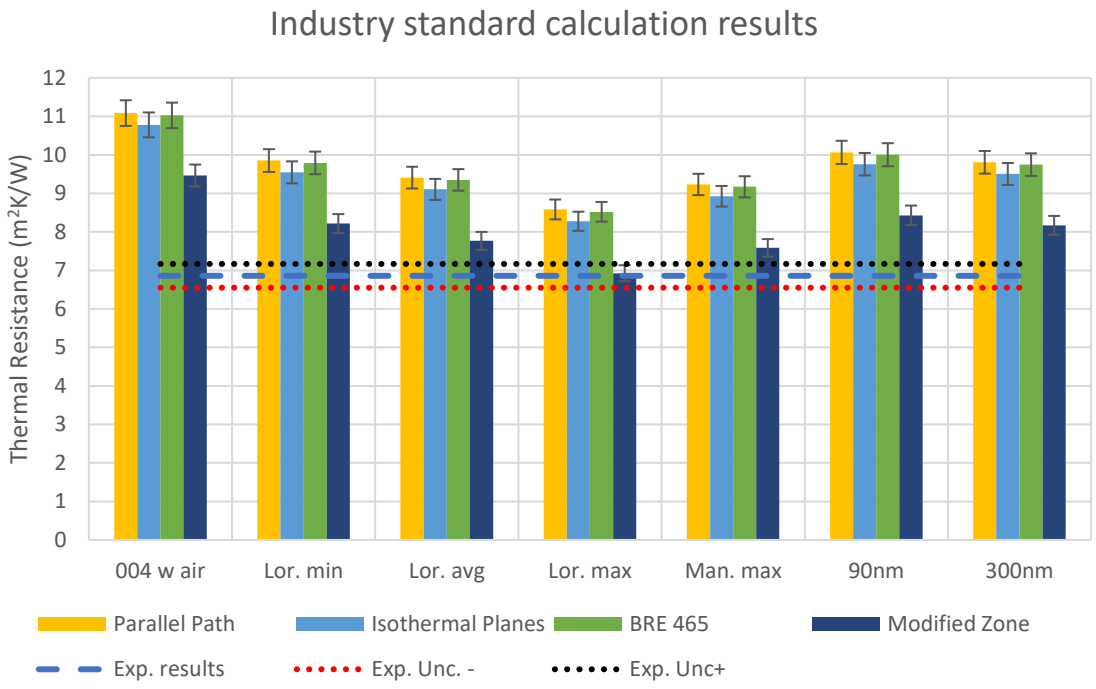


**Figure 23: Comparison graph for each calculation method using the various VIP thermal conductivity estimates.**

The following sections analyze the results to determine the accuracy of the different calculation methods in predicting the thermal resistance of the wall assembly and the accuracy benefits of using effective thermal conductivities for the VIPs.

### 6.3.1 Industry standard calculation method comparison

The calculation methods are compared using the results from the 004 w_air VIP thermal conductivity, as this represents the value which would be used by designers in most cases. The parallel path calculation method resulted in the highest over estimation of the thermal resistance of the wall assembly, resulting in a thermal resistance of RSI 11.09 (R63), which represents an overestimation of approximately 62%. The BRE 465 calculation method resulted in the second highest over estimation of the thermal resistance (61%), followed by the Isothermal planes method (57%). The reason for these calculation

methods overestimating the thermal resistance of the wall assembly is that they did not account for lateral heat flow that can occur due to the steel stud thermal bridge in the wall assembly, which can cause the steel stud to have a larger thermal effect than can be accounted for using the physical area.

The modified zone method, which accounts for the effective thermal zone of the steel stud instead of only its physical area, resulted in thermal resistance values closer to the experiment values. The modified zone method predicted a thermal resistance of 9.47$m^2$K/W (R54), which represents an overestimation of 38%.

These results indicate the importance of accounting for thermal bridges, both in the calculation method, as well as due to the VIP's. The results for the calculation methods using the effective thermal conductivities are described in the following section.

### 6.3.2 Vacuum insulated panel effective thermal conductivity

The VIP thermal conductivity scenarios were used in each calculation method, however the results will be described using only the modified zone method, as it resulted in the closest approximation of the thermal resistance. However, the trends determined for the modified zone method are applicable to all other calculation methods.

The results for the modified zone calculation method (Figure 24) indicate that the methods which account for the edge and joint effect in the VIPs result in more accurate thermal resistance results when compared to the GHB results.

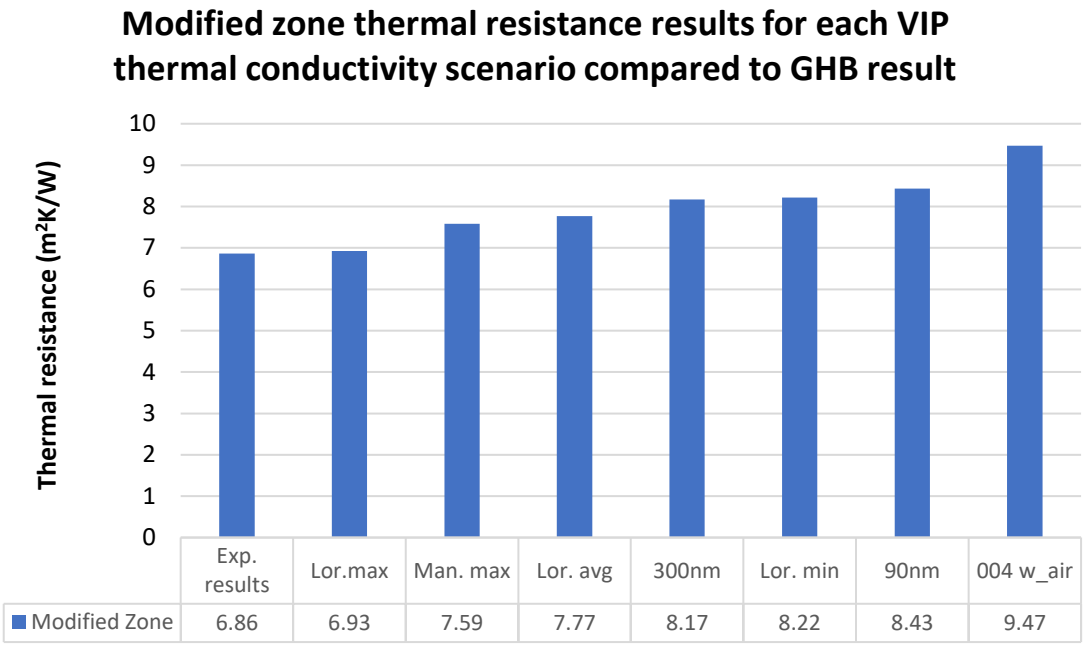


**Figure 24: Comparison of VIP thermal conductivity scenarios.**

Figure 24 shows that the highest over estimation of the thermal resistance occurs with the manufacturer advertised centre of panel value (004 w_air). The manufacturer advertised value (004 w_air) results in an overestimation of the thermal resistance by 38%. The manufacturer design value (Manufacturer max) results in an overestimation of the thermal resistance by approximately 20%.

The thermal transmittance methods result in overestimations of the thermal resistance by approximately 23% and 20%, for the 90nm and 300nm values respectively. This represents a change of only approximately 3% with an increase in the metallized foil thickness of over 200nm.

The VIP effective thermal conductivities that account for air joint thickness result in over estimations of the effective thermal conductivity of 20%, 13%, and 1% for the Lorenzati min, Lorenzati average, and Lorenzati Max respectively. The results indicate that

Lorenzati max effective thermal conductivity was the most accurate, however it is not recommended to be used for field calculations. The Lorenzati max effective thermal conductivity was determined by using the maximum joint thickness (air gap) measured, which should have resulted in an underestimation of the thermal resistance. Instead, the most appropriate method is to use the average joint width, which results in a 13% overestimation of the thermal resistance.

Overall the results indicate that the effective thermal conductivity of the VIP result in increased accuracy for the thermal resistance calculations. For methods which calculate the effective thermal conductivity of the VIP, the results indicate that it is more important to account for the air joint size than the foil barrier thickness for the air gaps measured. The increase from 90nm to 300nm foil thickness resulted in only a 3% change in the thermal resistance results, whereas the change from the Lorenzati min to Lorenzati max resulted in a change of 16%.

From the results, if an industry standard calculation method is to be used in estimating the thermal resistance of a steel stud wall incorporating VIPs, the modified zone method should be used with the Lorenzati effective thermal conductivity correlation using the average joint thickness. It should be noted however that the use of this scenario results in a 13% overestimation of the thermal resistance of a wall assembly.

# 7 Chapter: Two and three-dimensional numerical simulations set up

Numerical simulations were completed on the wall assembly in both two and three dimensions. The numerical simulations were conducted to determine if the accuracy of the thermal resistance prediction of the wall assembly using simulation methods improved over the industry standard calculation methods. Additionally, the models' accuracy in predicting the temperatures on the interior surface, and through the depth of the mineral fibre were examined. The two-dimensional (2D) simulations also evaluated the potential for using the effective thermal conductivity for the VIPs. The three-dimensional (3D) simulations used only the 004 w_air VIP thermal conductivity. Once again, the simulations were compared to the GHB test results.

The numerical simulations were conducted using the heat transfer package of the finite element software COMSOL Multiphysics® (COMSOL AB, 2017). The simulations were conducted at steady state for two temperature differentials using the boundary conditions from the GHB experiments. The settings for COMSOL Multiphysics® including governing equations, geometry, material properties and boundary conditions are presented in Appendix J .

## 7.1 Numerical simulation method

The numerical simulation method was similar for both 2D and 3D modelling. The modelling sequence consisted of: selecting and creating the geometry to be modelled, selecting the material properties, determining and applying the boundary conditions, performing a mesh verification, conducting the numerical simulations and comparing the

results to the GHB test results. The following sections describe each step for the 2D and 3D modelling.

## 7.2 Governing Equations

The numerical simulations were completed assuming all heat transfer through the solid components was due to conduction. The numerical simulations solved the general governing equation for heat conduction (COMSOL AB, 2017), given for one dimension in Equation 14.

$$q" = -\lambda * \frac{dT}{dx} \qquad \textbf{Equation 14}$$

$q"$ – heat flux [W/m$^2$]
$\lambda$ – thermal conductivity [W/mK]
$dT$ – temperature difference between nodes [K]
$dx$ – length between nodes [m]

## 7.3 Air space heat transfer modelling

The heat transfer across the air spaces was also modelled as conduction. This assumption was made after a dimensional analysis of the air gap to calculate the Rayleigh number ($Ra$). A Rayleigh number above the critical value of $Ra_c$=1708 indicates the onset of convection, which contributes to increased heat transfer through the space. The Rayleigh number is calculated according to Equation 14. The properties for air were taken at the mean temperature between the surface temperatures, and are given in Table 21, and Figure 25 depicts the location of the temperatures used.

$$Ra = \frac{g\beta(T_{s,h} - T_{s,c})L^3}{\nu^2} Pr \qquad \textbf{Equation 15}$$

$g$ – gravity [m/s$^2$]
$\beta$- thermal expansion coefficient [1/K]
$T_{s,h}$ – temperature of the interior surface [K]

$T_{s,c}$ – temperature of exterior surface [K]
$L$ – characteristic length [m]
$\nu$ – kinematic viscosity of air [m/s$^2$]
$Pr$ – Prandtl number

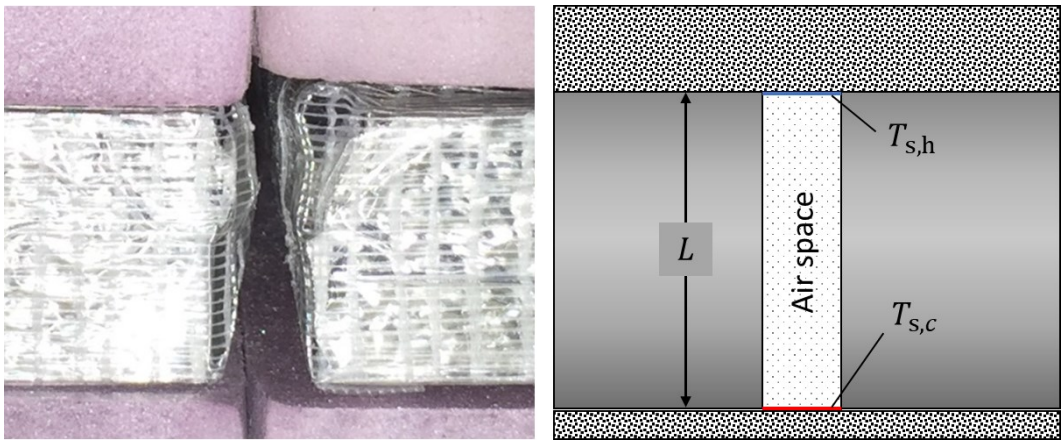


**Figure 25: A diagram indicating the parameters used to calculate the Rayleigh number for the air gap between VIPs.**

**Table 21: Parameters used to calculate Rayleigh number**

| Parameter | Value |
|---|---|
| $g$ [m/s$^2$] | 9.81 |
| $\beta$ [1/K] | 3.70E-03 |
| $\nu$[m/s$^2$] | 1.31E-05 |
| $Pr$ | 0.714 |
| $T_{s,c}$ | 265.9 |
| $T_{s,h}$ | 275.2 |
| $T_{mean}$ | 270.6 |

The average surface temperatures and corresponding mean temperature of the air were determined from the results 004 w_air two-dimensional simulation (see section 7.4 for geometry details). The results of the Rayleigh calculations are given in Table 22.

**Table 22: Results of Rayleigh calculations**

| Joint length | $Ra$ |
|---|---|
| $L$=25 mm | 21959 |
| $L$=11 mm | 1722 |

The results of the dimensional analysis indicate that at an air joint length of 25 mm, the Rayleigh number is above the critical value. However, for gap lengths less than 11 mm, the Rayleigh number is approximately equal to the critical value. Based on the representative photo of the VIP joint given in Figure 25, it is assumed that a joint length of 25 mm only occurs for a small section at the centre of the joint. The rest of the joint looks to have a length less than 11 mm. Therefore, it was assumed that heat conduction is representative of the heat transfer occurring in the through the joint.

## 7.4 Modelled Geometries

This section describes the geometries used to represent the wall assembly in the 2D and 3D numerical modelling. Each section describes the representative geometry, and assumptions made to create the representative geometry.

### 7.4.1 Two-dimensional geometries

The 2D numerical simulations were conducted on a plan view of the wall assembly for two configurations (Figure 26), and were drawn in COMSOL (COMSOL AB, 2017). The plan view orientation was selected to account for the effect of thermal bridges due to the steel studs. This orientation assumption ignores thermal bridges that occur due to the fiberglass clips and horizontal air spaces. The effect of this assumption will be investigated with the 3D modelling. Note, the naming convention for the various VIP thermal conductivities established in the previous chapter is also used here.

The first configuration consisted of simulating the wall assembly with the VIP layer containing VIPs separated by an airspace (Figure 26 B). The VIPs in this configuration

were simulated with thermal conductivity as per the manufacturer advertised centre of panel value (004 w_air).

The second configuration consisted of simulating the wall assembly with the VIP layer as a single material, modeled with effective thermal conductivities. The effective thermal conductivities accounted for combined centre of panel, edge and air joint heat transfer effects, as described in the previous chapter (Manufacturer max, Lorenzati min, Lorenzati average, Lorenzati max, 90nm, 300nm).

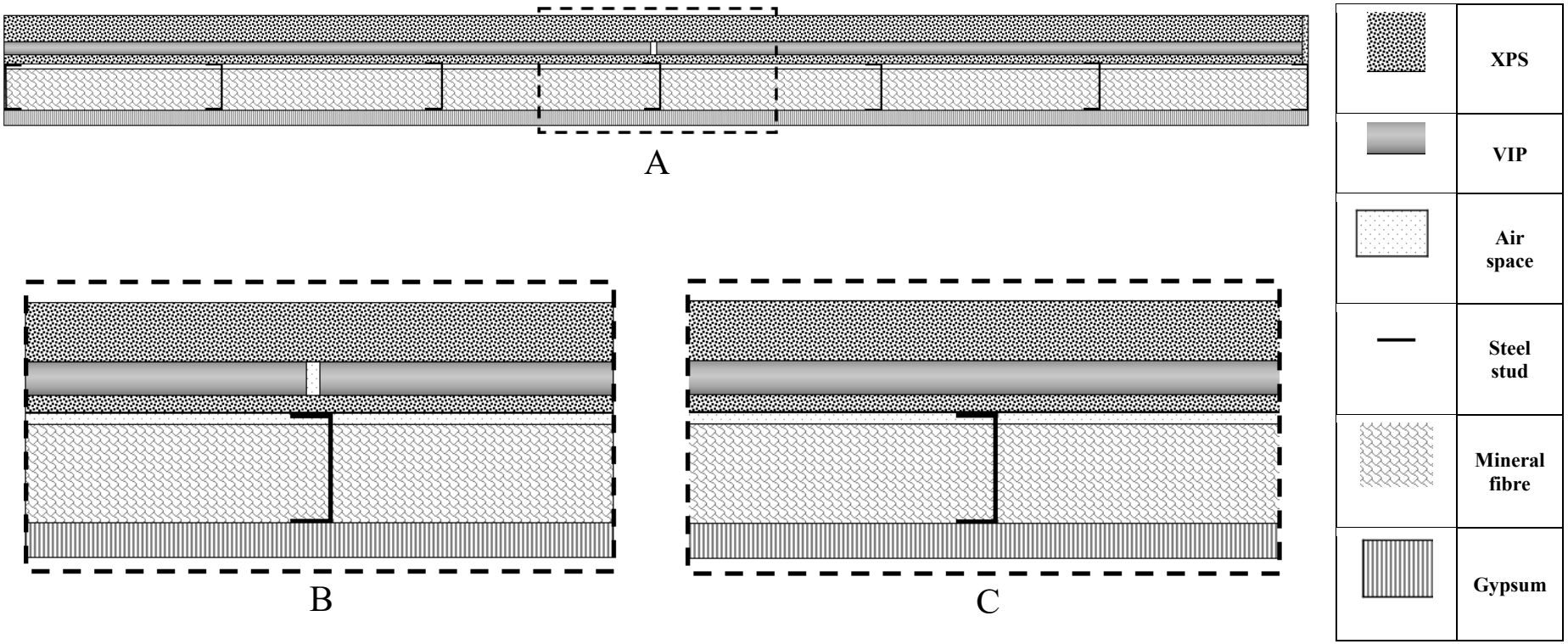


**Figure 26: Two-dimensional plan view geometry. Schematic A is the total geometry evaluated. Schematic B is a close-up section at the centre stud, which depicts the geometries that have a VIP and air space layer. Schematic C represents a close-up of the wall assembly centre stud configuration when the VIP and air space layer is modelled as an effective thermal conductivity layer.**

### 7.4.2 Three-dimensional geometry

The three-dimensional geometry was created in as close a replication as possible to the wall assembly that was tested in the GHB. This required defining both the vertical and horizontal air joints surrounding the VIPs. Due to the significant difference between the thickness of the steel stud (0.45 mm or 0.0179 in) to the overall wall assembly (~2.54 m by 2.54 m or 96 in by 96 in) a representative structure smaller than the full wall assembly was required for meshing to be achievable. Additionally, the gauge of the steel stud was increased to facilitate meshing. Fortunately, the substructure of the wall assembly consisted of a very similar construction (repeating steel studs every 400 mm or 16 in on centre). This allowed an assumption to be made that the thermal performance of the wall assembly could be modelled by selecting a representative section of the wall assembly, and assuming thermal symmetry at the lateral edges. The boundary conditions used in the modelling are described in the following section. The sub-assembly selected consisted of the centre stud of the wall assembly, with a half stud cavity to each side, as depicted in Figure 27 and Figure 28. The geometry was created in SolidWorks® (Dassault Systemes, 2016) and was imported into COMSOL Multiphysics® for simulation.

The effect of assuming the centre stud as representative to the whole assembly, using thermal symmetry boundary conditions and increasing the steel stud gauge size were investigated using two dimensional simulations. The results of these assumptions are presented in Chapter 8.

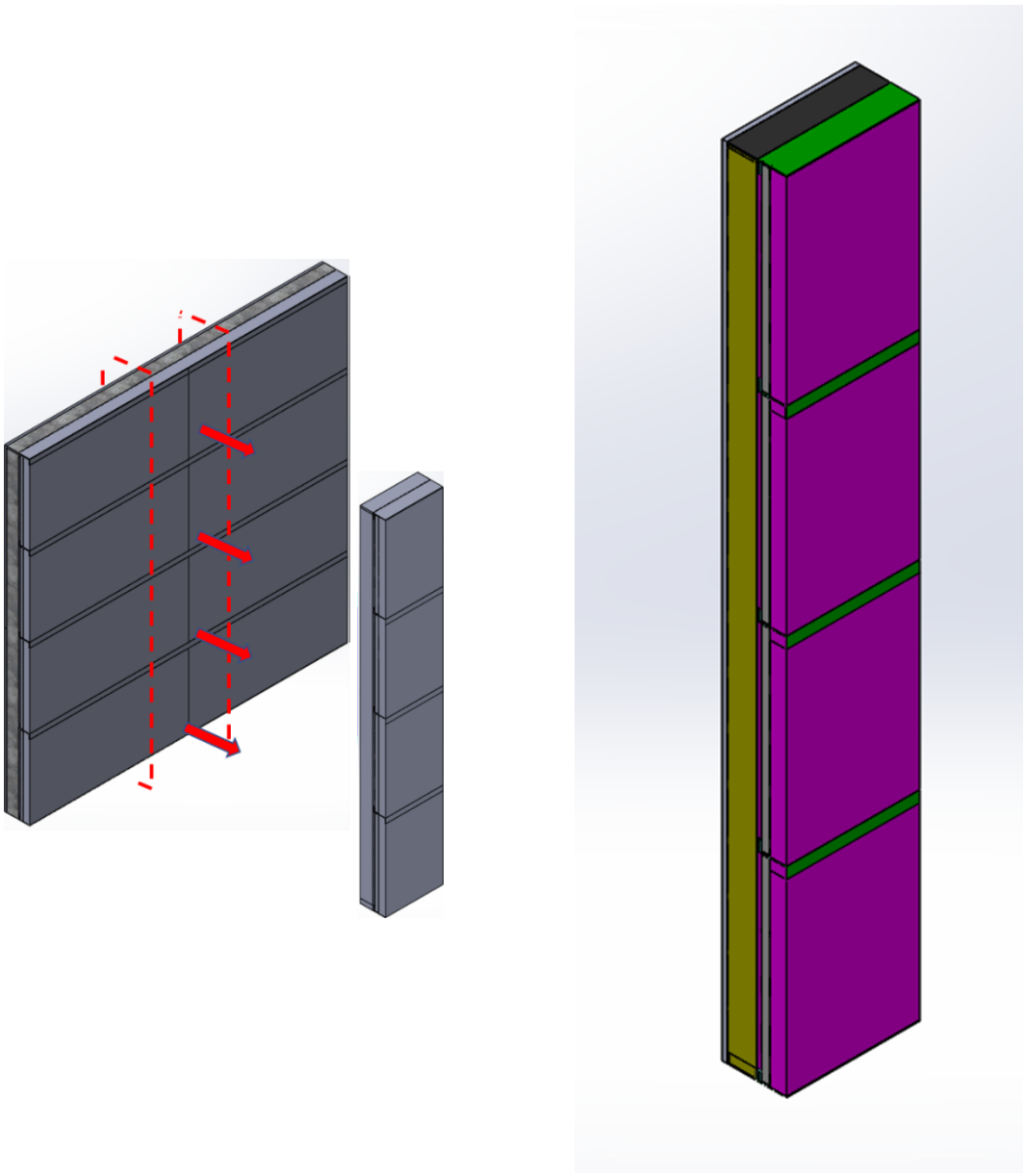

**Figure 27: Centre stud three-dimensional section.**

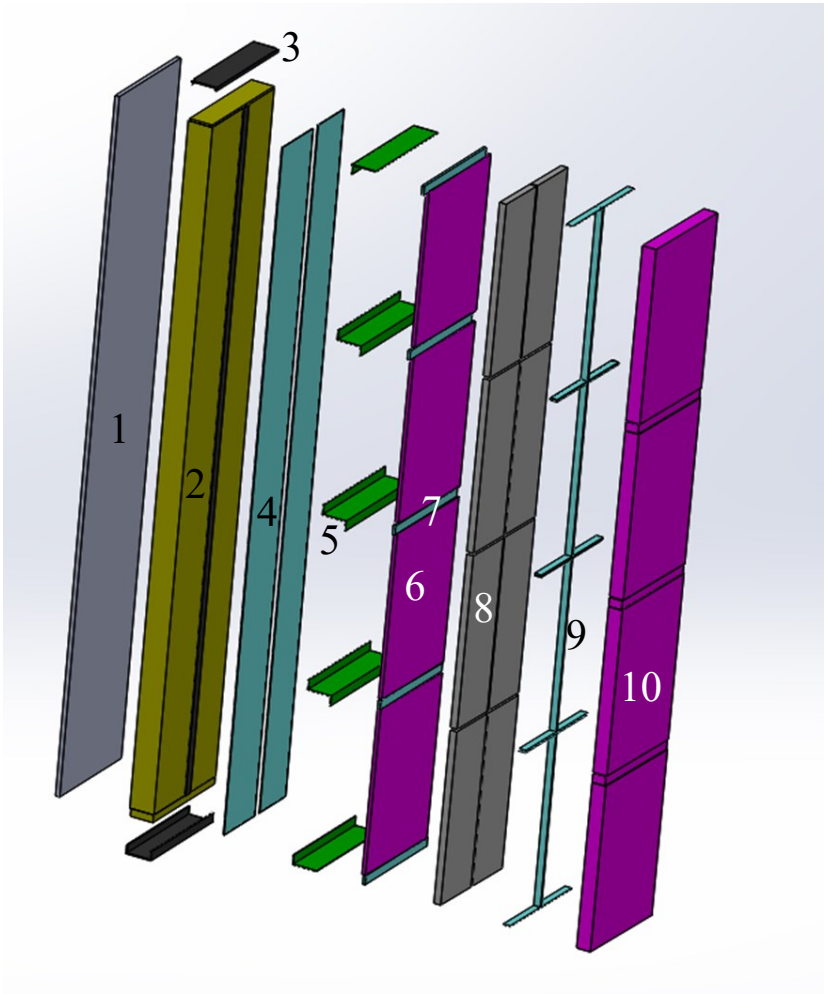


**Figure 28: Centre stud section exploded view.**

**Table 23: Label and description for three-dimensional exploded view**

| Label | Material |
|---|---|
| **1** | Gypsum |
| **2** | Mineral fibre |
| **3** | Steel stud |
| **4** | Air space affront of mineral fibre |
| **5** | Fiberglass clips |
| **6** | Interior XPS |
| **7** | Air space |
| **8** | VIP |
| **9** | Vertical and horizontal air space around VIP |
| **10** | Exterior XPS |

## 7.5 Numerical modelling boundary conditions

The boundary conditions (BCs) in the numerical models were implemented to mimic the BCs that the wall assembly was subjected to during the GHB testing. During the GHB test the surfaces of the wall assembly were exposed to three different boundary conditions. The interior surface is exposed to metering box air, the exterior surface is exposed to weather side air, and the lateral surfaces are exposed to the insulated mask. The boundary conditions implemented consisted of a Neumann boundary condition, where the heat flux, or heat flux and ambient temperature were specified.

Referring to Figure 4, the interior boundary condition is imposed on the surface exposed to the metering box, the exterior boundary condition is imposed on the surface exposed to the weather side, and the lateral boundary condition is imposed on the surfaces exposed to the insulated mask. The boundary conditions are demonstrated on plan view drawings of the wall assembly but are representative of both the 2D and 3D modelling.

### 7.5.1 Interior and exterior surface boundary conditions

The interior and exterior surface boundary conditions are assumed to be the average surface heat flux coefficients determined on the characterization specimens and the ambient temperatures of corresponding air from the GHB. The surface heat flux coefficients were represented in the model as convective heat flux coefficients with the air temperature during the test as the ambient temperature. The boundary conditions for each temperature condition for the interior and exterior surfaces are presented in Table 24. The modelling imposes the surface heat flux coefficient and the ambient temperature, and

solves for the corresponding surface temperature and heat flux using conservation of energy at the surface.

**Table 24: Interior and exterior boundary conditions.**

| | -20°C | -35°C |
|---|---|---|
| **Interior air temperature [°C]** | 20.8 | 20.9 |
| **Interior heat flux coefficient [W/m²K]** | 8.93 | 7.46 |
| **Exterior air temperature [°C]** | -20.1 | -34.9 |
| **Exterior heat flux coefficient [W/m²K]** | -60.76 | -50.42 |

Figure 29 depicts a representative plan view schematic of the surface energy balance. The boundary condition is presented in Equation 16 for the exterior surface. The same condition exists at the interior surface, however the heat transfer direction would from the air to the specimen.

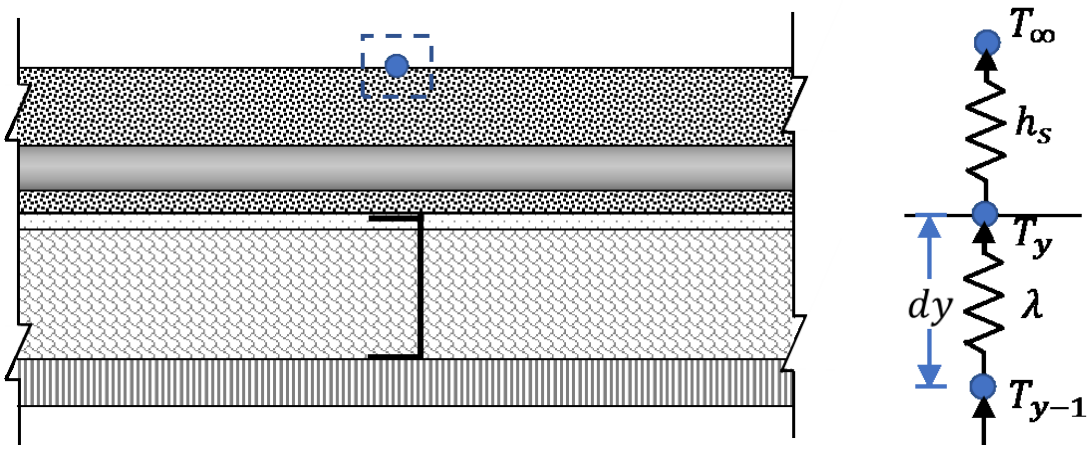


**Figure 29: Interior and exterior surface heat flux boundary condition imposed in numerical modelling.**

$$\lambda\left(\frac{T_{y-1} - T_y}{dy}\right) = h_s(T_y - T_\infty) \qquad \textbf{Equation 16}$$

$\lambda$ – is the apparent thermal conductivity of the material [W/mK]
$T_{y-1}$ – is the temperature at the previous element to the surface [°C]
$T_y$ – is the temperature at the surface element [°C]
$dy$ – is the distance between the elements [m]

$h_s$ – is the average surface heat flux coefficient from the GHB characterization tests [W/m$^2$k]
$T_\infty$ - is the ambient temperature of the air during the VIP wall GHB tests [°C]

### 7.5.2 Lateral surface boundary conditions

The lateral surfaces of the specimen in the GHB are in contact with the insulated mask. As discussed in the GHB characterization it is expected during the test that some heat transfer occurs between the test specimen and the mask. The heat transfer that occurs is accounted for in the characterization experiments, and subtracted from the thermal resistance calculation. Since the heat transfer across the mask is accounted for in the GHB results, the lateral surfaces boundary condition in the model is represented as a perfect thermal insulation condition, with zero heat flux normal to the lateral edges. A representative plan view schematic of the conservation of energy at the lateral surfaces is given in Figure 29. The perfect insulation boundary condition at the lateral surfaces is given in Equation 17.

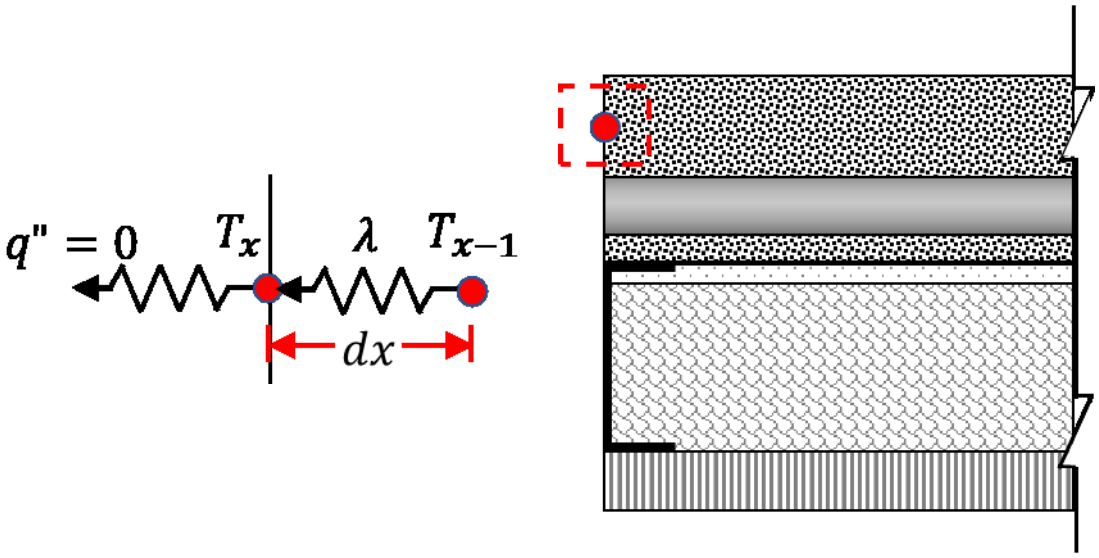


**Figure 30: Lateral surface boundary condition in numerical modelling.**

$$\lambda\left(\frac{T_{x-1}-T_x}{dx}\right)=0 \qquad \textbf{Equation 17}$$

$\lambda$ – is the apparent thermal conductivity of the material [W/mK]
$T_{x-1}$ – is the temperature at the previous element to the surface [°C]
$T_x$ – is the temperature at the surface element [°C]
$dx$ – is the distance between the nodes [m]

### 7.5.3 Thermal symmetry boundary conditions

The thermal symmetry boundary condition was imposed on the 3D representative geometry on the lateral sides. The numerical representation of the thermal symmetry condition is identical to a perfect insulation condition, where the boundary has zero heat flux occur across it. It is designated thermal symmetry to ensure that it is understood that the boundary condition is a slice of the wall assembly, not simply an insulated condition.

### 7.5.4 Boundary condition locations in two and three-dimensional models

The surfaces on which the boundary conditions were imposed in the 2D modelling are presented in Figure 31. The blue line depicts where the exterior surface heat flux boundary condition was applied, the red line depicts where the interior surface heat flux boundary condition was applied, and the green lines depict the where the perfect insulation condition was applied.

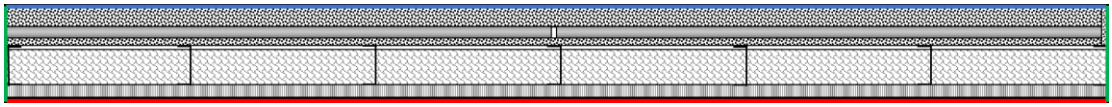

**Figure 31: Two-dimensional boundary condition locations**

The surfaces upon which the BCs were applied in the 3D modelling are presented in Figure 32. A thermal insulation boundary condition is imposed on the top and bottom surfaces of the assembly, thermal symmetry conditions are imposed at the lateral edges of

stud cavity to each side of the steel stud, and interior and exterior heat fluxes are imposed on the interior and exterior sides respectively.

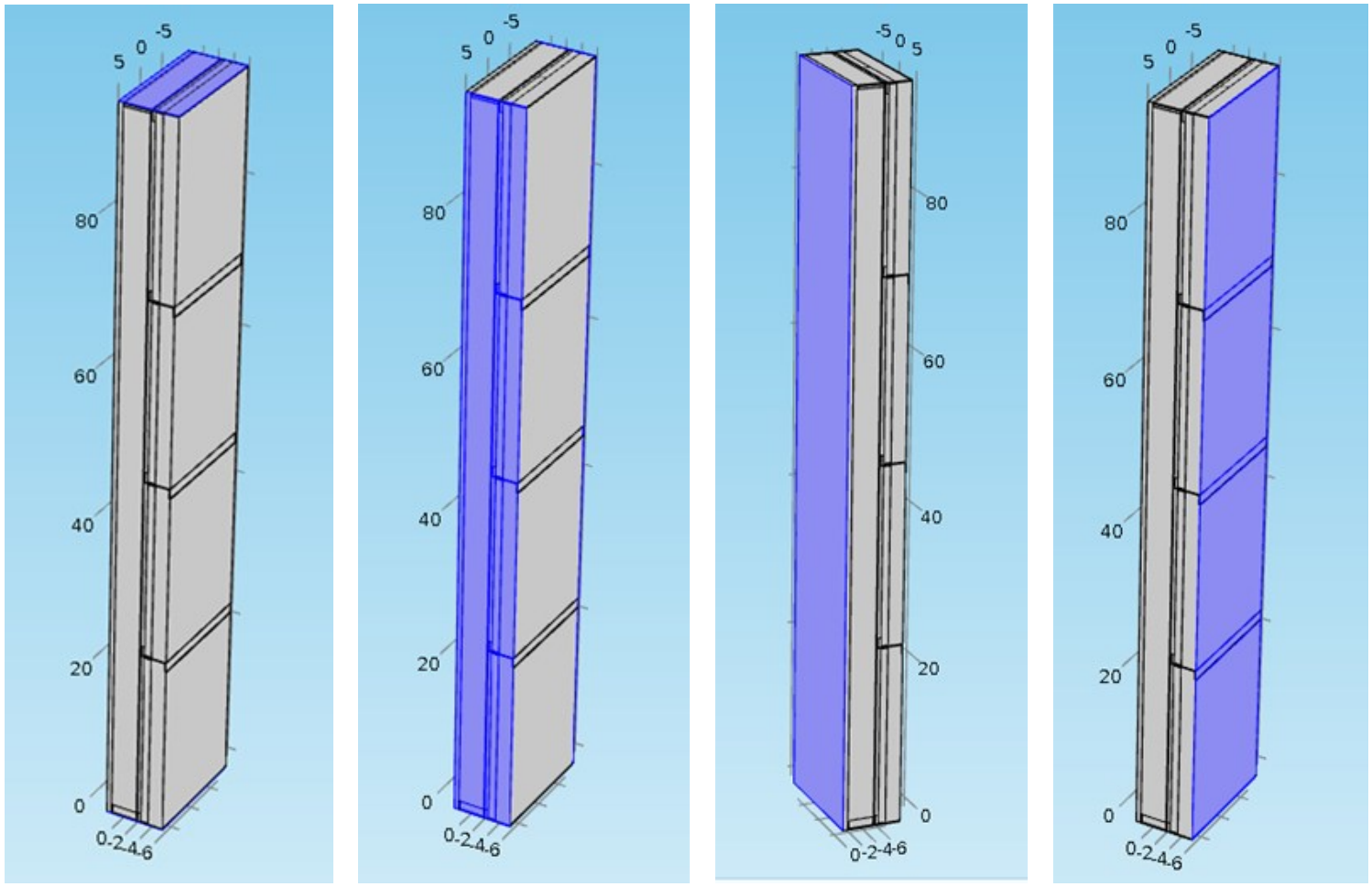


**Figure 32: Three-dimensional modelling boundary conditions: top left - thermal insulation BCs at top and bottom, top right - thermal symmetry BC's on each face of the centre of the stud cavity, bottom left - interior surface heat flux condition, bottom right - exterior surface heat flux condition.**

## 7.6 Mesh verification

The mesh verification process for the models consisted of conducting a grid independence study, as well as comparing the average heat flux in to and out of the geometry. The verifications were conducted for the-35°C exterior temperature, as this condition resulted in higher temperature gradients in the assembly than in the -20°C experiments. Since higher temperature gradients occurred in the -35°C simulations, it was assumed the mesh would be valid for the -20°C simulations. The two-dimensional mesh was constructed of triangular elements, and the three-dimensional mesh was constructed of tetrahedral elements.

### 7.6.1 Two-dimensional mesh verification

The 2D mesh verification used the geometry which contained the separated VIP and air space layer (Figure 26 B) as this geometry required a finer mesh than the combined VIP air space layer geometry.

The meshes used in this study consist of several built in COMSOL (COMSOL AB, 2017) automatic preset meshes, specifically the Coarser, Normal, Finer and Extreme Fine mesh. A final mesh consisted of reducing the largest and smallest allowable element size in the Extreme Fine mesh by a factor of 10 (Extreme Fine x10). The details for each mesh are presented in Table 25.

**Table 25: Mesh details.**

| | Coarser | Normal | Finer | Extremely fine | Extremely fine x10 |
|---|---|---|---|---|---|
| **Maximum element size (in)** | 0.315 | 0.163 | 0.0898 | 0.0243 | 0.00243 |
| **Minimum element size (in)** | 0.0146 | 0.000728 | 0.000303 | 0.0000485 | 0.00000485 |
| **Maximum element growth rate** | 1.5 | 1.3 | 1.25 | 1.1 | 1.05 |
| **Curvature factor** | 0.6 | 0.3 | 0.25 | 0.2 | 0.1 |
| **Resolution of narrow regions** | 1 | 1 | 1 | 1 | 1 |
| **Number of elements** | 48690 | 58091 | 64985 | 132828 | 376928 |

A visual comparison of the differences in the meshes is presented in Figure 33. The location used for the visual comparison is the centre of the wall assembly which contains a steel stud and the air joint between the VIP's.

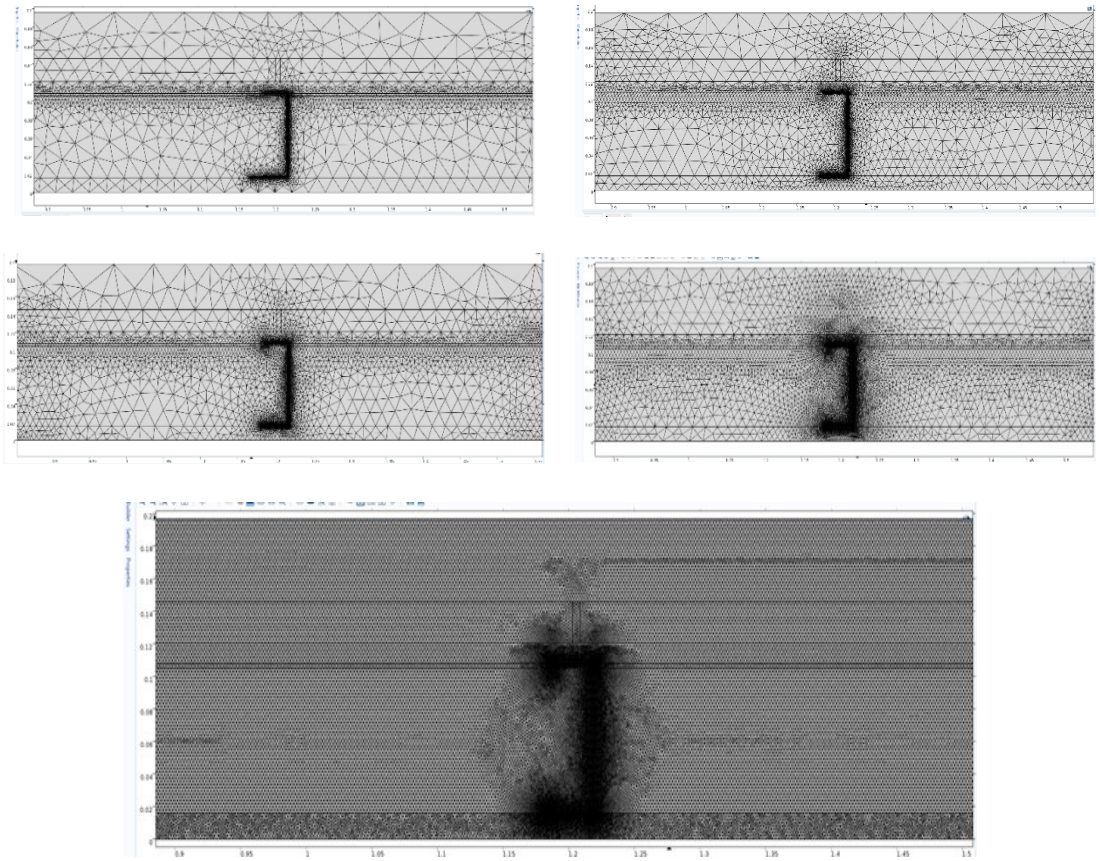

**Figure 33: Visual mesh comparison at centre of wall assembly.**

The mesh convergence plot is generated for the average heat flux density on the interior surface, which is used in the calculation of the thermal resistance at each temperature. Additionally, the heat flux into the interior surface is compared to the heat flux out of the exterior surface for a secondary verification comparison. The results of the mesh verification are presented in Figure 34 and Table 26.

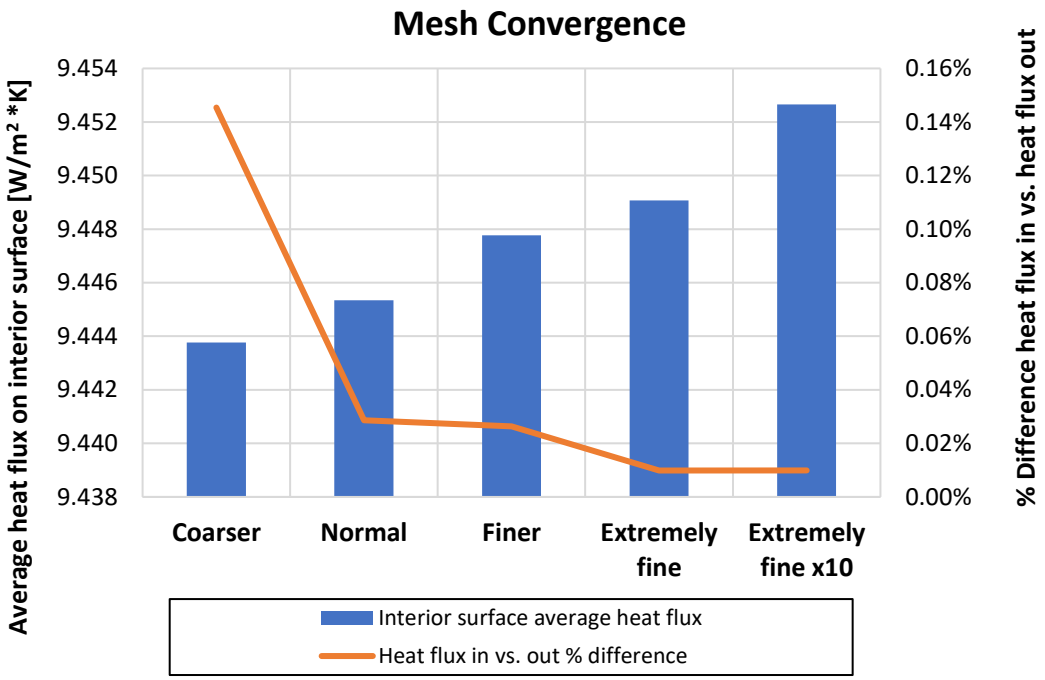


**Figure 34: Convergence plot for mesh comparison.**

**Table 26: Comparison of the heat flux into the wall assembly vs. the heat flux exiting the wall assembly.**

| | Interior heat flux density [W/m²] | % Difference between mesh vs. Extreme Fine x10 mesh | Heat flux in vs. Heat flux out |
|---|---|---|---|
| **Coarser** | 5.81 | 0.09% | 0.145% |
| **Normal** | 5.81 | 0.08% | 0.029% |
| **Finer** | 5.81 | 0.05% | 0.026% |
| **Extremely fine** | 5.81 | 0.04% | 0.010% |
| **Extremely fine x10** | 5.80 | N/A | 0.010% |

The plot in Figure 34 and corresponding data presented in Table 26 demonstrate that all meshes generate results for the average interior heat flux within approximately 0.005 W/m$^2$K (0.1%). The percent difference between the heat flux entering the wall assembly (average interior heat flux) and the heat flux exiting the geometry (average

exterior surface heat flux) for all mesh's used in this study are within approximately 0.15%. The final mesh indicates the heat flux in is within 0.01% of the heat flux out of the assembly.

The reason for the small spread in the results is due to the scale difference between the steel stud gauge (0.45 mm or 0.0179 in) and all other elements in the wall assembly (2.54 m or 96 in wide). This size discrepancy causes any mesh which has elements small enough to mesh the steel stud to result in a mesh which can adequately account for the physics on the larger assembly. The remaining 2D simulations were conducted using the Extremely fine x10 mesh.

### 7.6.2 Three-dimensional mesh verification

For the 3D mesh, custom mesh parameters had to be assigned, as the discrepancy between the steel stud gauge and the rest of the wall assembly caused errors when attempting to use built in COMSOL mesh settings. The parameters for each mesh investigated are shown in Table 27 and results are shown in Figure 35.

**Table 27: Mesh details for three-dimensional simulations.**

| | Mesh 1 | Mesh 2 | Mesh 3 | Mesh 4 | Mesh 5 | Mesh 6 |
|---|---|---|---|---|---|---|
| **Maximum element size (in)** | 1.92 | 1.5 | 1 | 0.5 | 0.5 | 0.4 |
| **Minimum element size (in)** | 0.005 | 0.005 | 0.005 | 0.005 | 0.005 | 0.005 |
| **Convergence criteria** | 0.001 | 0.001 | 0.001 | 0.001 | 0.0001 | 0.001 |
| **Maximum element growth rate** | 1.1 | 1.1 | 1.1 | 1.1 | 1.1 | 1.1 |
| **Curvature factor** | 0.2 | 0.2 | 0.2 | 0.2 | 0.2 | 0.2 |
| **Resolution of narrow regions** | 1 | 1 | 1 | 1 | 1 | 1 |
| **Number of elements** | 2825142 | 2828434 | 3109344 | 3901404 | 3901404 | 5223231 |
| **Thermal resistance** | 6.78 | 6.78 | 6.78 | 6.79 | 6.79 | 6.80 |

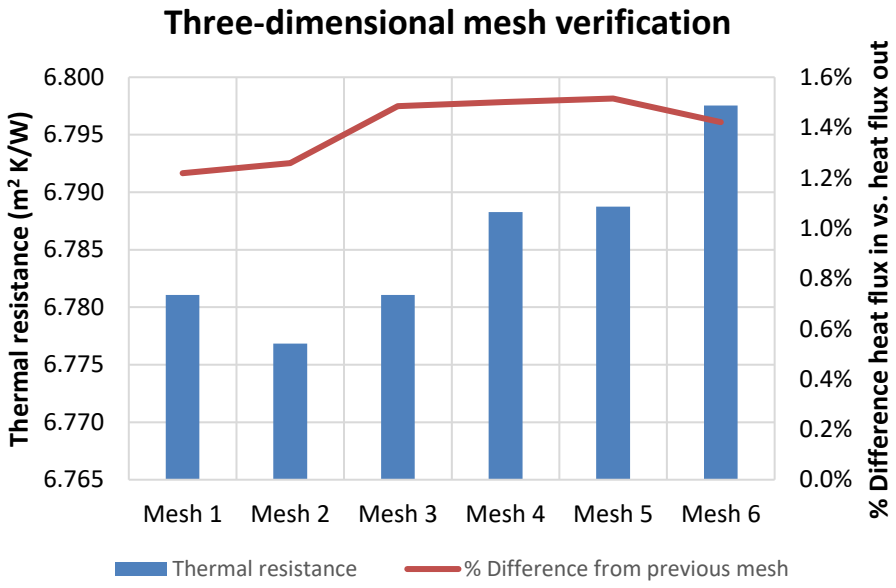


**Figure 35: Three-dimensional simulations mesh convergence results.**

From the results, it can be determined that the thermal resistance results are independent of the mesh as all results from Mesh 1 to Mesh 6 are within ± 0.02 $m^2K/W$.

The percent difference between the heat flux in versus heat flux out is also consistent across all meshes. The heat flux in versus. heat flux out comparison shows a difference (1.4%) even at Mesh 6. It is anticipated that a finer mesh could achieve closer results, however Mesh 6 was at the limits of the computers being used. The difference is accounted for in the 3D results as an additional uncertainty.

The effect of convergence criteria was also investigated by comparing Mesh 4 and Mesh 5. These two meshes have the same size parameters, however the convergence criteria for Mesh 5 was ten times stricter than that of Mesh 4. Comparing the results between these two meshes shows that convergence criteria is not affecting results.

Based on these results, Mesh 6 was used for simulations at both exterior temperatures.

# 8 Chapter: Numerical simulation results and uncertainty

Two and three-dimensional numerical modelling was conducted on the geometries described previously for exterior temperatures of -20°C and -35°C. The simulation results were compared with the results from the GHB tests. In addition to comparing the thermal transmittance of the wall assembly to GHB test results, the interior gypsum surface temperature profile in proximity to the steel stud, and the temperature through the depth of the mineral fibre were also compared. Uncertainty estimations for the 2D and 3D modelling results are also described in this section.

The investigation of the effect of the assumptions made to the 3D representative geometry using 2D modelling is presented previous to the 3D numerical simulation results.

## 8.1 Two-dimensional numerical simulation

Similar to the industry standard calculation methods, the 2D simulations were conducted to investigate the potential to increase the accuracy of the predicted thermal resistance of the wall assembly by using effective thermal conductivities for the VIP. The VIP configurations investigated in the 2D modelling were the same as were investigated with the industry standard calculation methods.

In addition to comparing the thermal resistance of the 2D wall configurations to the GHB test results, the effect of the steel stud thermal bridge on the interior temperature of the sheathing board, and the temperature profile through the depth of the mineral fibre were also compared. The results comparison for each wall assembly configuration simulated are presented in the following sections.

### 8.1.1 Uncertainty – Two dimensional simulations

The uncertainty in the 2D simulation results considers uncertainty due to the material properties, discretization of the geometry and convergence and rounding of the numerical solution.

The uncertainty due to the material properties is estimated to be ±2%, using the same rationale as that for the industry standard calculation methods.

The uncertainty due to the discretization, convergence and rounding error of the numerical solution is estimated from the difference between the heat flux in to and heat flux out of the geometry. It is assumed that discretization error is negligible in this case, as the difference in heat fluxes are less than 0.1%. The convergence of the simulations is 0.001%, and is also assumed to not add significant uncertainty to the simulation results in this case.

Therefore, the overall uncertainty for the 2D simulations is considered to be due to the uncertainty of the material properties, giving an overall uncertainty of ±2%.

### 8.1.2 Thermal resistance comparison: two-dimensional simulation versus guarded hot box results

The thermal resistance of the modeled geometry was calculated from the simulation results by determining the average interior surface heat flux density (heat flux entering the geometry normalized by the area) and the temperature difference between the air in the

metering box (interior), and the air in the weather side chamber (exterior). The results of the thermal resistance calculation are presented in Table 28 and Figure 36.

**Table 28: Comparison between thermal resistance experiment results and simulation results.**

| RSI (R-value) | Experiment | 004 w_air | Lor. max | Lor. average | Lor. min | 90nm | 300nm | Manufacturer max |
|---|---|---|---|---|---|---|---|---|
| -20°C | 6.86 (38.9) | 9.5 (53.7) | 7.4 (42.1) | 8.2 (46.7) | 8.6 (48.9) | 8.8 (49.9) | 8.6 (48.9) | 7.8 (44.4) |
| -35°C | 6.84 (38.9) | 9.5 (53.7) | 7.4 (42.0) | 8.2 (46.7 | 8.6 (48.9) | 8.8 (49.9) | 8.6 (48.9) | 7.8 (44.4) |

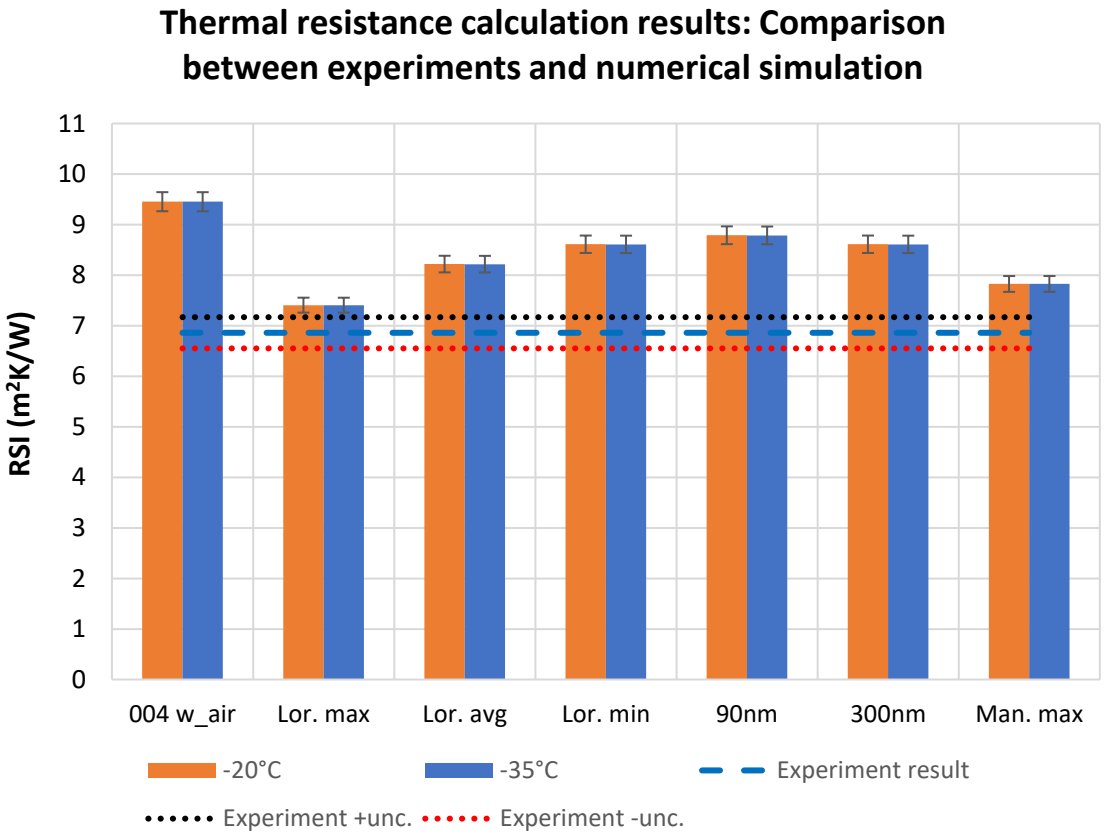


**Figure 36: Graphical comparison of RSI results for -20°C and -35°C exterior temperatures.**

**Table 29: Absolute percent difference between two-dimensional simulation RSI and GHB RSI.**

| | 004 w_air | Lor. max | Lor. average | Lor. min | 90nm | 300nm | Manufacturer max |
|---|---|---|---|---|---|---|---|
| **-20°C** | 38.0% | 8.1% | 20.0% | 25.7% | 28.3% | 25.7% | 17.0% |
| **-35°C** | 38.0% | 8.1% | 20.0% | 25.7% | 28.3% | 25.7% | 15.7% |

The least accurate results occur when using the manufacturer advertised centre of panel thermal conductivity (004 w_air), which resulted in an over prediction of the thermal resistance by 38% at both exterior temperatures. Similar to the trend found with the industry standard calculation methods, the use of effective thermal conductivity of the VIP result in increased accuracy.

The effective thermal conductivity which results in the thermal resistance closest to the experiment results is the Lorenzati max effective thermal conductivity, with a predicted RSI of 7.4 $m^2$ K/W for both -20°C and -35°C exterior temperatures. This corresponds to an absolute difference of 8.1% for both exterior temperatures. The next most accurate RSI value is derived from using the Manufacturer max VIP effective thermal conductivity., with a predicted RSI of 7.8 $m^2$K/W for both exterior temperatures. This corresponds to percent differences of 17.0% compared to the test results.

Although the Lorenzati max and Manufacturer max effective thermal conductivities resulted in the most accurate results, the assumptions made to determine these values should not be applied in future calculation methods. As discussed in the industry standard calculation results, the Lorenzati max effective thermal conductivity should result in an underestimation of the thermal resistance, as it is derived from the maximum air gap measured in the wall assembly. The manufacturer max value is supposed

to include edge heat transfer and aging effects, however the VIPs used in the investigation were new, and therefore should have very minimal aging effects associated with their performance.

Based on these results the recommended approach would be to use the Lorenzati average effective thermal conductivity. In this case the results indicate that using an effective thermal conductivity based on the average air joint width results in an overestimation of the thermal resistance by 20% for both exterior temperatures.

### 8.1.3 Temperature through depth of mineral fibre

The mineral fibre temperature was measured at four depth locations at the centre of the cavity. The four depths consisted of the exterior gypsum/mineral fibre interface (0 mm), 25 mm (1 in) from the sheathing board towards the exterior, 50 mm (2 in) from the sheathing board and 75 mm (3 in) from the sheathing board. The experiment results consist of an average at the four locations for each depth. Likewise, the 2D simulation results consist of an average temperature at each depth derived from the results in the centre of each stud cavity in the simulations. The comparison of the numerical simulation to experiment results are presented for the -20°C and -35°C exterior temperature conditions in Table 30. The results are graphically compared in Figure 38 and Figure 38 for the -20°C and -35°C exterior temperatures respectively. The values are compared also in Table 31 for absolute percent difference from the experimental result.

Table 30: Temperature profile through the depth of mineral fibre.

| | [mm] | GHB exp. result (±0.55) | 004 w_air | Lor. max | Lor. avg | Lor. min | 90nm | 300nm | Man. max |
|---|---|---|---|---|---|---|---|---|---|
| -20°C | 0 | 19.4 | 20.0 | 19.8 | 19.9 | 19.9 | 19.9 | 19.9 | 19.9 |
| | 25 | 16.1 | 17.4 | 16.7 | 17.0 | 17.2 | 17.3 | 17.2 | 17.0 |
| | 50 | 13.8 | 14.6 | 13.4 | 14.1 | 14.4 | 14.5 | 14.4 | 13.9 |
| | 75 | 9.4 | 11.9 | 10.2 | 11.1 | 11.6 | 11.8 | 11.6 | 10.9 |
| -35°C | 0 | 19.1 | 19.7 | 19.4 | 19.5 | 19.6 | 19.6 | 19.6 | 19.5 |
| | 25 | 14.7 | 16.5 | 15.1 | 15.7 | 15.9 | 16.0 | 15.9 | 15.5 |
| | 50 | 11.6 | 13.1 | 10.7 | 11.7 | 12.1 | 12.2 | 12.1 | 11.4 |
| | 75 | 5.7 | 9.7 | 6.3 | 7.7 | 8.3 | 8.5 | 8.3 | 7.3 |

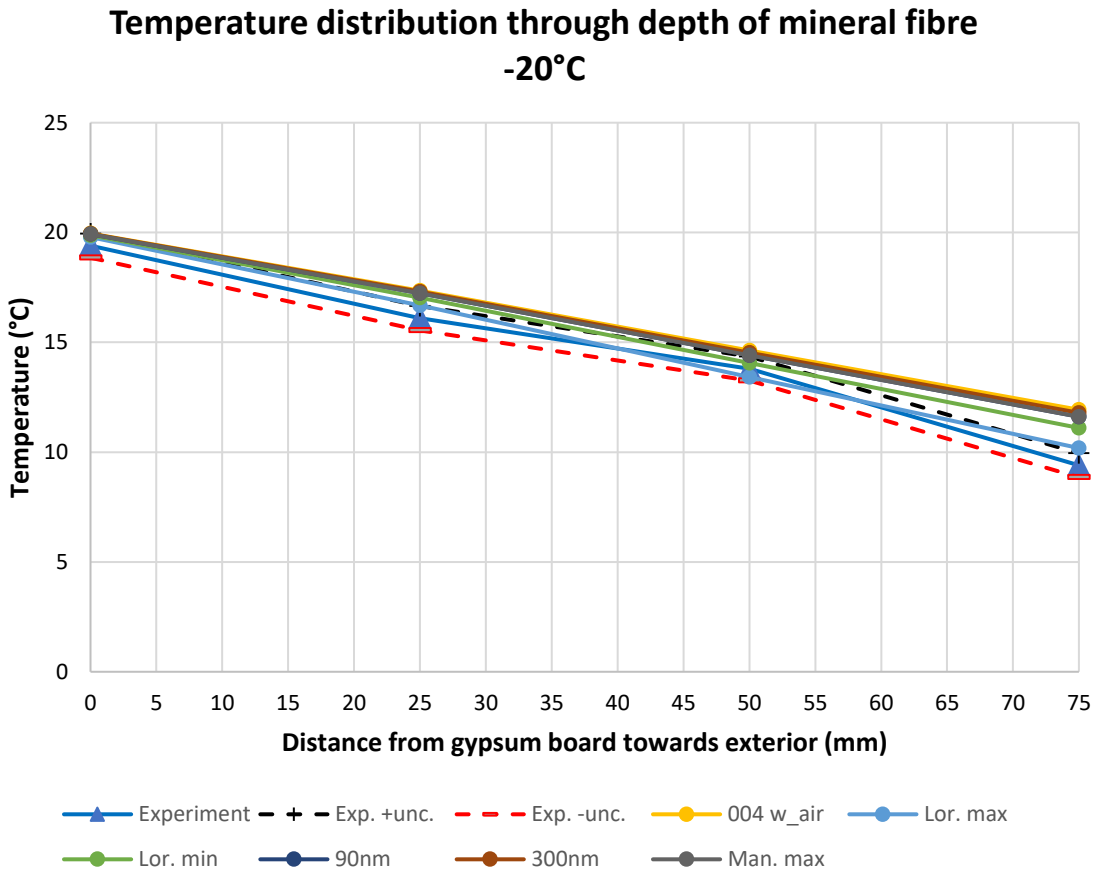


Figure 37: Comparison of the mineral fibre temperature as predicted by the numerical simulations to those measured for the same location in GHB experiments at -20°C exterior temperature.

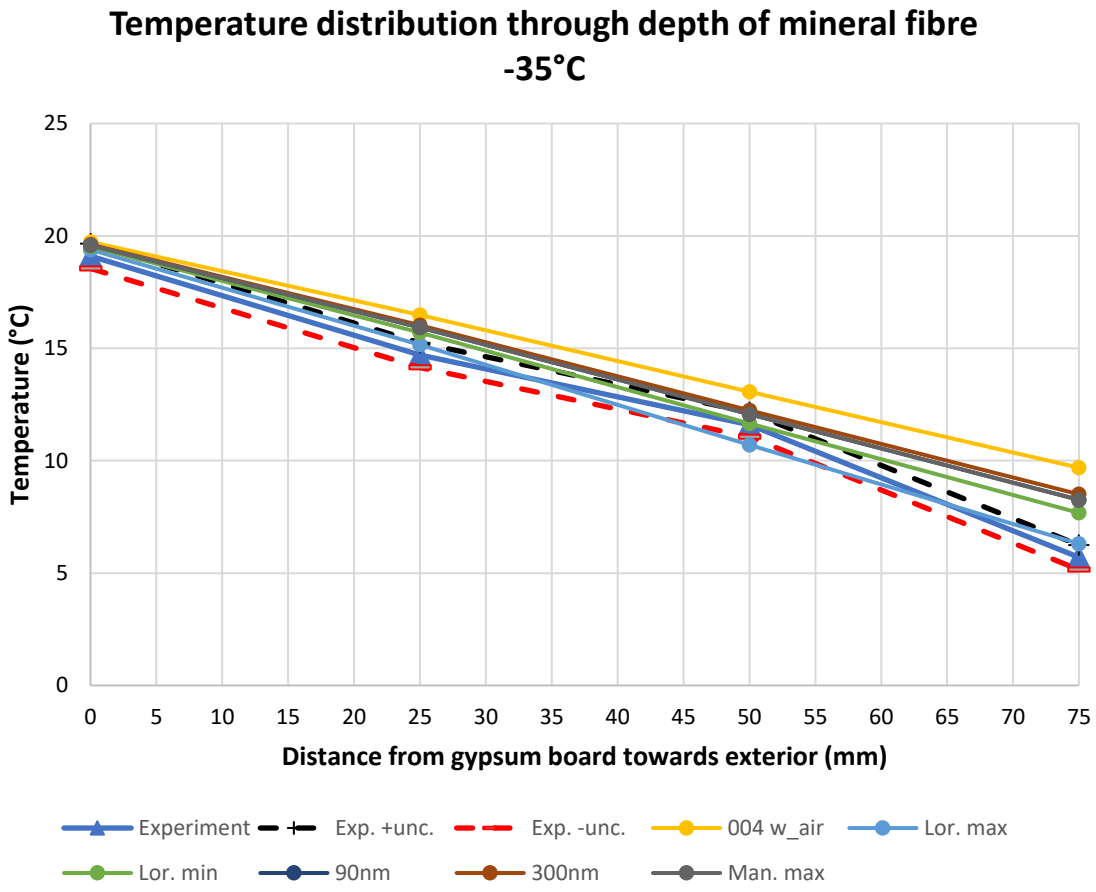


**Figure 38: Comparison of the mineral fibre temperature as predicted by the numerical simulations to those measured for the same location in GHB experiments at -35°C exterior temperature.**

**Table 31: Absolute percent difference between the experiment and numerical results.**

| | [mm] | 004 w_air | Lor. Max | Lor. Avg | Lor. Min | 90nm | 300nm | Man. max |
|---|---|---|---|---|---|---|---|---|
| -20°C | 0 | 2.9% | 2.0% | 2.5% | 2.7% | 2.8% | 2.7% | 2.4% |
| | 25 | 7.8% | 3.6% | 5.8% | 7.1% | 7.5% | 7.1% | 5.4% |
| | 50 | 6.0% | 2.8% | 1.8% | 4.4% | 5.3% | 4.4% | 0.9% |
| | 75 | 26.9% | 8.4% | 18.1% | 23.5% | 25.4% | 23.5% | 16.2% |
| | Avg. % diff. | **10.9%** | **4.2%** | **7.1%** | **9.4%** | **10.3%** | **9.4%** | **6.2%** |
| -35°C | 0 | 3.30% | 1.5% | 2.2% | 2.6% | 2.7% | 2.612% | 2.0% |
| | 25 | 12.10% | 3.1% | 6.8% | 8.3% | 9.0% | 8.3% | 5.6% |
| | 50 | 12.6% | 7.8% | 0.5% | 4.0% | 5.5% | 4.0% | 1.7% |
| | 75 | 70.0% | 10.6% | 34.7% | 44.9% | 49.2% | 44.9% | 28.4% |
| | Avg. % diff. | **24.5%** | **5.7%** | **11.1%** | **14.9%** | **16.6%** | **14.9%** | **9.5%** |

Comparing the overall results shows that the accuracy of the simulations decreases the further the location of interest is from the sheathing board. The probable cause is due to two factors. The first factor is that the mineral fibre thermal conductivity that was selected is from the manufacturer quoted value, so could be slightly different than that which was tested. The second reason is that the nominal instrumentation locations may be slightly different than those selected. Referring to Figure 15, the thermocouples in the mineral fibre were held on a tree, and were placed on the tree within approx. ±5 mm of the designated depth. This difference in depth could have caused a slight difference in the experiment results from those determined in the simulations. Even considering these potential differences between the experimental set up and the simulations, the simulation results generally agree with the experiment values.

The results indicate the same trends that were noticed previously with the thermal resistance results. The simulation that uses the Lorenzati max VIP effective thermal

conductivity results in the closest values to the experiment, followed by the Manufacturer max and the Lorenzati average VIP effective thermal conductivity simulations. The least accurate result is once again due to the manufacturer advertised centre of panel thermal VIP thermal conductivity.

### 8.1.4 Steel stud thermal bridge: Comparison of numerical simulation results to experiment results

The effect of the steel stud thermal bridge on the interior sheathing board surface temperature is compared between the measured values from GHB experiments to the numerical simulations for both exterior temperatures in Table 32, Figure 39 and Figure 40.

**Table 32: Comparison between simulations and experiment results for interior surface temperature in proximity to steel stud.**

| | [mm] | Exp. (±0.55°C) | 004 w_air | Lor. max | Lor. avg. | Lor. min | 90nm | 300nm | Man. max |
|---|---|---|---|---|---|---|---|---|---|
| -20°C | 0 | 18.7 | 19.8 | 19.6 | 19.7 | 19.8 | 19.8 | 19.6 | 19.6 |
| | 25 | 18.9 | 20.0 | 19.8 | 19.9 | 20.0 | 20.0 | 19.8 | 19.9 |
| | 50 | 19.3 | 20.3 | 20.2 | 20.2 | 20.3 | 20.3 | 20.2 | 20.2 |
| | 200 | 19.7 | 20.4 | 20.3 | 20.4 | 20.4 | 20.4 | 20.3 | 20.3 |
| -35°C | 0 | 18.3 | 19.4 | 19.0 | 19.2 | 19.3 | 19.3 | 19.3 | 19.1 |
| | 25 | 18.5 | 19.7 | 19.4 | 19.5 | 19.6 | 19.6 | 19.6 | 19.4 |
| | 50 | 19.1 | 20.1 | 19.9 | 20.0 | 20.0 | 20.0 | 20.0 | 19.9 |
| | 200 | 19.5 | 20.3 | 20.1 | 20.2 | 20.2 | 20.2 | 20.2 | 20.1 |

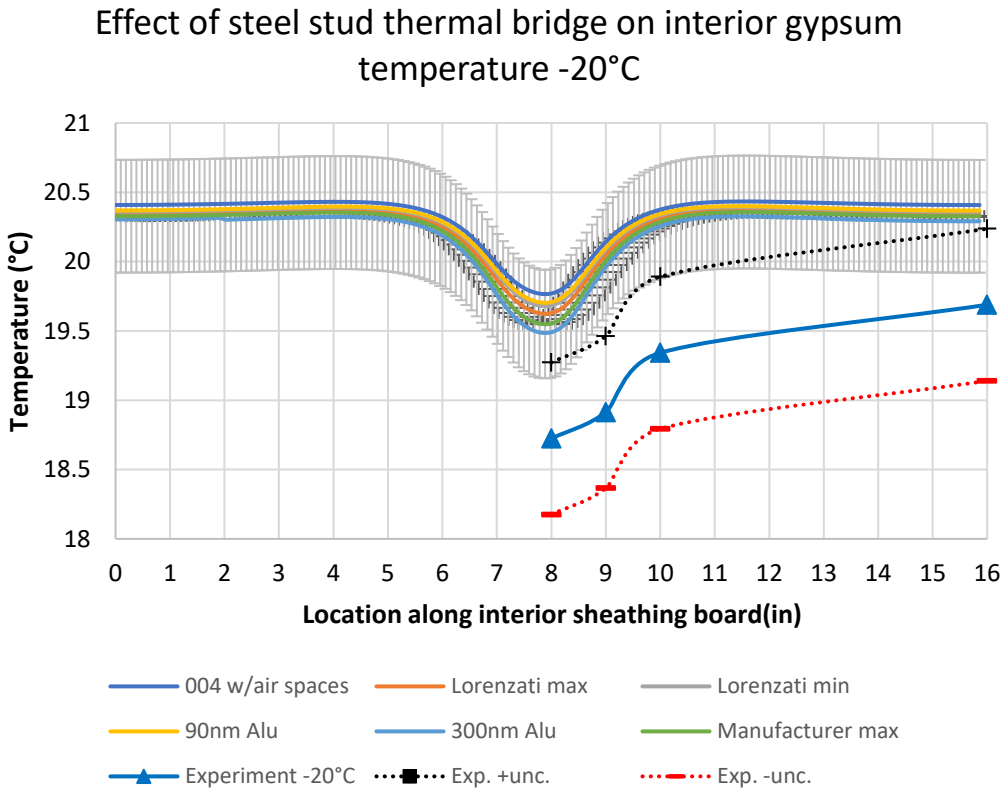


**Figure 39: -20°C steel stud effect on interior sheathing board temperature.**

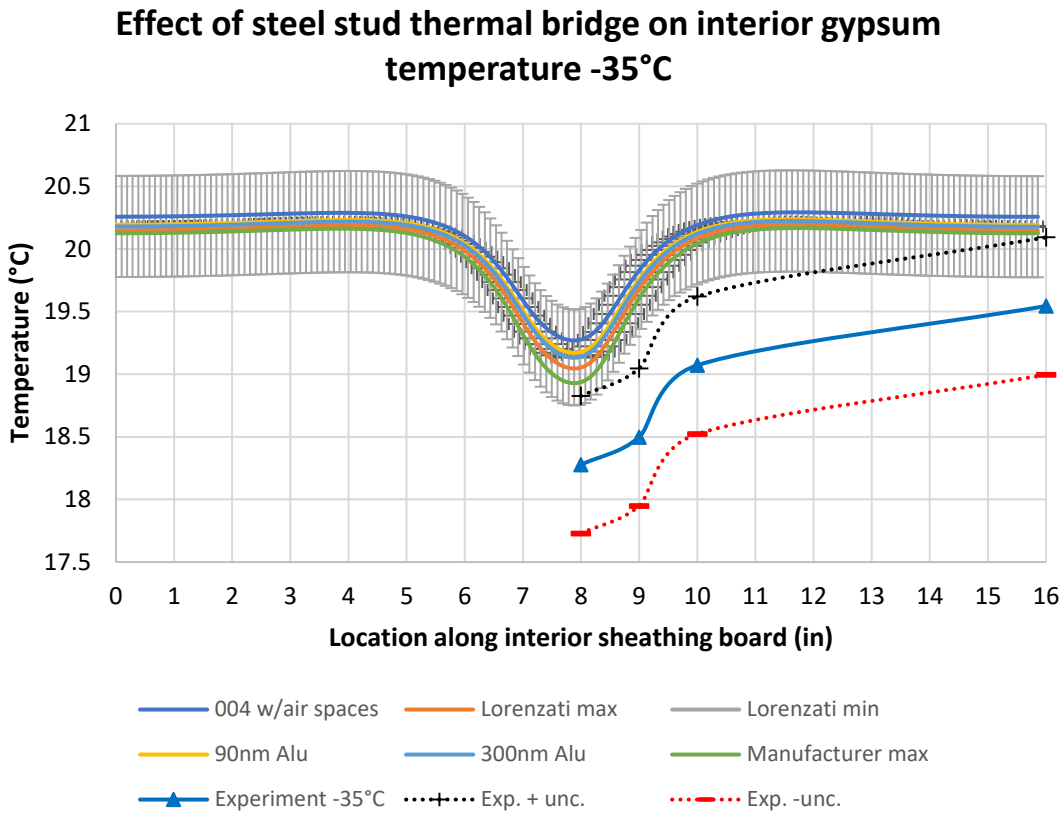


**Figure 40: -35°C steel stud effect on interior sheathing board temperature.**

Overall the results indicate that the 2D numerical simulations over predict the temperature of the interior sheathing board in proximity to the steel stud and at the centre of the stud cavity. The over estimation of the interior surface temperature due to the steel stud is likely caused by the thermal bridges that are not accounted for in the two-dimensional simulations, specifically at the horizontal air spaces and fiberglass clips (Figure 41). The thermal bridges at these locations would cause the temperature of steel stud to decrease and transfer more heat from the interior.

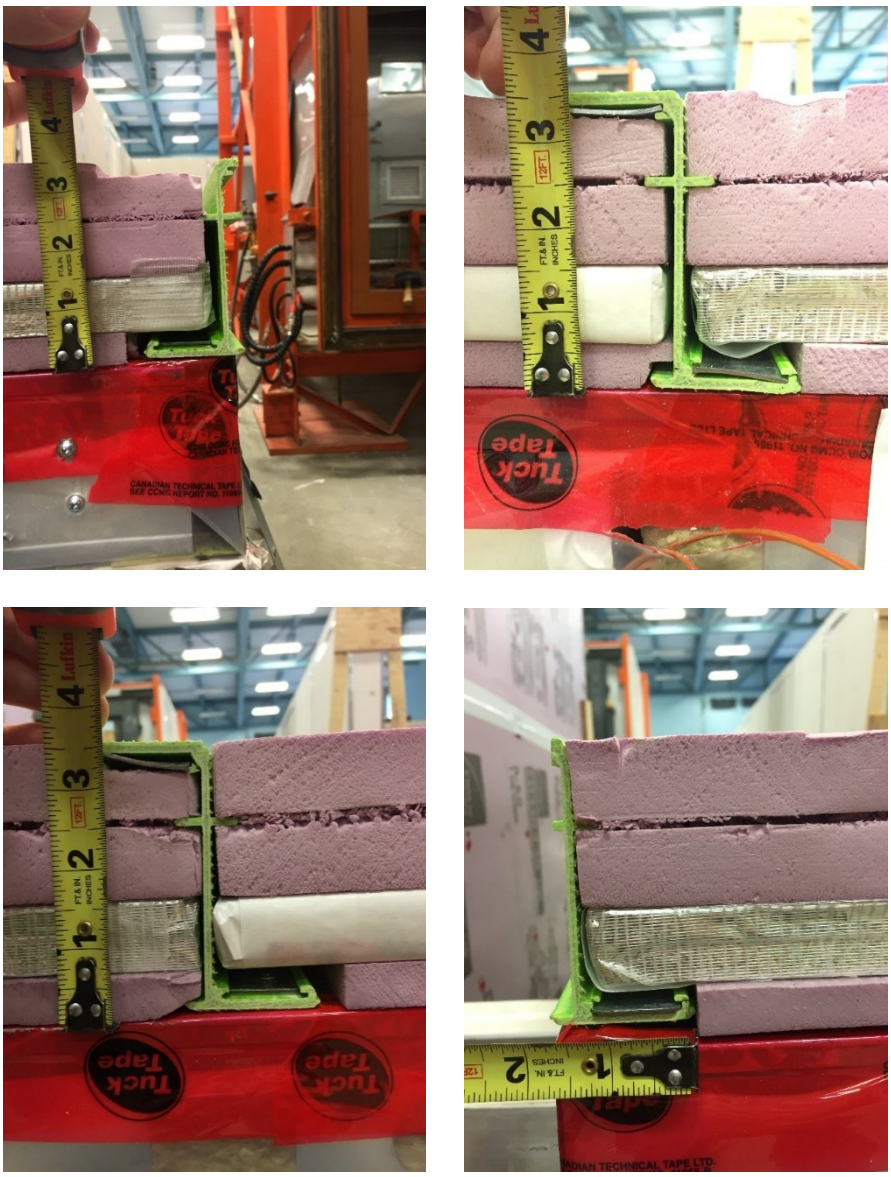


**Figure 41: Horizontal thermal bridge air gaps in wall assembly. The top left photo depicts the air gap present at the top of the wall assembly, the top right and bottom left represent the two transition air gaps between rows of VIP sandwich panels and the bottom right photo represents the air gap present at the bottom of the wall assembly.**

To investigate the potential for air gaps to decrease the stud temperature, the 004 w_air VIP effective thermal conductivity simulation was analyzed to compare the interior surface temperature at the centre stud to the other studs in the assembly. This comparison enabled determining the interior sheathing board temperature due to a stud in the presence

of an air gap and a stud that was not exposed to the air gap. The comparison is shown in Figure 42 (-20°C) and Figure 43 (-35°C).

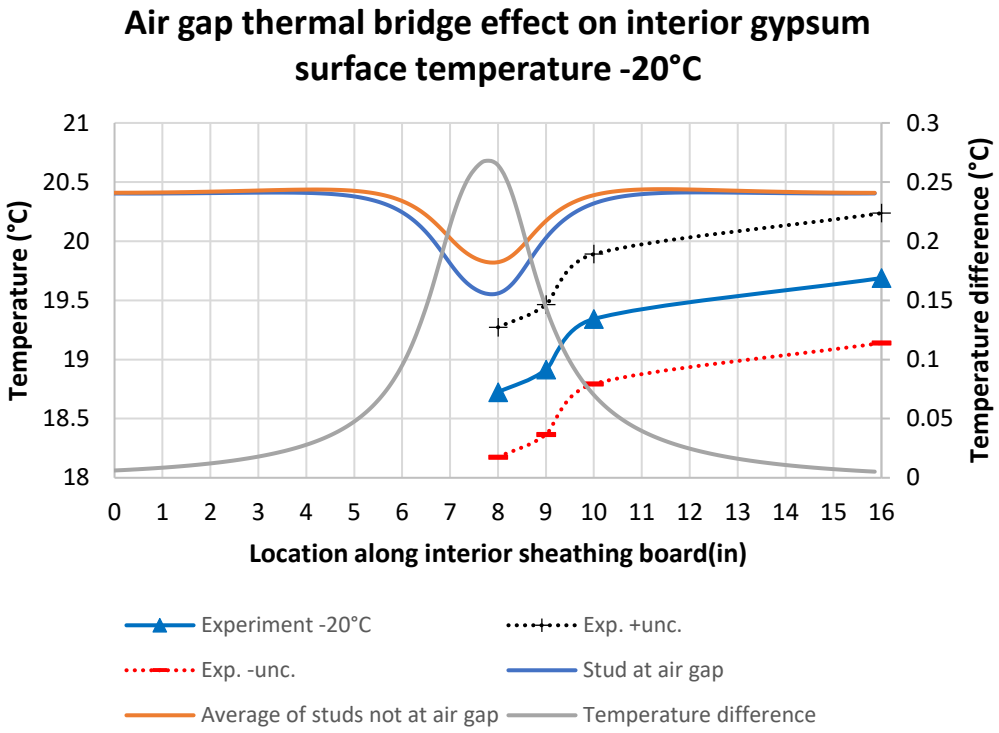


**Figure 42: Comparison of the effect of air gap thermal bridge on interior surface temperature at steel stud locations with and without the air gap, exterior temperature of -20°C.**

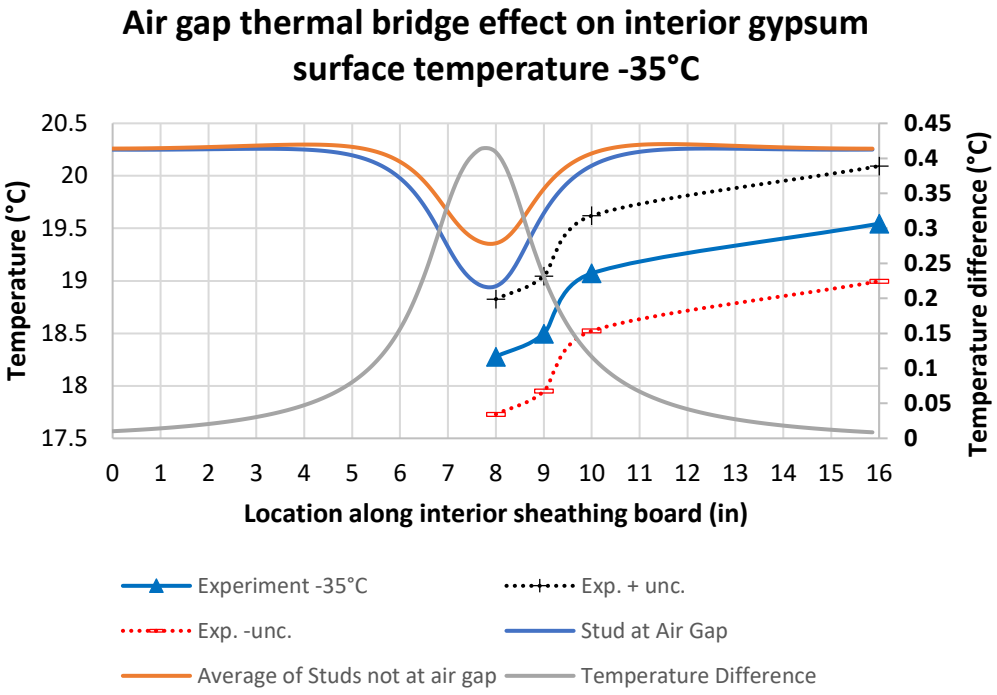


**Figure 43: Comparison of the effect of air gap thermal bridge on interior surface temperature at steel stud locations with and without the air gap, exterior temperature of -35°C.**

The results in Figure 42 and Figure 43 demonstrate the difference in the interior surface temperature that can occur due to the proximity of a steel stud with and without the presence of an air gap thermal bridge. Comparing the temperature drop to the experimental results still indicates that the simulation overestimates the interior surface temperature. The result is an example however that not accounting for the horizontal thermal bridges does decrease the accuracy of the 2D simulation.

### 8.1.5 Two-dimensional simulation conclusions

The results of the 2D numerical simulations indicate the additional information that can be obtained over the industry standard calculation methods. However, the results indicate that the 2D simulations are less accurate for predicting the thermal resistance of a

wall assembly than the modified zone calculation method. Using the Lorenzati average results for comparison, the overestimation of the thermal resistance for the modified zone method was approximately 15%, whereas the 2D simulation using the same effective thermal conductivity indicates an overestimation of 20%. The reason for the decreased accuracy in the 2D simulations is most likely due to the underprediction of the effect of the steel stud on the interior temperature. The modified zone method makes use of a zone factor, which accounts for the area over which the steel stud effects the interior temperature. The calculation of the zone factor only accounts for the insulation level of the first 25 mm of exterior sheathing materials, which in this case is 12.7 mm XPS and 12.7 mm VIP. Not accounting for the full insulation level of the exterior sheathing is why the modified zone method attributes higher heat transfer through the stud than the 2D simulations. For these results the modified zone method is more accurate than the 2D simulations, however more highly insulated wall systems would need to be tested to validate these findings.

The advantage of 2D simulations over industry standard calculation methods is that the simulations can provide more information regarding the wall assembly performance than just the thermal resistance of the assembly. In this case the interior surface temperature and temperature through the depth of the mineral fibre were investigated. The results for the temperature through the depth of the mineral fibre compared favorably to the GHB test results. The interior sheathing board temperature however indicated that the 2D simulations overestimated the interior surface temperature by approximately 1.5°C. The reasons for the

over estimation are likely due to the thermal bridges that are not accounted for in the plan view geometry.

An investigation of the potential effect of air gaps not accounted for in the plan view geometry demonstrated that accounting for air gaps would decrease the sheathing board temperature. The effect of the thermal bridges not accounted for in the 2D simulations were investigated in the 3D simulations.

Overall the results indicate that accounting for the effective thermal conductivity of VIPs increases the calculation accuracy over simply using the centre of panel thermal conductivity. The 2D simulations also demonstrate that it is important to account for all thermal bridges in an assembly, as the results still overestimate the thermal resistance, and interior sheathing board temperature around the steel studs, as compared to the GHB test results. Likely, the accuracy of the 2D simulations could be significantly improved if the thermal transmittance method could be used to determine the effective thermal transmittance of the XPS-VIP-XPS layer including all thermal bridges.

## 8.2 Three-dimensional numerical simulation

The overestimation of thermal resistance by the industry standard calculation method and 2D simulations demonstrated in this work indicates that for highly insulated wall assemblies, attention needs to be given to all thermal bridge effects to attain an accurate result. These results are consistent with findings in the literature to determine the effective thermal conductivity values for assemblies containing thermal bridges (Morris and Hershfield Ltd., 2011). To determine the effect of all thermal bridges in the wall

assembly a three-dimensional simulation including the fiberglass clips and the horizontal air spaces was conducted.

As discussed previously, difficulties in meshing the geometry caused several adjustments to be required on the wall assembly geometry compared with the as built wall assembly. The adjustments were that only a subsection of the wall assembly was simulated with thermal symmetry boundary conditions, and the steel stud gauge was increased.

To relate the adjusted 3D simulation results with the results that would be expected if the as built wall was simulated correction factors were developed from 2D simulations. The correction factors were determined through 2D modelling for the thermal resistance, interior surface temperature in proximity to the steel stud and temperature through the depth of the mineral fibre. The corrections were applied to the 3D simulation results and the adjusted values were compared to the GHB test results. This section describes the 2D correction factors that were developed.

### 8.2.1 Investigation of modelling sub-section with thermal symmetry assumption and larger gauge steel studs

The method to determine the correction factors consisted of simulating the sub-section of the 2D plan view geometry with increased gauge steels studs, and comparing the results to those of the average results of the same full plan view 2D assembly. The correction factor was then determined as the factor which if multiplied by the sub-section results would result in the same as the full assembly result.

The sub-section consisted of a centre stud with a half stud cavity (200 mm or 8 in) in each direction from the centre of the steel stud and thermal symmetry boundary conditions on each lateral edge. The steel stud gauge in this geometry was increased by a

factor of 10; all other parameters of the steel stud were the same as the original dimensions. The 004 w_air VIP thermal conductivity with the air gap geometry (Figure 26 B) was used for this assessment, as it is used in the 3D simulation and results in the largest correction factor due to the difference between the centre of panel thermal conductivity and the air gap between the VIPs.

The thermal resistance, interior surface temperature, and temperature through the depth of the mineral fiber at the centre of the stud cavity results for the sub-assembly were compared with the results derived from the full 2D plan view assembly. Correction factors were developed from the 2D comparison to adjust the values of the 3D sub-assembly to predict the performance expected if a full 3D assembly was simulated. A schematic depicting the sub-assembly compared with the centre stud of the full 2D geometry is shown in Figure 44. The boundary conditions are also indicated on the sub-assembly geometry. The boundary conditions for this simulation were the same as those used for all other two-dimensional simulations, given in Table 24. The Extreme fine x10 mesh was used for the sub-assembly geometry. The COMSOL settings for the models to determine the correction factors are given in Appendix K .

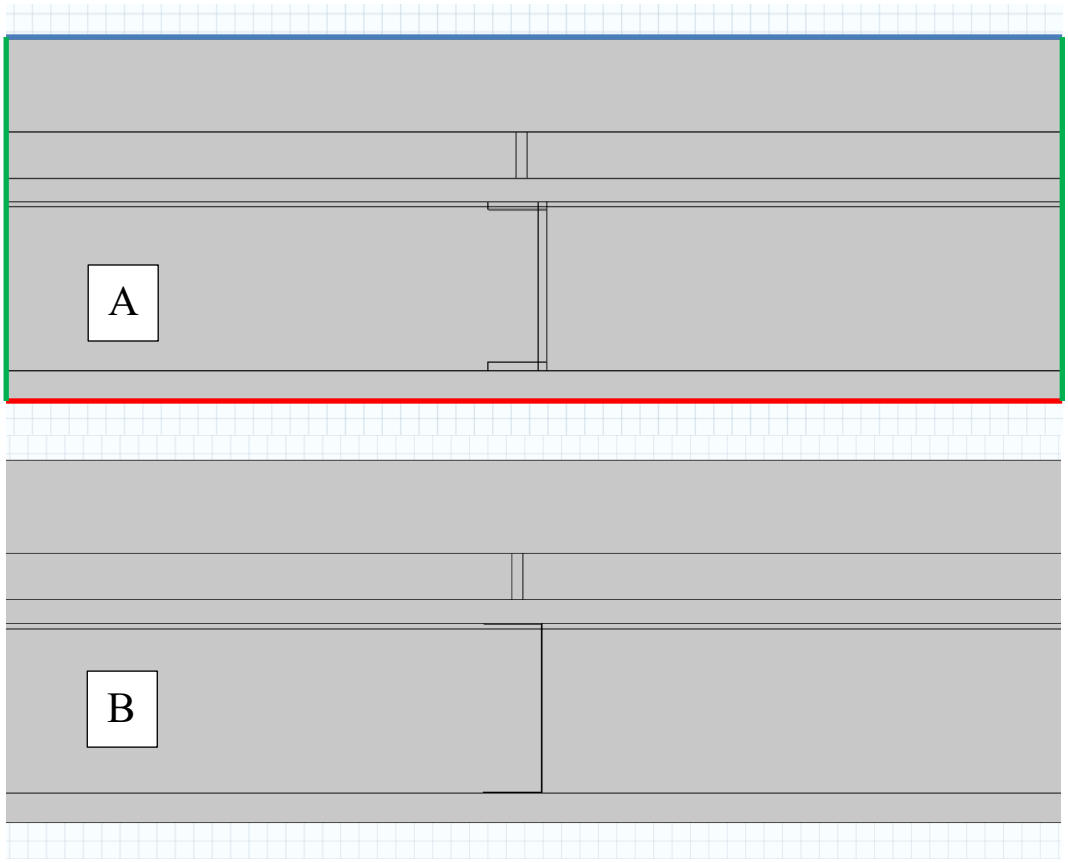


**Figure 44: Sub section (x10 gauge) geometry (A) compared with the centre stud of full 2D geometry (B). BC's: blue – exterior heat flux condition, red – interior heat flux condition, green – thermal symmetry condition.**

#### 8.2.1.1 Thermal resistance correction factors

The thermal resistance correction factor is based on the change of the average interior surface heat flux density, which is used in the thermal resistance calculation. The results for the interior heat flux density for the full 2D plan view geometry (2D full) and the sub-assembly (N10 symmetry) are given in Table 33. The corrected 3D result is obtained by multiplying the average interior surface heat flux density by the correction factor, and then calculating the thermal resistance with the corrected value.

**Table 33: Results comparison and correction factor for thermal resistance with centre stud and increased stud gauge assumptions**

| Average surface heat flux density [W/m$^2$] | -20°C | -35°C |
|---|---|---|
| 2D full | 4.20 | 5.72 |
| N10 symmetry | 4.78 | 6.49 |
| Correction factor | 0.88 | 0.88 |

#### 8.2.1.2 Interior surface temperature correction factors

The correction factors for the interior surface temperature are based directly on the difference in temperature between the sub-assembly results and the average of the full 2D geometry results. The results of the temperature comparison on the interior surface are given in Figure 45 and Figure 46 for the -20°C and -35°C exterior temperatures respectively.

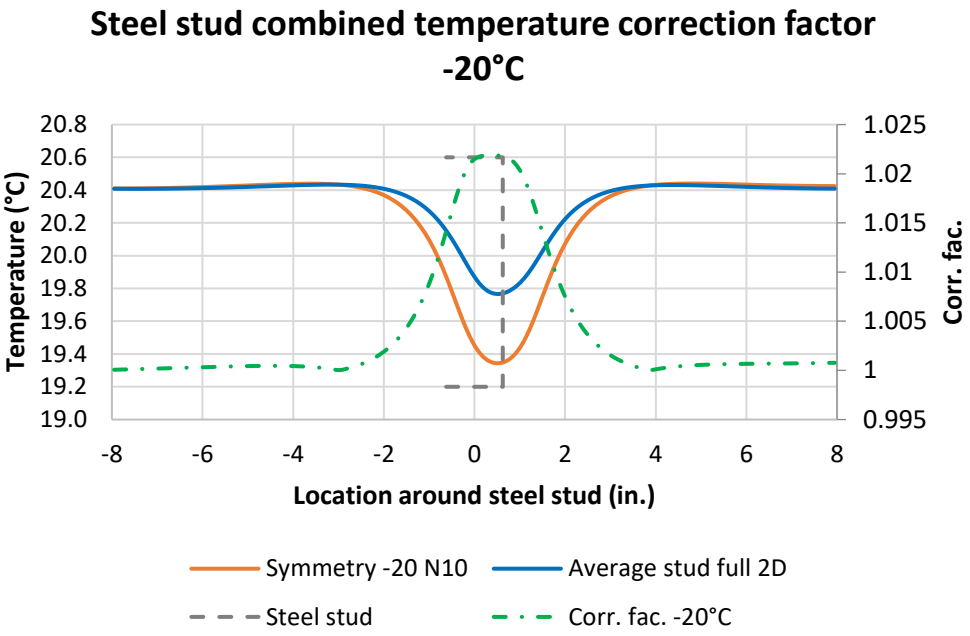


**Figure 45: Results comparison and correction factor for interior surface temperature in proximity to steel stud, -20°C.**

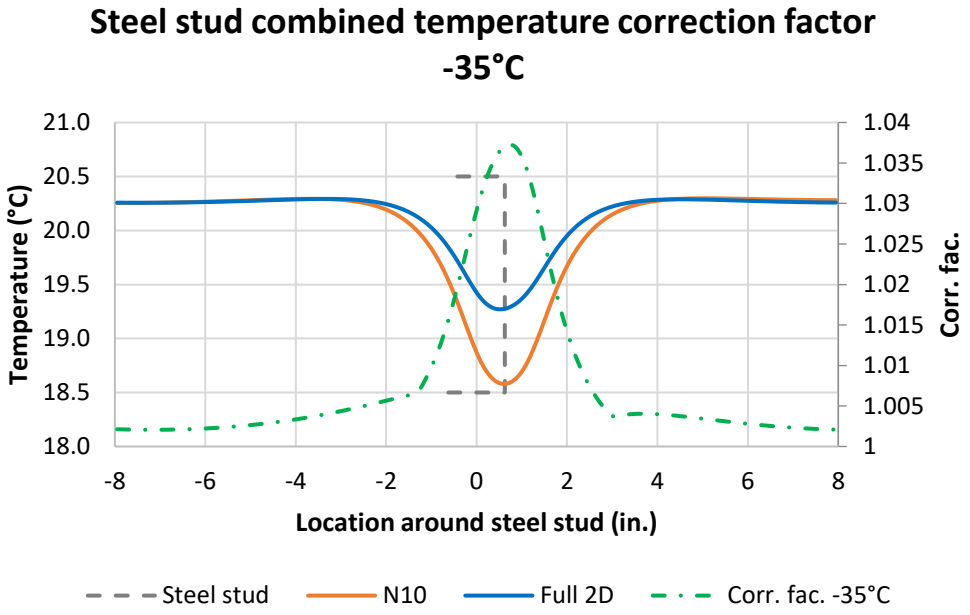


**Figure 46: Results comparison and correction factor for interior surface temperature in proximity to steel stud, -35°C.**

Comparing the full 2D geometry average results to the N10 centre stud symmetry results for both exterior temperatures shows that the centre stud combined with the increased stud gauge causes a decreased temperature to occur on the interior surface at the steel stud location. The decreased temperature zone occurs from the centre stud for approximately three inches to each side. After three inches to each side the results converge back to very similar values by the centre of the cavity to each side.

The correction factor for the steel stud temperature difference was applied to the 3D results by creating a curve fit dependent on the location in proximity to the steel stud. The curve fit was separated into a piecewise continuous curve, given in Appendix K .

#### 8.2.1.3 Temperature through the depth of the mineral fibre correction factors

The correction factors for the temperature through the depth of the mineral fibre were also based directly on the temperature difference between the thermal symmetry with 10x gauge studs and the 2D full plan view simulation results. The results of the comparison on the temperature through the depth of the mineral fibre are given in Figure 47 and Figure 48 for the -20°C and -35°C temperatures respectively.

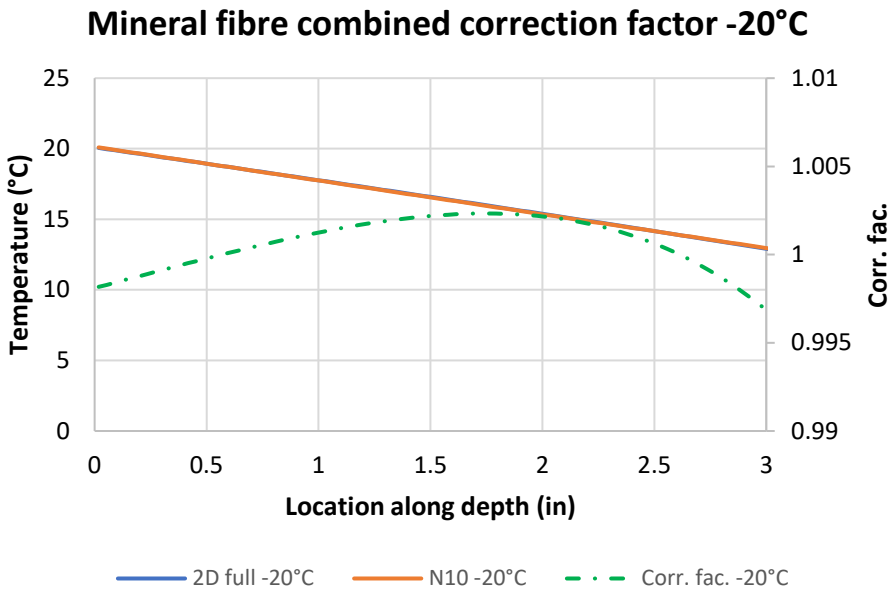


**Figure 47: Results comparison and correction factor for temperature through the depth of the mineral fibre -20°C exterior temperature.**

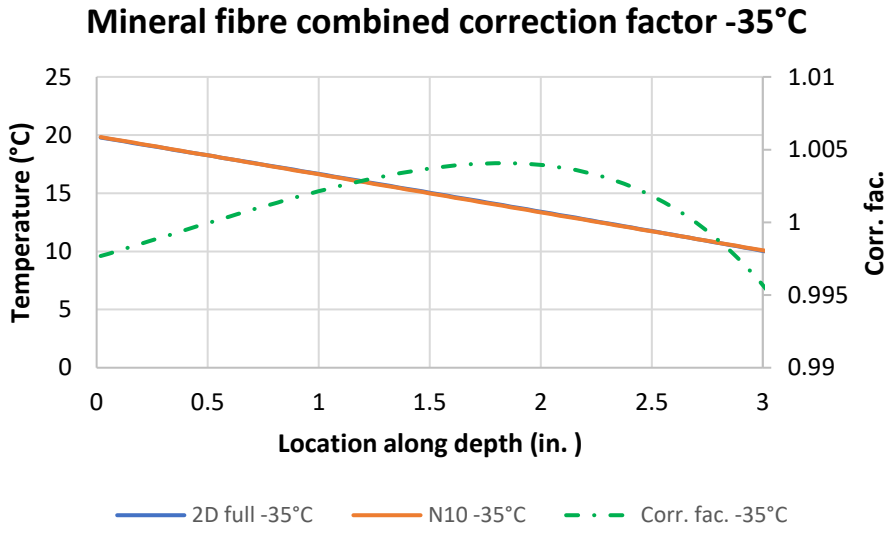


**Figure 48: Results comparison and correction factor for temperature through the depth of the mineral fibre -20°C exterior temperature.**

The mineral fibre results indicate that there is very negligible effect on the temperature profile at the centre of the stud cavity due to the centre stud sub-assembly, or

the increased stud gauge. The correction factors were applied to the 3D results in the same manner as the other correction factors. The curve fit for the mineral fibre correction factor is given in Appendix K .

## 8.3 Three-dimensional simulations

The three-dimensional simulations were conducted for exterior temperatures of - 20°C and -35°C. The results were compared to the experiment results for the wall assembly at each temperature for: thermal resistance, interior surface temperature in proximity to the steel stud thermal bridge and temperature through the depth of the mineral fibre. The uncertainty in the 3D results is also described.

### 8.3.1 Uncertainty – Three-dimensional simulations

The uncertainty in the 3D simulation results considers uncertainty due to the material properties, discretization, convergence and rounding of the numerical solution and the correction factors.

The material properties used in the 3D simulations are a subset of the material properties used previously, so the uncertainty is assumed to be ±2%.

The correction factors were developed from the 2D simulations described previously. The correlations reproduce the results from the 2D modelling better than 0.1% in all cases, and therefore are not assumed to add any significant uncertainty to the results. The correction factors are also not estimated to increase the uncertainty of the results, beyond the material properties which have been accounted for.

The mesh convergence of the 3D numerical simulations results in a slight difference between the heat flux in to and out of the assembly due to the mesh being limited in the number of elements. This results in an uncertainty of approximately 0.73% and 0.98% for

the -20°C and -35°C exterior temperatures respectively. The convergence of the simulation was investigated by increasing the convergence by a factor of 10, and no appreciable difference in the results was noticed.

The combination of material property and numerical solution uncertainties are estimated to give a total uncertainty of ±3% for the 3D simulations.

### 8.3.2 Corrected three-dimensional thermal resistance comparison

The parameters used in the thermal resistance calculations and the corresponding calculated thermal resistance for each exterior temperature are shown in Table 34 and Figure 49.

**Table 34: Corrected thermal resistance from three-dimensional simulations.**

| | Interior heat flux $\frac{W}{m^2}$ | Exterior heat flux $\frac{W}{m^2}$ | RSI (R-value) $\frac{W}{m^2K}\left(\frac{hr*ft^2*°F}{BTU}\right)$ | Experiment RSI (R-value) $\frac{W}{m^2K}\left(\frac{hr*ft^2*°F}{BTU}\right)$ | % diff. |
|---|---|---|---|---|---|
| **-20°C** | 5.25 | 5.17 | 7.80 (44.26) | 6.85 (37.93) | 13.9% |
| **-35°C** | 7.15 | 7.01 | 7.83 (44.33) | 6.85 (38.38) | 14.0% |

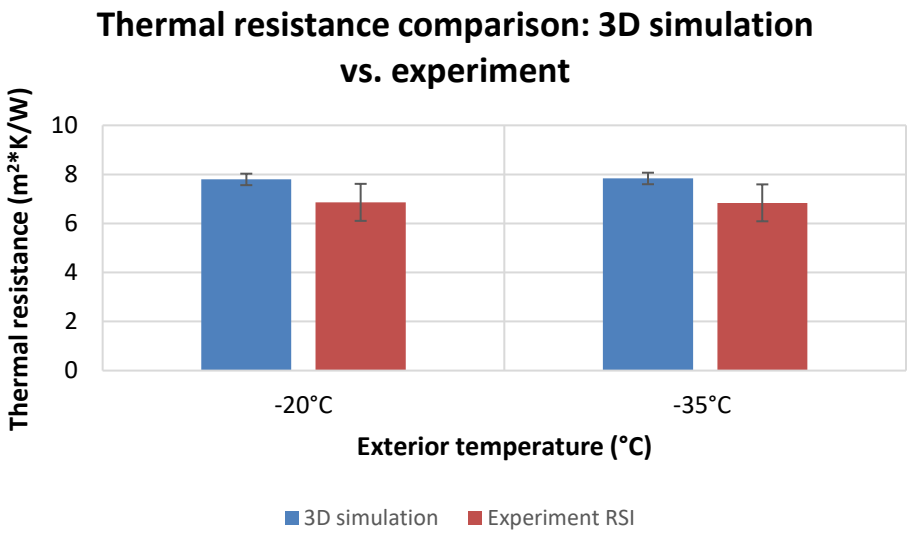


**Figure 49: Thermal resistance comparison, three-dimensional simulation versus experiment**

The results from Table 34 and Figure 49 indicate that the 3D simulations overestimate the thermal resistance by approximately 14% for both exterior temperatures. Comparing these results with the modified zone standard calculation method and 2D simulation results shows that the 3D simulation accuracy is equal to the modified zone method, and more accurate than the 2D simulations. Likely this is due to the 3D simulation accounting for the horizontal thermal bridges that occur due to the fiberglass clips and horizontal air spaces. An isotherm diagram from the COMSOL results is presented in Figure 50, which depicts the lateral view of the 3D simulation at the locations of the horizontal thermal bridges for both exterior temperatures.

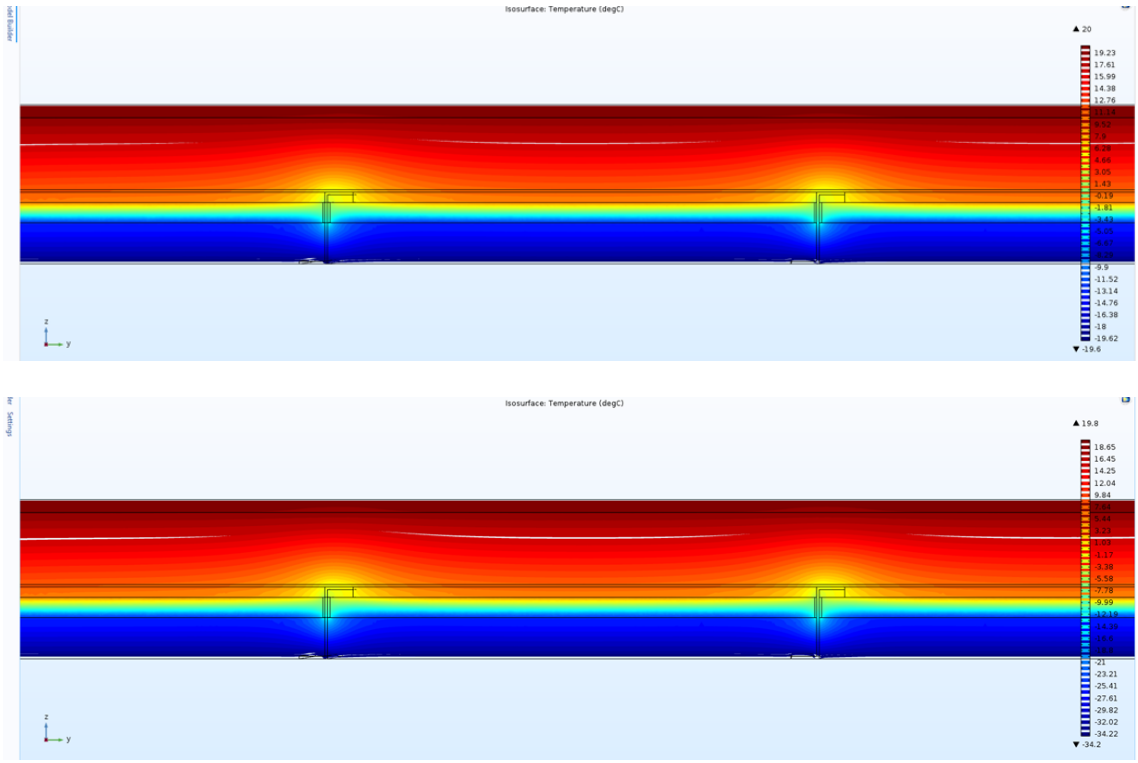


**Figure 50: Surface temperature plot from COMSOL Multiphysics® results for -20°C and -35°C exterior temperatures due to horizontal thermal bridges.**

The most likely reason that the 3D simulation still overestimates the thermal resistance of the wall assembly as compared with the experiments is due to the use of the idealized 004 w_air VIP thermal conductivity. Most likely this value is slightly higher, however without testing it is difficult to assign a value different than this for the 3D simulations.

#### 8.3.2.1 Corrected surface temperature due to steel stud thermal bridge

Results for the interior surface temperature around the steel stud for each exterior temperature are compared with the results from the experiment in Figure 51 (-20°C) and Figure 52 (-35°C).

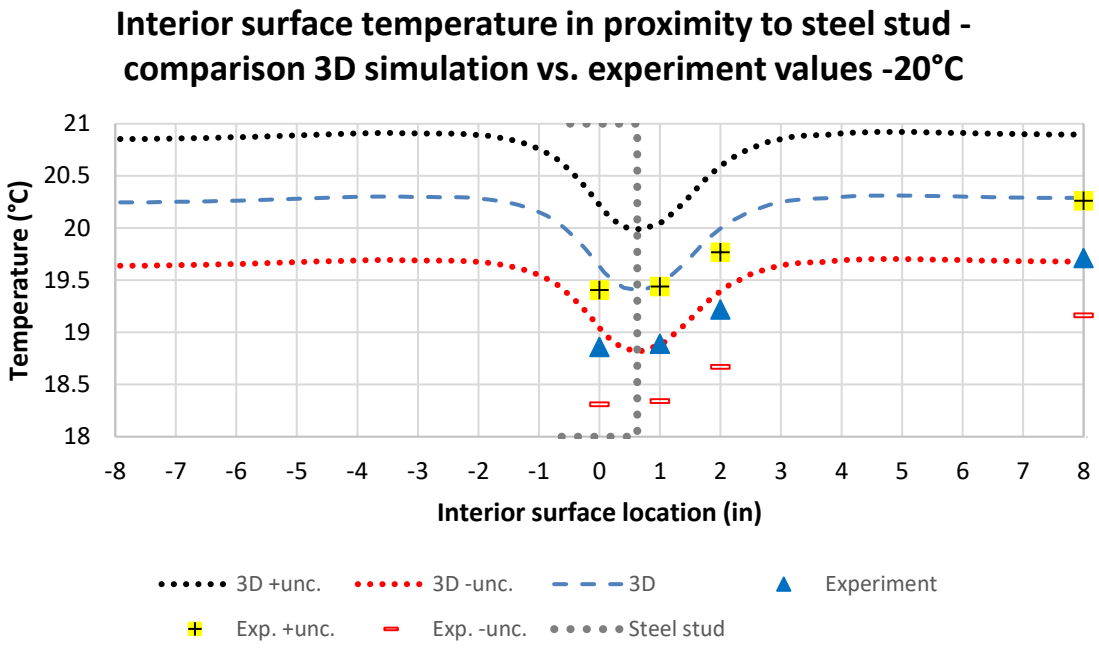


**Figure 51: Comparison between experiment and three-dimensional simulation for the interior surface temperature around the centre stud for the -20°C exterior temperature.**

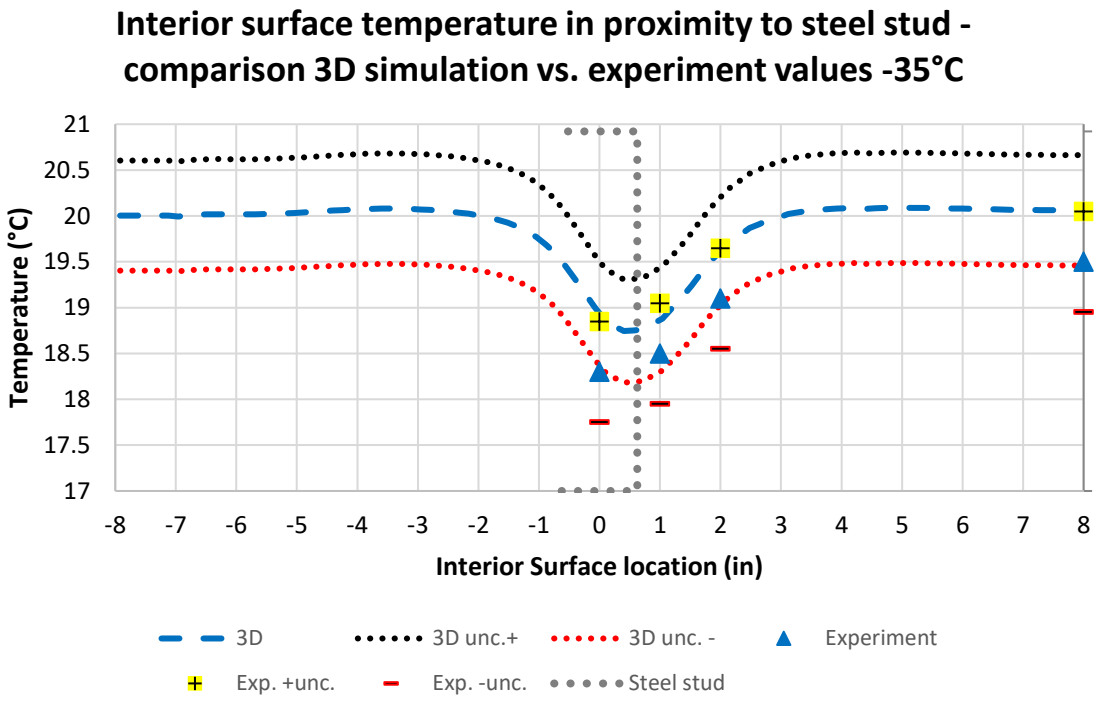


**Figure 52: Comparison between experiment and three-dimensional simulation for the interior surface temperature around the centre stud for the -35°C exterior temperature.**

Overall, the 3D modelling results in a much closer approximation of the experimental data than any of the two-dimensional model conditions. The results indicate that the three-dimensional model still underestimates the effect of the steel stud thermal bridge on the interior temperature. This underestimation, as well as the underestimation at the centre of the cavity (at -8 in and 8 in), indicates that likely the thermal conductivity of the VIP is too high in the simulations.

The -35°C exterior temperature simulation shows slightly better agreement with the experimental data than the -20°C results, with the uncertainty bands overlapping for both results. The maximum overestimation by the -35°C results is 0.6°C and the maximum overestimation of the surface temperature in the -20°C results is 0.8°C.

#### 8.3.2.2 Corrected temperature profile through depth of mineral fibre – 3D

The corrected temperature through the depth of the mineral fibre for the three-dimensional modelling is compared to the results measured during the experiment for both exterior temperatures in Figure 53 (-20°C) and Figure 54 (-35°C).

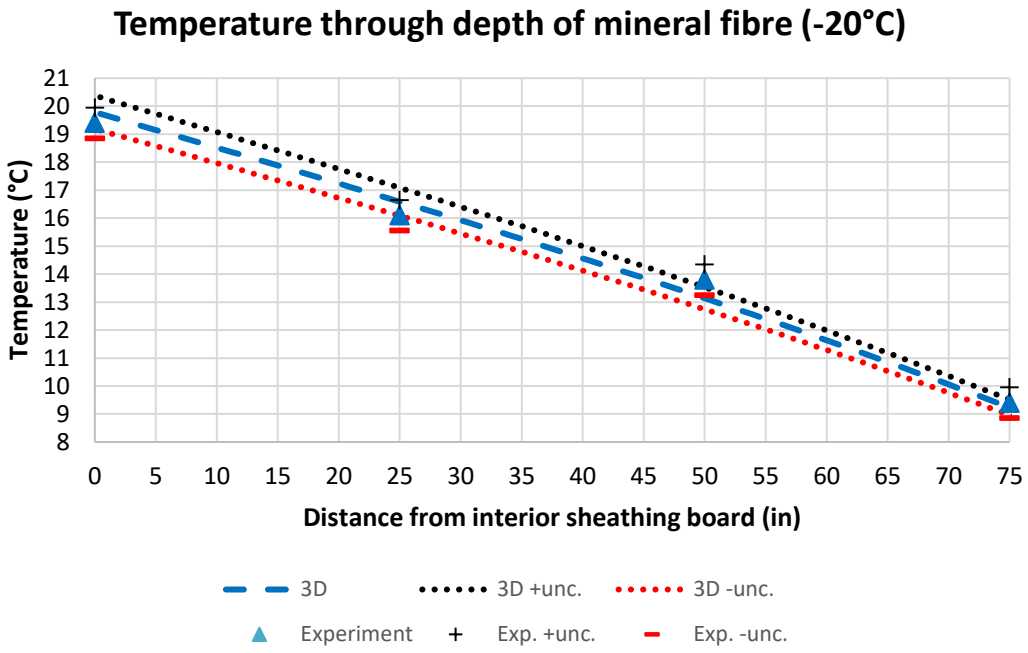


**Figure 53: Temperature profile through the depth for the mineral fibre, three-dimensional simulation at -20°C.**

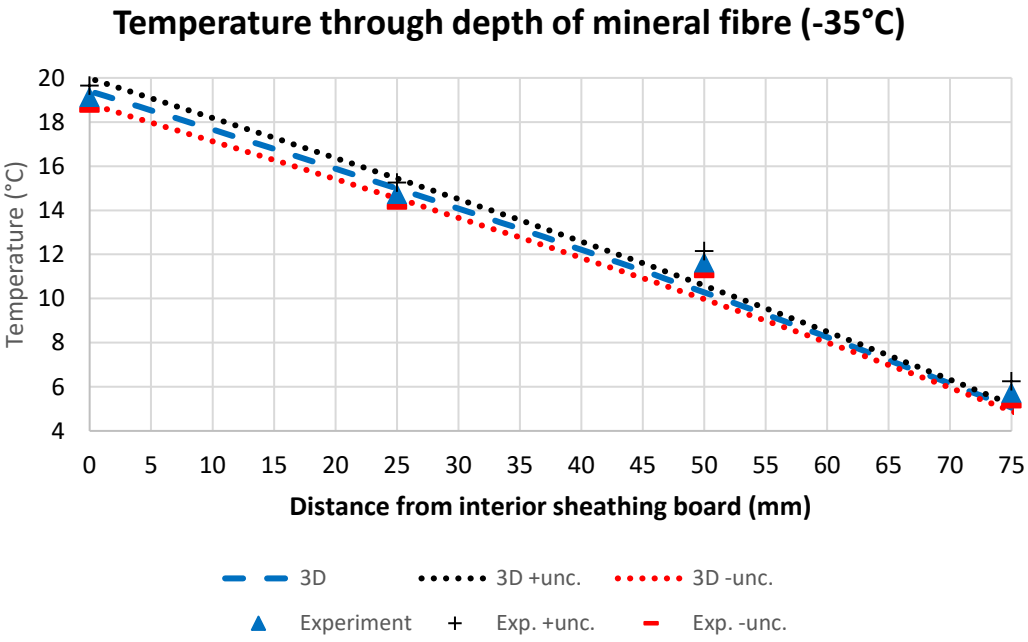


**Figure 54: Temperature profile through the depth for the mineral fibre, three-dimensional simulation at -35°C.**

The results for the temperature through the depth of the mineral fibre show reasonable agreement with the experimental results for both external temperatures, especially the 0 mm, 25 mm and 75 mm depth locations. The 50 mm location shows less agreement in both external temperature cases. The results indicate that the assumption of thermal symmetry at the centre of cavity is valid.

The underestimation at the 50 mm point could be caused by two factors: the thermal conductivity of the mineral fibre is slightly different than that which was used from advertised values, or the thermocouple tip measurement location may not be at the exact location plotted. Based on the simulation accuracy at 0 mm, 25 mm and 75 mm it is unlikely that the variance at 50 mm is caused by an error in the thermal conductivity of the mineral fibre.

Most likely the reason for the discrepancy is due to experimental error, specifically estimation of the sensor location. The thermocouple could be ±5 mm, due to install error, and if the location was more towards the -5 mm location in the wall assembly, the results would correlate very well with the simulation results for both cases.

#### 8.3.2.3 Three-dimensional simulation conclusions

The 3D simulations resulted in an overestimation of the thermal resistance of the wall assembly by 14% for both exterior temperatures, overestimation of the interior surface temperature by 0.8°C and 0.6°C for the -20°C and -35°C exterior temperatures, and very close approximation of the temperature through the depth of the mineral fibre. The overestimation of the 3D simulation results indicates that if more accurate results are

required, the individual VIPs used in the building assembly would have to be individually characterized with laboratory testing.

The 3D simulation results also indicate that increasing the steel stud gauge and simulating a centre stud sub-assembly with thermal symmetry boundary conditions can achieve reasonable results if correction factors are determined to relate the sub-assembly results to full assembly results. This requires further validation to be applied in other situations.

Overall the 3D simulation results were more accurate than the 2D simulation results, and equally as accurate as the modified zone calculation method results using the VIP effective thermal conductivity derived from using the average air joint width in the wall assembly. The 3D simulation results achieve reasonable accuracy for predicting the effect of the steel stud thermal bridge on the interior surface temperature.

# 9 Chapter: Conclusions and future work

Considering recent focus on improving building energy efficiency in Canada this thesis attempted to provide building designers and building code officials information regarding the level of detail required to properly estimate field performance of highly insulated wall assemblies containing thermal bridges. Several industry standard calculation methods for predicting the thermal resistance of a wall assembly were investigated for a wall assembly containing both steel studs and VIPs.

The calculation methods consisted of both industry standard calculation methods commonly used by building designers and two and three-dimensional numerical simulations using COMSOL Multiphysics®. Accuracy of the industry standard calculation methods and 2D simulations were improved through use of effective thermal conductivities of the VIPs, which accounted for edge and joint heat transfer effects. The calculation methods were compared to GHB test results for thermal resistance (hand calculation methods, simulations), effect of the steel stud thermal bridge on interior surface temperature (simulations) and temperature profile through the depth of the cavity insulation at the centre of the cavity (simulations). Uncertainties of both experiment values and calculation methods were also determined. Overall findings for each stage are discussed in the following sections.

## 9.1 Guarded hot box experiment

This thesis investigated the thermal resistance of a highly-insulated wall containing both steel studs and VIPs through GHB tests. In addition to determining the thermal resistance of the wall assembly, the wall was instrumented to determine the effect of the steel stud thermal bridge on the interior surface temperature, the temperature difference

between the centre and edge of a VIP and the temperature through the mineral fibre at the centre of the cavity. The GHB tests were conducted at steady state for two different exterior temperatures.

The steady state tests were conducted in accordance with ASTM C1363 at exterior air temperatures of -20°C and -35°C. The interior air temperature was held at 21°C for both tests. The resulting thermal resistance at each exterior temperature condition was calculated as 6.86 $m^2K/W$ (38.9 $hrft^2°F/BTU$) and 6.84 $m^2K/W$ (38.9 $hrft^2°F/BTU$) for the -20°C and -35°C exterior temperatures respectively.

Instrumentation of the interior and exterior sides of a VIP demonstrated that more heat transfer occurred at the edges of the panel than through the centre of the panel. This indicated that calculation methods that use the centre of panel value for thermal transmittance calculations are likely overestimating the performance of the wall assembly.

Instrumentation on the interior and exterior sides of the gypsum panel showed that the presence of steel studs in the wall assembly caused a temperature decrease of approximately 1.2°C for the gypsum surface temperature when compared to the centre of the stud cavity gypsum surface temperature for both exterior temperatures.

## 9.2 Industry standard calculation method conclusions

The thermal resistance results from GHB testing were used to determine the accuracy of several industry standard calculation methods. The results showed that the accuracy of the industry standard calculation methods could be improved by using effective VIP thermal conductivities.

The industry standard calculation methods consisted of the parallel path method, the isothermal planes method, the modified zone method, and the BRE 465 method. The VIP

effective thermal conductivities were determined using methods found in literature for relating the increased edge and joint heat transfer effects to the centre of panel thermal conductivity.

The results indicated that the most accurate industry standard calculation method was the modified zone method, and that use of effective thermal conductivities can improve the accuracy of the calculation methods. The modified zone calculation method with the ideal centre of panel thermal conductivity resulted in an overestimation of 38%. By using the effective thermal conductivity derived from the average air joint width in the assembly, the over estimation was reduced to 13%.

### 9.3 Numerical simulation conclusions

Two and three-dimensional numerical simulations were conducted of the wall assembly using the heat transfer package of COMSOL Multiphysics®. The values compared between the experiment and the simulations consisted of the thermal resistance, the interior surface temperature in proximity to the steel stud thermal bridge and the temperature through the depth of the mineral fibre at the centre of the stud cavity.

Comparing the 2D simulation results to the results of the modified zone calculation method indicated that the modified zone method gave a more accurate prediction for thermal resistance than the 2D simulations. The result based on the average gap thickness for the 2D

simulations resulted in an overestimation of 20%, compared to the 13% using the modified zone method. This requires further validation with other highly insulated wall assemblies.

The interior surface temperatures were also overestimated by the 2D simulations. This was again likely because the 2D model was unable to account for the horizontal thermal bridges present in the assembly due to the fiberglass clips and the horizontal air spaces.

The temperatures through the depth of the mineral fibre were also overestimated in most cases.

The 3D simulations resulted in an overestimation of 14.5% for the thermal resistance of the wall assembly. The overestimation is likely due to using the ideal VIP centre of panel (COP) thermal conductivity. The 3D simulation resulted in a more accurate prediction of the thermal resistance than the 2D simulations, but equally accurate to the modified zone calculation method. The 3D simulation achieves better accuracy at predicting the effect of the steel stud thermal bridge on the interior surface temperature than the 2D simulations. The results also indicate that simulating a sub-assembly with increased gauge studs can result in reliable results when correction factors are developed to relate the sub-assembly thermal performance to a full assembly.

## 9.4 Overall conclusions

Overall this thesis confirmed findings from others in literature that calculating the thermal resistance of wall assemblies containing VIPs using centre of panel values results in a significant overestimation of the wall assembly thermal performance (ASHRAE, 2011; Tenperik & Cauberg, 2007; Van Den Bossche, Moens, Janssens, & Delvoye, 2010; Wakili, Bundi, & B.Binder, 2004). The results in this thesis demonstrated that the accuracy of industry standard calculation methods and 2D simulations can be improved if the effective

thermal conductivity of the VIP is used. Several methods from literature to predict the effective thermal conductivity of the VIP were evaluated, and the most accurate methods accounted for the air joint between VIPs.

For the single wall evaluated in this thesis the results also indicated that if thermal resistance is the only performance metric desired of the wall assembly, an industry standard calculation method which properly accounts for the edge and joint heat transfer effects of the VIP can achieve results just as accurate as 3D simulations. Further evaluation of other wall assembly types is required to determine if this finding is applicable in other instances.

The results in this thesis were derived using published material property values for each material in the wall assembly. The results indicate that each calculation method still overestimates both the thermal resistance of the wall assembly, and the temperatures that occur within it using these material properties. This indicates that if results are desired better than a 13% overestimation, more accurate material properties may be required. In this case the largest uncertainty in material properties exists due to the VIP. The other materials have well established well defined material properties. Also, the thermal resistance of the VIP was estimated to provide just over 50% of the thermal resistance to the wall assembly. Therefore, the most likely area to increase accuracy of the calculation methods is to more accurately determine the thermal resistance of the VIP.

## 9.5 Future work

This thesis focused on predicting the thermal performance of a steel stud wall assembly containing VIPs at the start of service life. Due to the technology used by VIPs it is expected that the thermal resistance of the VIP decreases over time, due to atmospheric gas and vapour transmission across the barrier envelope. Future work would be to couple

the calculation methods evaluated in this thesis with a service life prediction model, to give designers a realistic idea of the long-term performance of such a wall assembly.

Although end of service life definitions are generally defined for VIPs (ASTM, 2009; Schwab, Heinemann, Beck, Ebert, & Fricke, 2005), the actual estimate of that service life in field conditions is still being developed. Comparisons of existing service life prediction equations seem to overestimate the service life performance of VIPs in field conditions (Brunner & Simmler, 2003). Further work is required to give designers an easy to use tool which predicts service life to a reasonably accurate degree.

Additionally, there is a need to update the industry standard calculation methods in situations where significant heat transfer through thermal bridges is expected, such as VIP wall systems. There is a need for either a publicly available thermal transmittance calculator/database, or a standardized simulation method to predict thermal resistance in wall assemblies. The 3D model from this thesis could be further validated with other wall systems to provide a base for either the thermal transmittance database, or the standardized simulation method.

## Bibliography


Alam, M. S. (2011). Vacuum Insulation Panels (VIPs) for building construction industry – A review. *Applied Energy 88*, 3592-3602.

Anderson, B. (2006). *Conventions for U value Calculations.* Garsten, Watford, Scotland: BRE Press.

ASHRAE. (2011). *RP-1365 Thermal Performance of Building Envelope Details for Mid-And High-Rise Buildings.* ASHRAE.

ASHRAE. (2013). *2013 ASHRAE Handbook Fundamentals.* Atlanta, GA, U.S.: ASHRAE.

ASHRAE. (2016). *ASHRAE 90.1.*

ASHRAE. (2016). *ASHRAE Handbook of Fundamentals.*

ASHRAE. (2016). *ASHRAE Standard 160-2016 -- Criteria for Moisture-Control Design Analysis in Buildings* . ASHRAE.

ASTM. (2009). *ASTM C1484-09 Standard Specificaion for Vacuum Insulation Panels.* West Conshohoken, PA: ASTM International.

ASTM. (2010). *ASTM C168-10 Standard Terminology Relating to Thermal Insulation.* West Conshohocken, PA: ASTM International.

ASTM. (2013). ASTM C 1363 - Thermal Performance for Building Materials and Envelope Assemblies by means of a Hot Box apparatus. *ASTM Standards*.

ASTM. (2015). ASTM C518 - Standard Test Method for Steady-State Thermal Transmission Properties by Means of the Heat Flow Meter Apparatus.

Bowen, R., & Solvason, K. (1987). A Calorimeter for determining heat transmission characteristics of windows. *Thermal insulation: materials and systems* (pp. 567-81). Dallas: ASTM .

Brown, W. C., & Ullett, J. M. (1992). *Assessment of the Thermal Performance of the NVLAP Round Robin Wall Specimen in IRC's Guarded Hot Box Facilities.* Ottawa: National Research Council Canada.

Brown, W., & Schwartz, N. (1987). The thermal and air leakage perfromance of residential walls. *SPIC 7th Annual Canadian Rigid Polyurethane Foam Conference* (pp. 1-10). Huntsville, ON: SPIC.

Brown, W., & Stephenson, D. (1993). Guarded hot box measurements of the dynamic heat transmission characteristics of seven wall specimens - Part II. *ASHRAE Transactions*, 643-660.

Brunner, S., & Simmler, H. (2003). Service Life Prediction in vacuum insulation panels. *CISBAT.* Lausanne.

Brunner, S., & Wakili, K. (2014). Hints for an additional aging factor regarding the thermal performance of vacuum insulation panels with pyrogenic silica core. *Vacuum 100*, 4-6.

Brunner, S., Stahl, T., & Wakili, K. G. (2012). Single and double layered vacuum insualtion panels of the same thickness comparison. *Building Enclosure Science Technology Conference (BEST3).* Atlanta.

Canada, G. o. (2017). *Pan Canadian Framework on Clean Growth and Climate Change.* Ottawa: Government of Canada.

COMSOL AB. (2017). *COMSOL Multiphysics(R) v. 5.2.* Stockholm, Sweden: COMSOL AB.

Dassault Systemes. (2016). *Soldiworks(r) Mechanical 3D CAD.* Waltham, Massachusetts, USA: Dassault Systemes.

Elmahdy, A. H. (1992). Heat Transmission and R-value of fenestration systems using the IRC hot box: procedure and analysis. *ASHRAE Transactions 98*, 630-637.

Elmahdy, A. H., & Haddad, K. (2000). Experimental procedure and uncertainty analysis of a guarded hot box method to determine the thermal transmission coefficient of skylights and sloped glazing. *ASHRAE Transactions 106*, 601-613.

Fricke, J. (2005). From Dewars to VIPs - One Century of Progress in Vacuum Insulation Technology. *7th International Vacuum Insulation Symposium 2005* (pp. 5-14). Zurich, Switzerland: EMPA.

Gorgolewski, M. (2007). Developing a simplified method of calculating U values in light steel framing. *Building and Environment, 42*, 230-236.

H.Simmler, S. B. (2005). *IEA Annex 39.* International energy agency. EMPA.

Incopera, F. P. (2006). *Fundamentals of Heat and Mass Transfer 6th edition.* Hoboken, N.J., U.S.: John Wiley and Sons Inc.

ISO. (2007a). *ISO 10211 Thermal bridges in building constructions - Heat flows and surface temepratures - Detailed Calculations.* Switzerland: ISO.

ISO. (2007b). *ISO 14683 Thermal bridges in building construction - Linear thermal transmittance - Simplified methods and default values.* Switzerland: ISO.

ISO. (2007c). *ISO 6946:2007 Building components and building elements -- Thermal resistance and thermal transmittance -- Calculation method.* Geneva, Switzerland: Internation Organization for Standardization.

IVIS. (2007). IVIS 7th International Vacuum Symposium.

J. M. Ullet, M. C. (1995). *Effect of Stud Guage and Insulating Sheathing on the Thermal Performance of Steel Stud Walls.* Ottawa, ON, Canada: National Research Council Canada.

Keysight Technologies. (2017, January 16). *Agilent 34970a Data Acquisition / Data Logger Switch Unit*. Retrieved from Keysight Technologies: http://www.keysight.com/en/pd-1000001313%3Aepsg%3Apro-pn-34970A/data-acquisition-data-logger-switch-unit?nid=-33261.536881544.00&cc=CA&lc=eng

Kosny, J. (1995, July). Comparison of Thermal Performance of Wood Stud and Metal Frame Wall Systems. *Thermal Insulation and Budiling Environments, 19*.

Kumaran, M. (2006). A Thermal and moisture property database for common building and insulation materials. *ASHRAE Transactions, 112 pt. 2*, (pp. 1-13).

Lackey, J., Normandin, N., Marchand, R., & Kumaraman, M. (1994). Calibration of a Heat Flow Meter Apparatus. *Journal of Thermal Insulation and Buidling Envelopes*, 128-144.

Lorenzati, A., Fantucci, S., Capozzoli, A., & Perino, M. (2014). The effect of different materials joint in vacuum insulation panels. *6th International Conference on Sustainability in energy and Buidlings*, (pp. 374-381).

Maref, W., Van Den Bossche, N., Armstrong, M., Lacasse, M. A., Elmahdy, H., & Glazer, R. (2012). Condensation risk assessment on box windows : the effect of the window-wall interface. *Journal of Building Physics*, 35-56.

Moffat, R. (1988). Describing the Uncertainties in Experimental Results. *Experimental and Thermal Science*, 1:3-17.

Morris and Hershfield Ltd. (2011). *Thermal Performance of Envelope Details for Mid- and High-Rise Buildings(1365-RP).* Vancouver, B.C., Canada: Morris and Hershfield Ltd.

Morris and Hershfield Ltd. (2014). *Building Envelope Thermal Bridging Guide.*

National Research Council Canada. (2015). National Building Code.

Nations, U. (2015). *Paris Agreement.* United Nations.

Nicholas, J., & White, D. (1994). *Traceable Temperatures - An Introduction to Temperature Measurement and Calibration.* West Sussex, England: John Wiley & Sons Ltd.

NRC. (2016). *National Energy Code for Buildings Canada.* Ottawa, ON: National Research Council Canada.

OMEGA Engineering inc. (2017, January 15). *Thermocouple Wire Special Limits of Error*. Retrieved from OMEGA : http://www.omega.ca/pptst_eng/SLE_Wire.html#description

S. Doran, M. G. (2002). *U-values for light steel frame construction (Digest 465).* BRE.

Schwab, H., Heinemann, U., Beck, A., Ebert, H., & Fricke, J. (2005). Prediction of Service Life for Vacuum Insulation PAnels with Fumed Silica Kernal and Foil Cover. *Journal of Thermal Env. & Bldg. Sci., Vol 28, No 4*, 357-374.

Schwab, H., Stark, C., Wachtel, J., Ebert, H.-P., & Fricke, J. (2005). Thermal Bridges in Vacuum-insulated Building Facades. *Journal of Thermal Env. and Bldg. Sci.*, 345-355.

Simko, T., Elmahdy, A., & Collins, R. (1998). Determination of the overall heat transmission coefficient (u-value) of vacuum glazing. *ASHRAE Transactions* (pp. 1-9). Toronto, ON: ASHRAE.

Simmler, H., Brunner, S., Heinemann, U., Schwab, H., Kumaran, M. K., Mukhopadhyaya, P., . . . Kucukpinar-Niarchos, E. (2005). *International Energy Agency Annex 39: High Performance Thermal Insulation Materials, Subtask A: Vacuum insulation panels - study on VIP-components and panels for service life prediction of VIP in building applications.* Paris, France: IEA/ECBCS.

Sprengard, C., & Holm, A. (2014). Numerical examination of thermal bridging effects at the edges of vacuum insulation panels (VIP) in various constructions. *Energy and Buildings 85*, 638-643.

Tenperik, M., & Cauberg, H. (2007). Effects Caused by Thin High Barrier Envelopes around Vacuum Insulation Panels. *Journal of Building Physics*.

Tenpierik, M., van der Spoel, W., & Cauberg, J. (2007). Simplified analytical service life prediction of a vacuum insulation panel. *8th International Vacuum Insulation Symposium*, (pp. 1-8). Wurzburg.

Van Den Bossche, N., Moens, J., Janssens, A., & Delvoye, E. (2010). *Thermal Performance of VIP panels: Assessment of the edge effect by experimental and numerical analysis.* Ghent: Ghent University, Department of Architecture and Urban Planning.

Wakili, K. G., Bundi, R., & B.Binder. (2004). Effective thermal conductivity of vacuum insulation panels. *Building Research and Information*, 293-299. doi:10.1080/0961321042000188644

# Appendices

## Appendix A **Experiment data plots thermopile calibration**

The thermopile calibration consisted of inducing a temperature difference between the room-side guard and the calorimeter (metering box) to determine the corresponding heat transfer between the room side and metering box versus the thermopile voltage generation ($E_0$). In this set-up, a positive value for the thermopile voltage corresponds to heat transferring from the room side guard to the metering box. Conversely, a negative value for the thermopile voltage corresponds to heat transfer from the metering box to the room side. The heat transfer rate for a given thermopile voltage was determined for several scenarios. At an exterior temperature of -20°C, the heat transfer rate between the room side guard and the metering box was determined for six average thermopile voltages. The data used to determine the average value for each scenario is presented in Figure 55 to Figure 60.

At an exterior temperature of -35°C, the heat transfer rate was determined for three thermopile voltages. The data used to determine the average value for each scenario for the is presented in Figure 61 to Figure 63.

For the raw data, the cyclic nature of the 15-minute averages can be attributed to the cycling of the heater in the metering box.

## A.1 -20°C Exterior temperature:

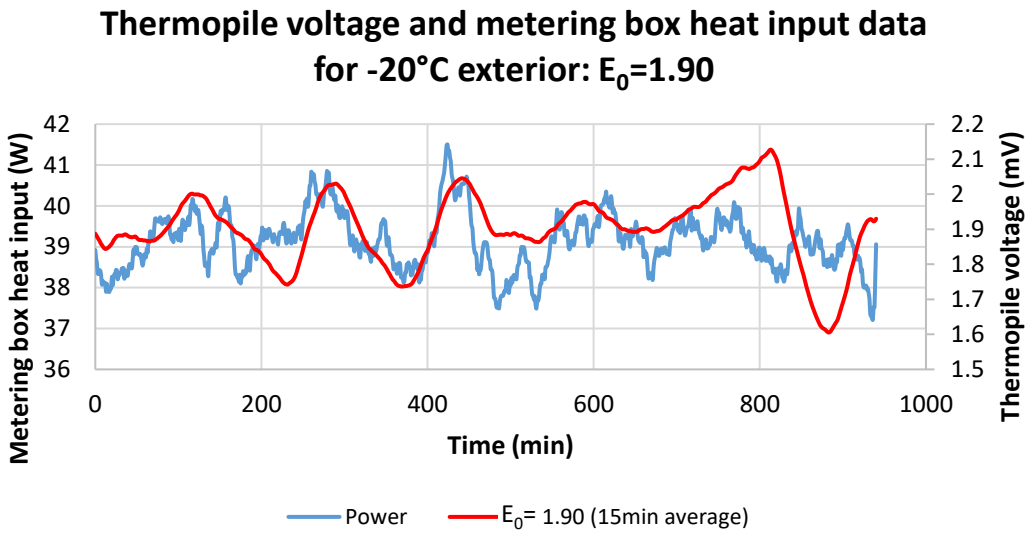


**Figure 55: Thermopile voltage and calorimeter heat data from the -20°C test inducing an average of $E_0$=1.90 for the thermopile.**

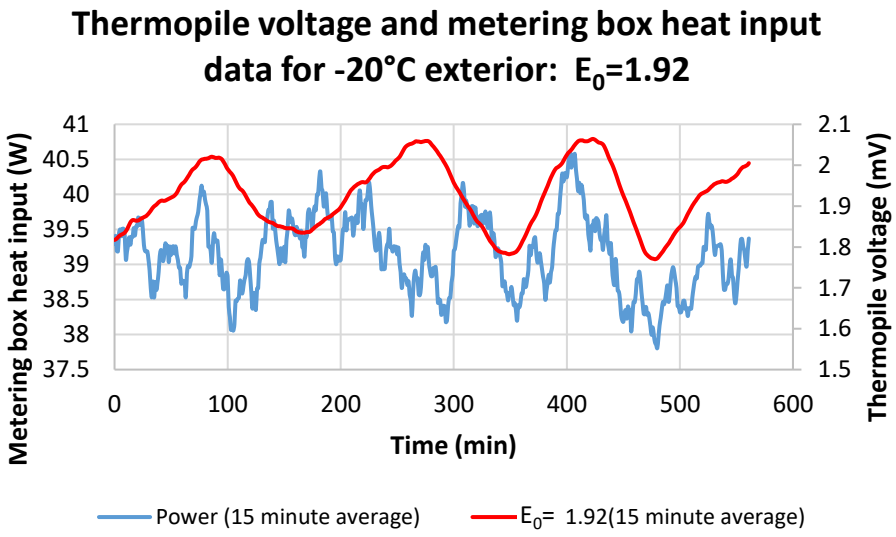


**Figure 56: Thermopile voltage and calorimeter heat data from the -20°C test inducing an average of $E_0$=-1.92 for the thermopile.**

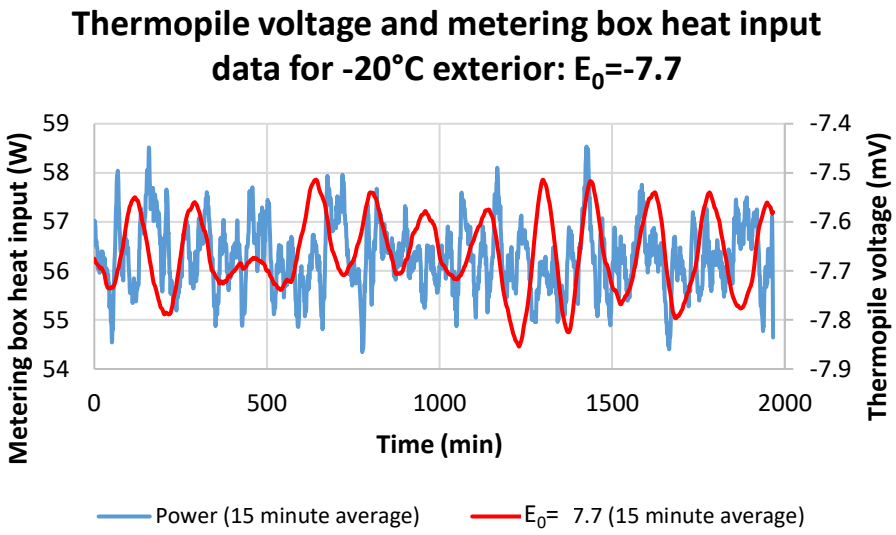


**Figure 57: Thermopile voltage and calorimeter heat data from the -20°C test inducing an average of $E_0$=-7.7 for the thermopile.**

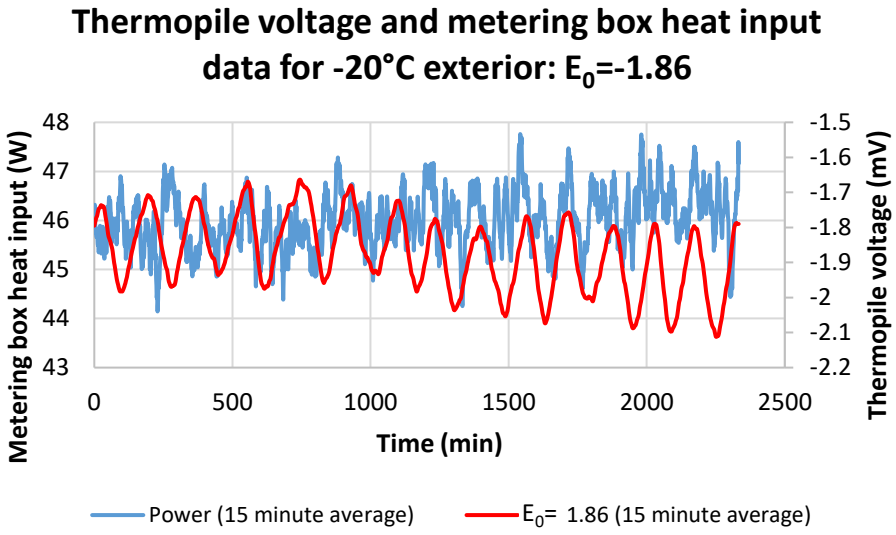


**Figure 58: Thermopile voltage and calorimeter heat data from the -20°C test inducing an average of $E_0$=-1.86 for the thermopile.**

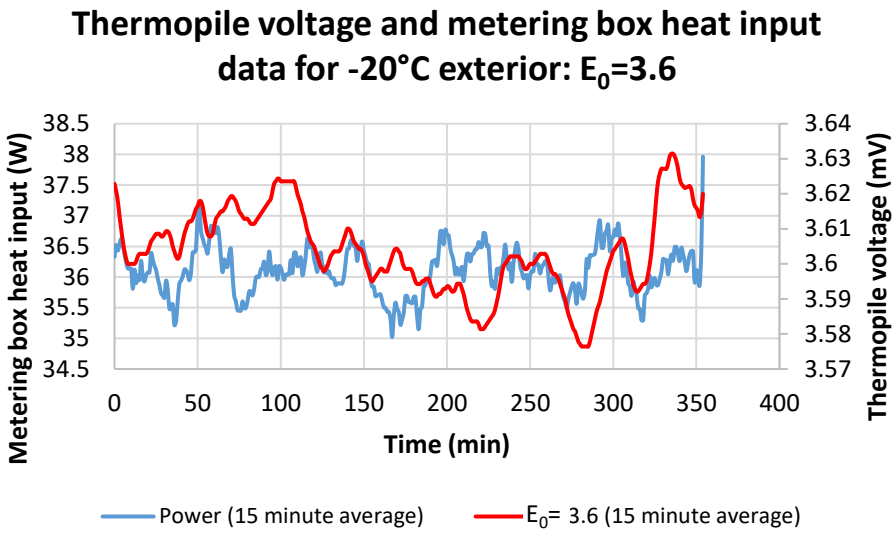


**Figure 59: Thermopile voltage and calorimeter heat data from the -20°C test inducing an average of $E_0$=3.6 for the thermopile.**

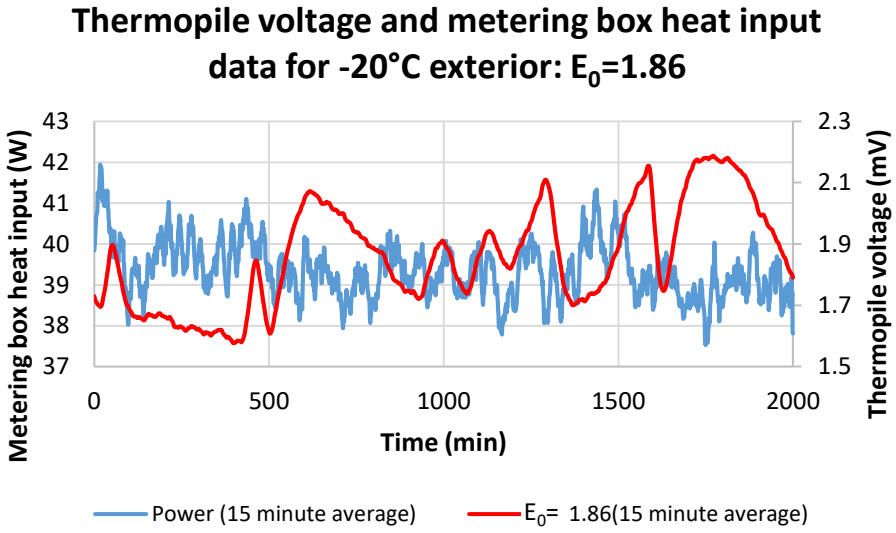


**Figure 60: Thermopile voltage and calorimeter heat raw data from the -20°C test inducing an average of $E_0$=1.86 for the thermopile.**

## A.2 -35°C Exterior temperature:

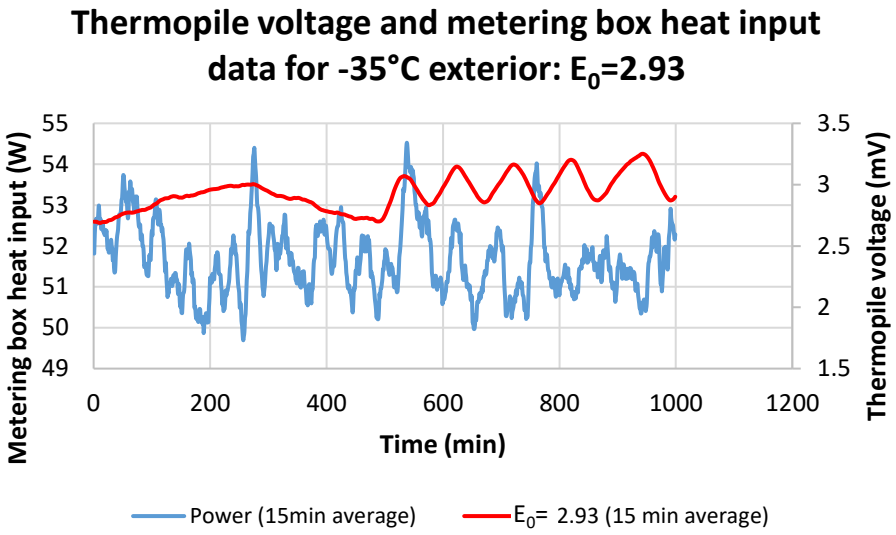


**Figure 61: Thermopile voltage and calorimeter heat raw data from the -35°C test inducing an average of $E_0$=2.93 for the thermopile.**

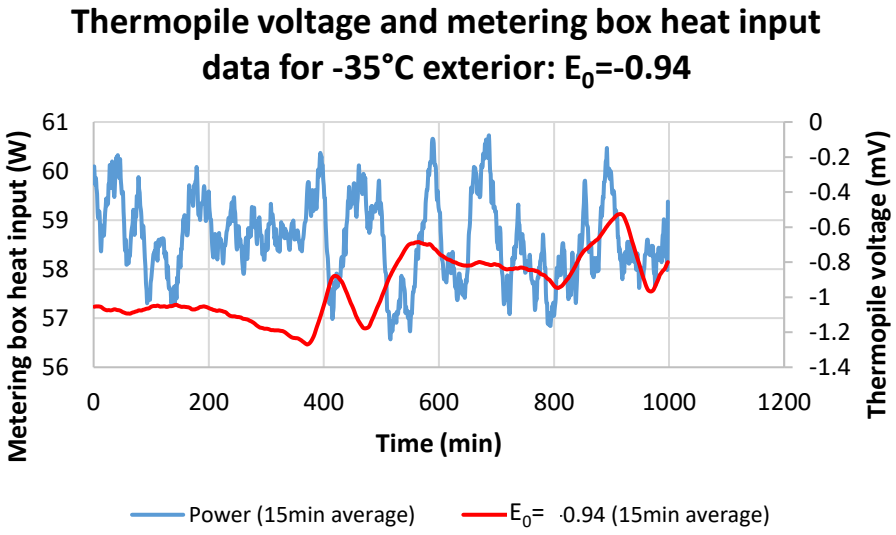


**Figure 62: Thermopile voltage and calorimeter heat raw data from the -35°C test inducing an average of $E_0$=-0.94 for the thermopile.**

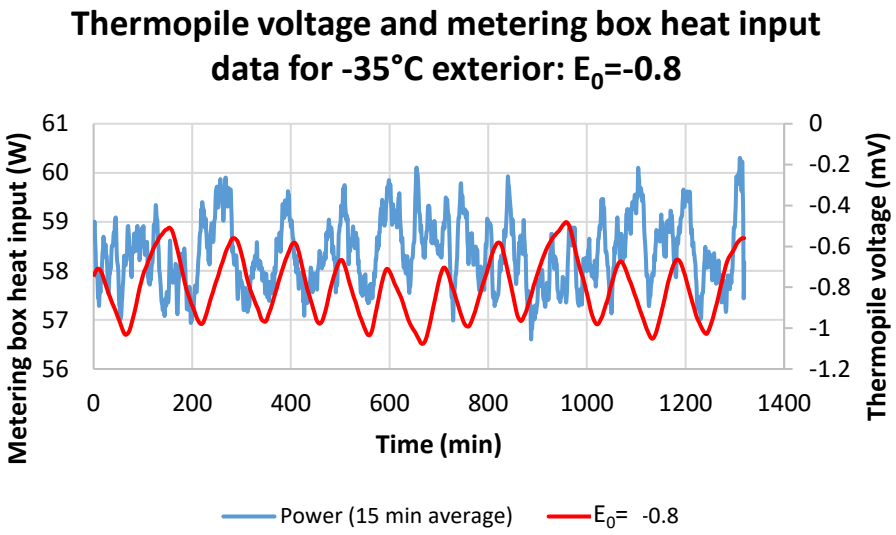


**Figure 63: Thermopile voltage and calorimeter heat raw data from the -35°C test inducing an average of $E_0$=-0.8 for the thermopile.**

## Appendix B **Experiment data guarded hot box characterization**

This appendix presents the data used to determine the average temperatures used in the characterization of the guarded hot box facility. These averages were used to determine the surface heat transfer coefficients (modelling boundary conditions), as well as the combined metering box and flanking loss at a thermopile voltage equal to zero.

The data provided is for both the -20°C and -35°C exterior temperatures. The data was used to determine average values for metering box air temperature, metering box specimen surface temperature, weather side specimen surface temperature, weather side air temperature, the total heat provided by the heater to the metering box and the thermopile voltage. The data for each of these parameters is presented in Figure 64 to Figure 68, for the -20°C exterior temperature, and Figure 69 to Figure 73, for the -35°C exterior temperature.

## B.1 -20°C Exterior temperature

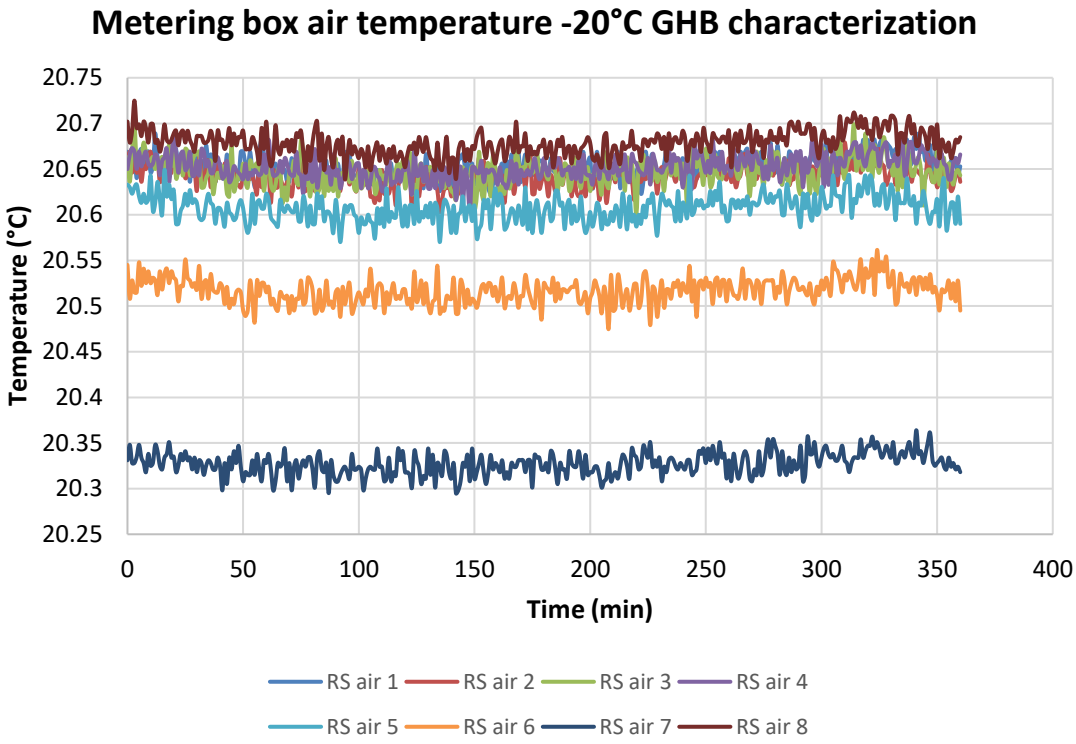


**Figure 64: Metering box air temperature during -20°C exterior GHB characterization.**

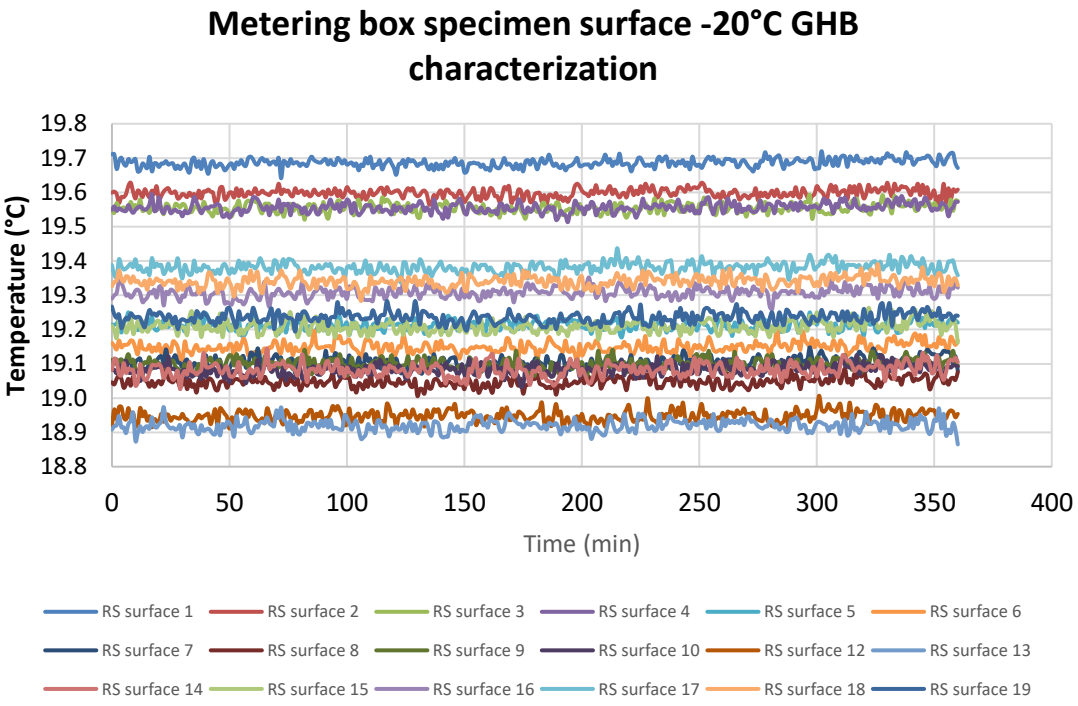


**Figure 65: Metering box specimen surface temperature during -20°C exterior GHB characterization.**

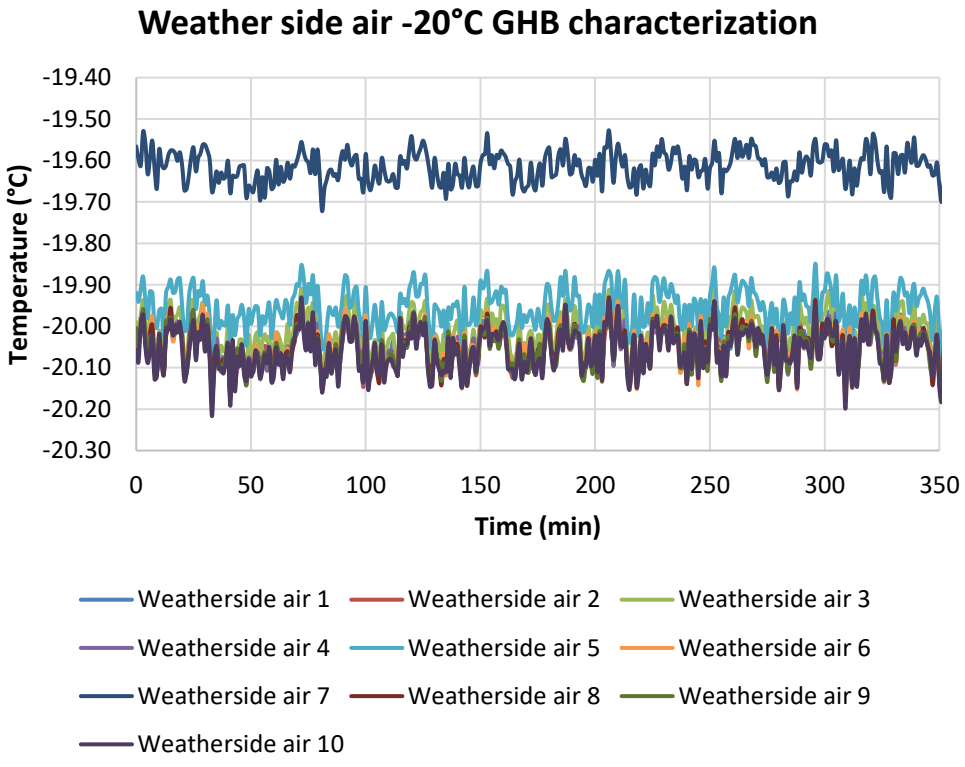


**Figure 66: Weather side air temperature during -20°C exterior GHB characterization.**

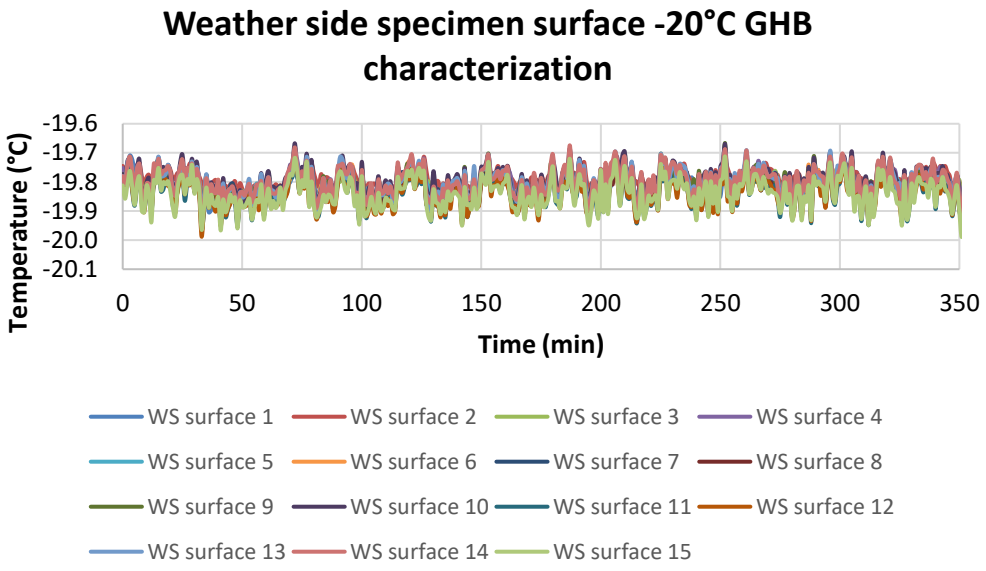


**Figure 67: Weather side specimen surface temperature during -20°C exterior GHB characterization.**

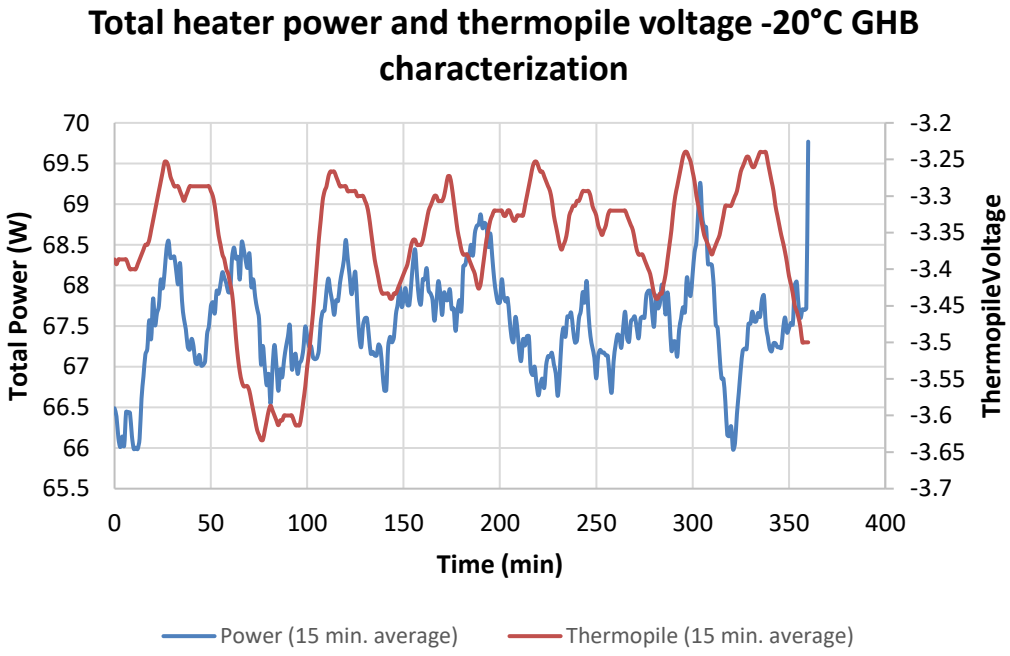


**Figure 68: Total heater power and thermopile voltage during -20°C exterior GHB characterization.**

## B.2 -35°C Exterior Temperature

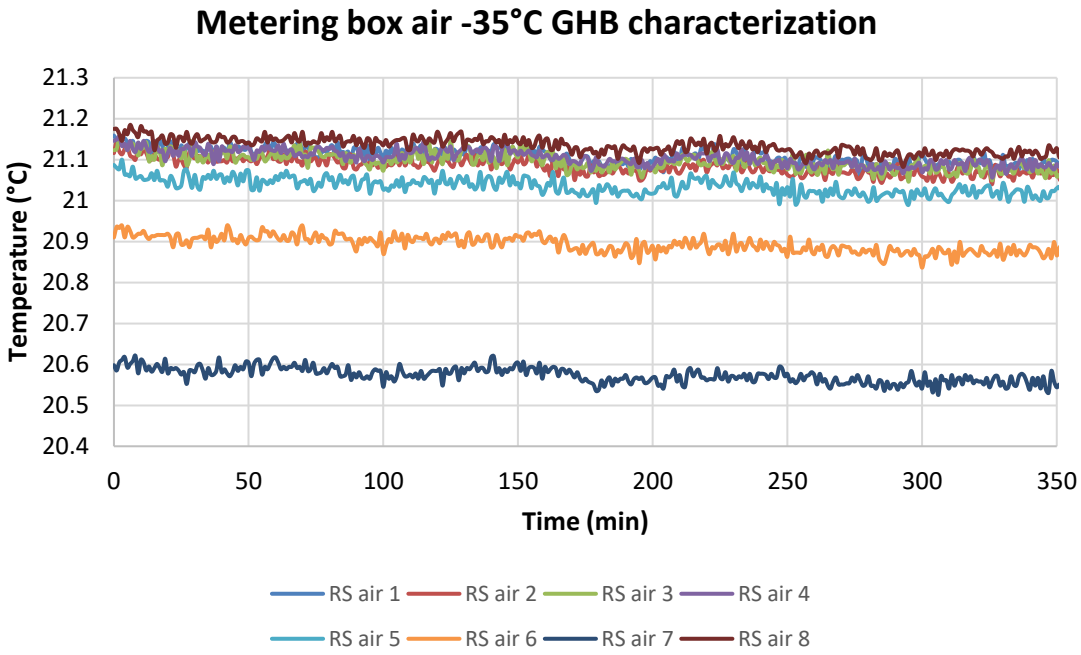


**Figure 69: Metering box air temperature during -35°C exterior GHB characterization.**

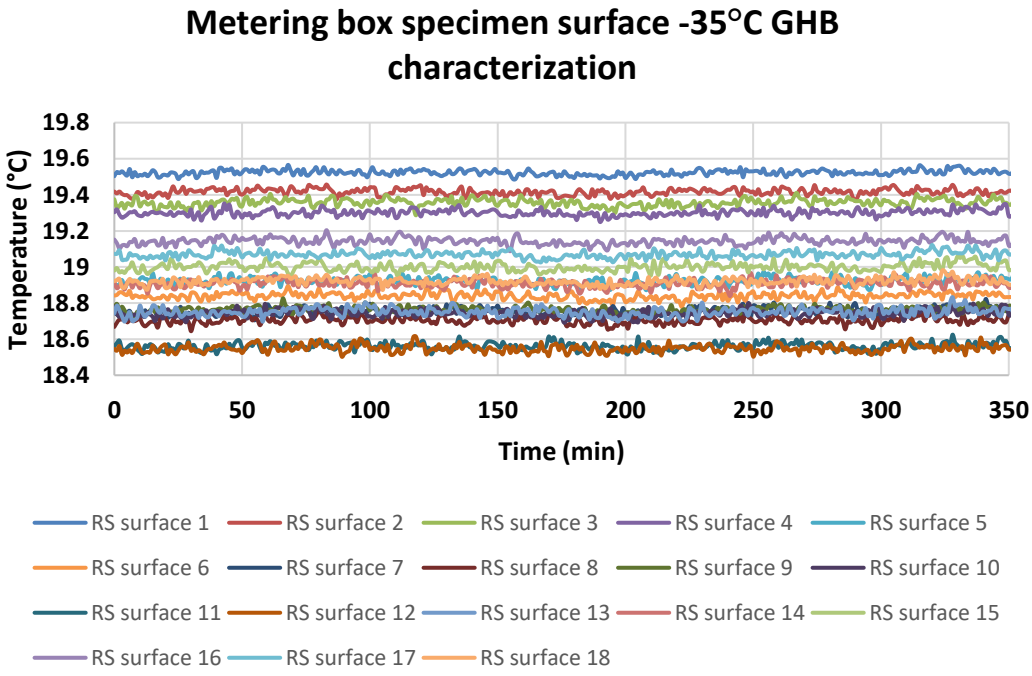


**Figure 70: Metering box specimen surface temperature during -35°C exterior GHB characterization.**

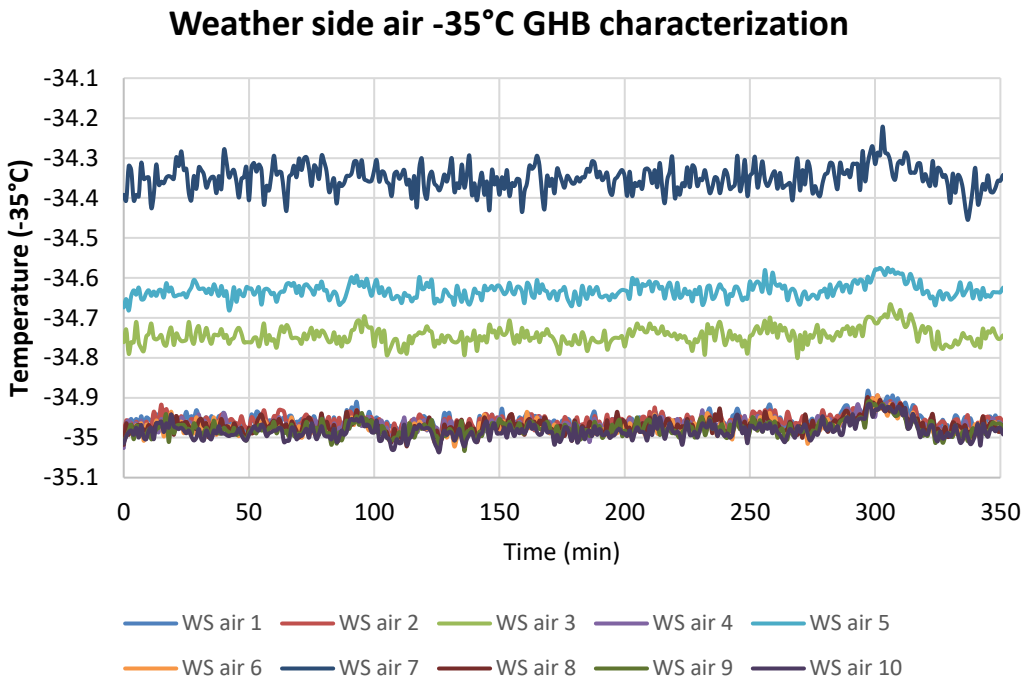


**Figure 71: Weather side air temperature during -35°C exterior GHB characterization.**

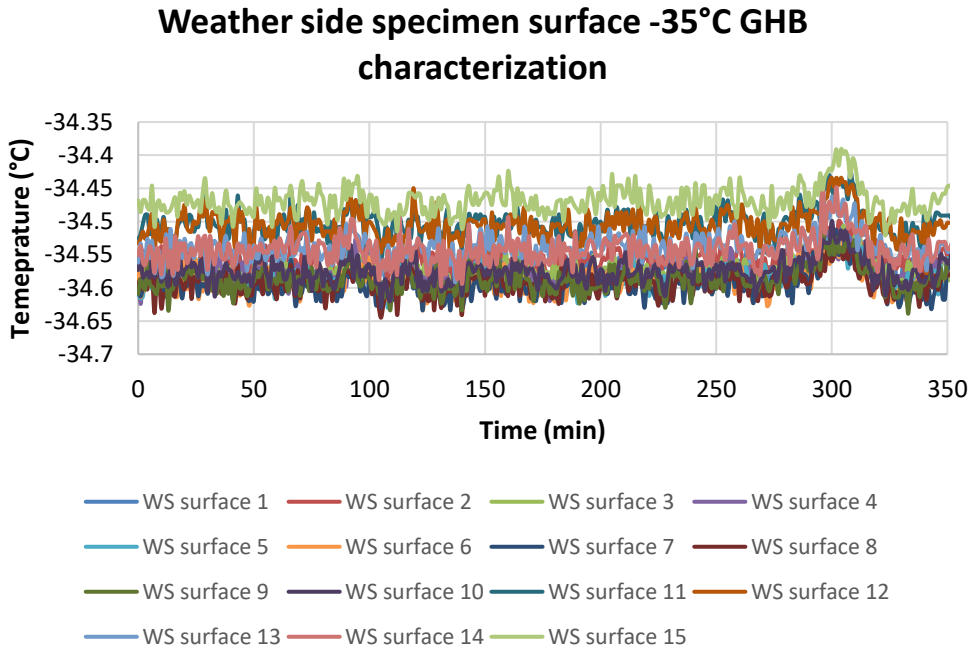


**Figure 72: Weather side specimen surface temperature during -35°C exterior GHB characterization.**

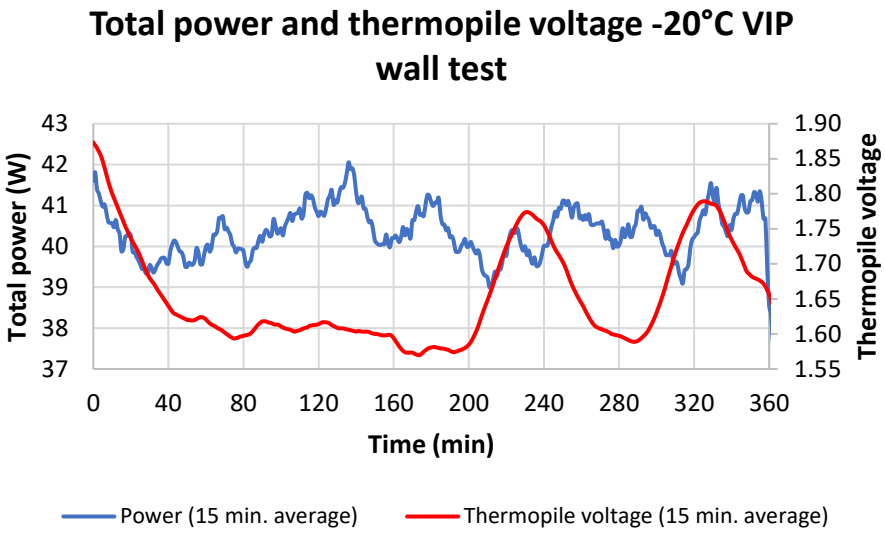


**Figure 73: Total heater power to the calorimeter and thermopile voltage during -35°C exterior mask calibration.**

Appendix C **Experiment data plots -20°C VIP wall**

This appendix presents the experiment data from the VIP wall thermal resistance test conducted in the GHB for the -20°C exterior temperature. The data presented was used to determine average values for the metering box air temperature, metering box specimen surface temperature, weather side specimen surface temperature, weather side air temperature, the temperature through the depth of the mineral fibre, total power consumption of the metering box heater and the thermopile voltage. The data for each parameter are presented in Figure 74 to Figure 79.

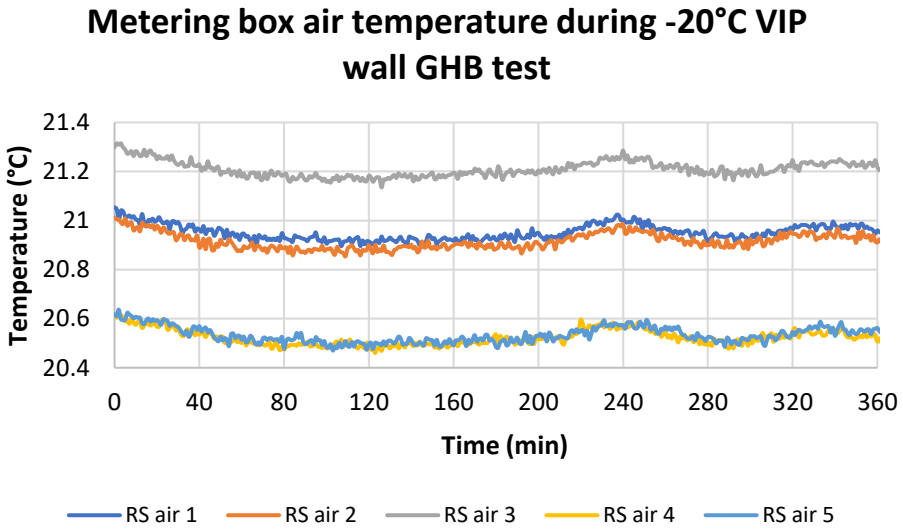


**Figure 74: Metering box air temperature raw data during -20°C experiment on the VIP wall specimen.**

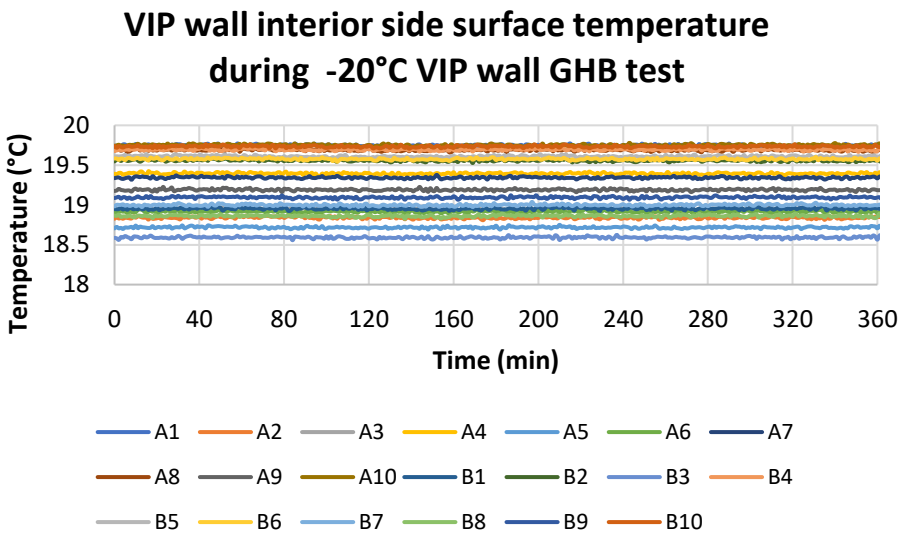


**Figure 75: VIP wall interior side surface temperature raw data during -20°C experiment.**

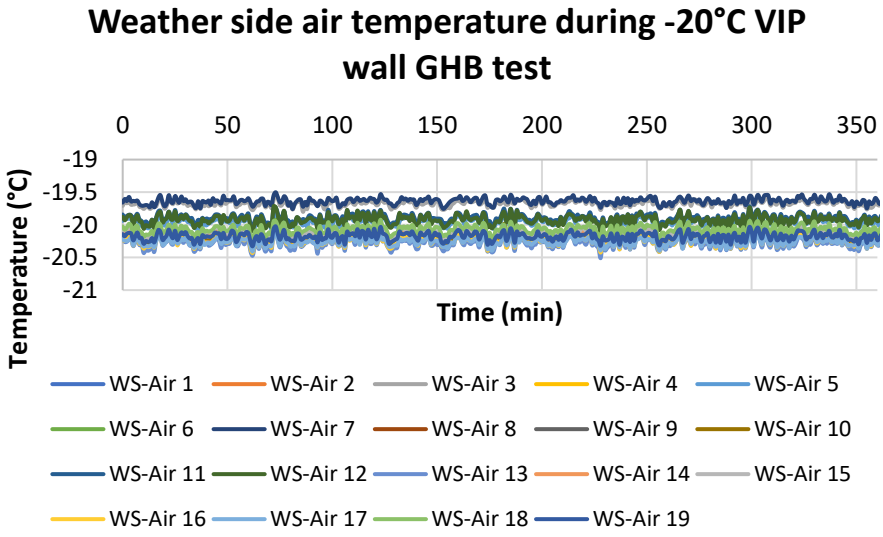


**Figure 76: Weather side air temperature raw data during -20°C experiment on the VIP wall specimen.**

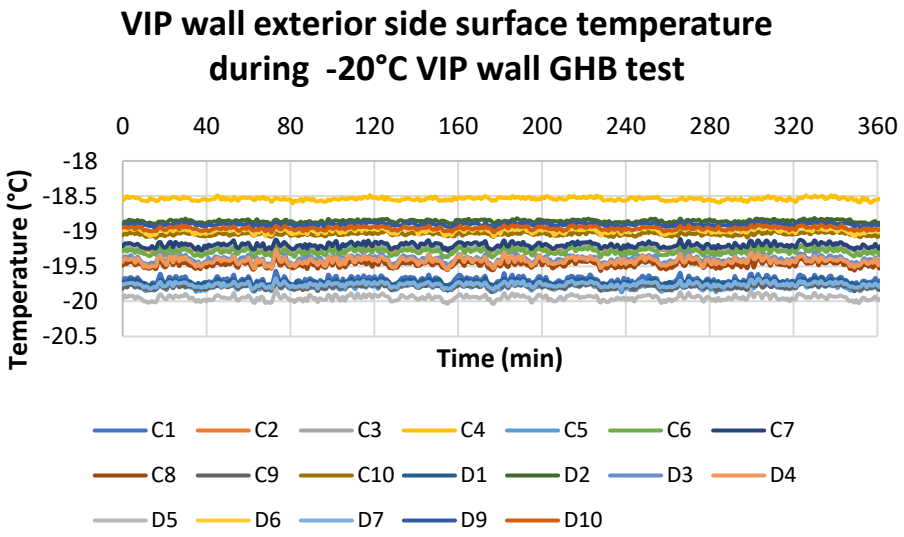


**Figure 77: Weather side surface temperature raw data during -20°C experiment on the VIP wall specimen.**

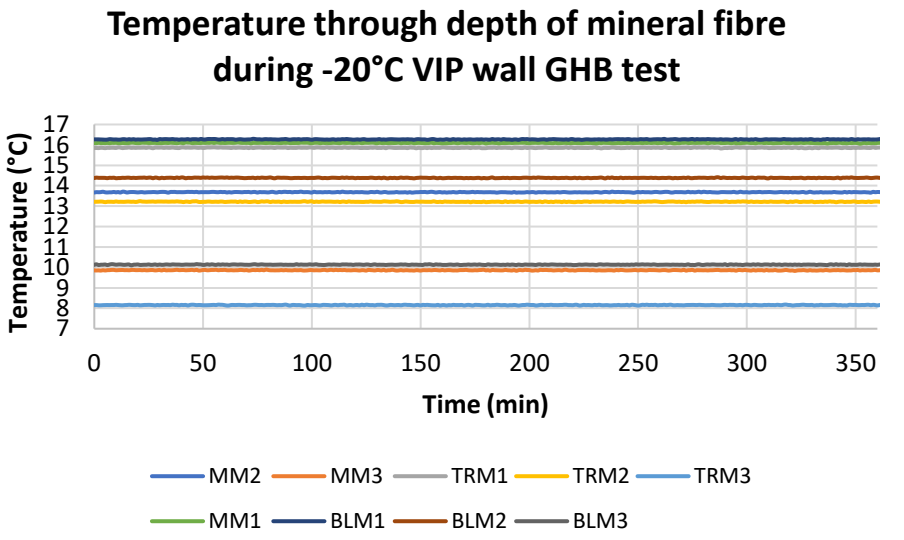


**Figure 78: Temperature through the depth of mineral fibre raw data during -20°C experiment on the VIP wall specimen.**

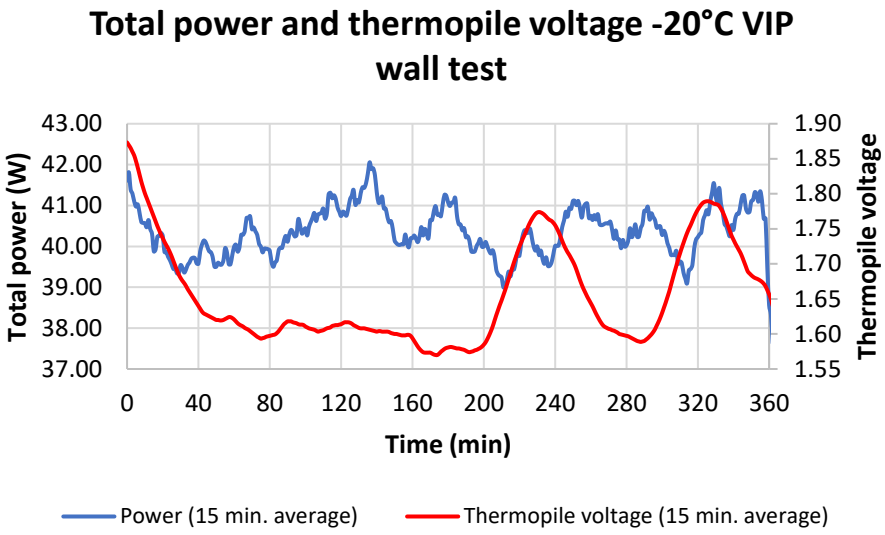


**Figure 79: Total heat input to the calorimeter and thermopile voltage raw data during -20°C experiment on the VIP wall specimen.**

Appendix D **Experiment data plots -35°C VIP wall**

This appendix presents the experiment data from the VIP wall thermal resistance test conducted in the GHB for the -35°C exterior temperature. The data presented was used to determine average values for the metering box air temperature, metering box specimen surface temperature, weather side specimen surface temperature, weather side air temperature, the temperature through the depth of the mineral fibre, total power consumption of the metering box heater and the thermopile voltage. The data for each parameter are presented in Figure 80 to Figure 85.

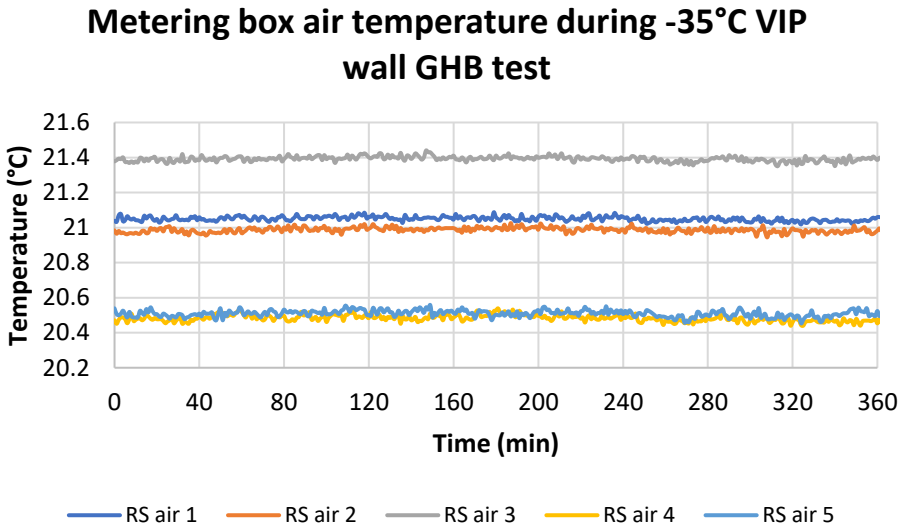


**Figure 80: Room side air temperature raw data during -35°C experiment on the VIP wall specimen.**

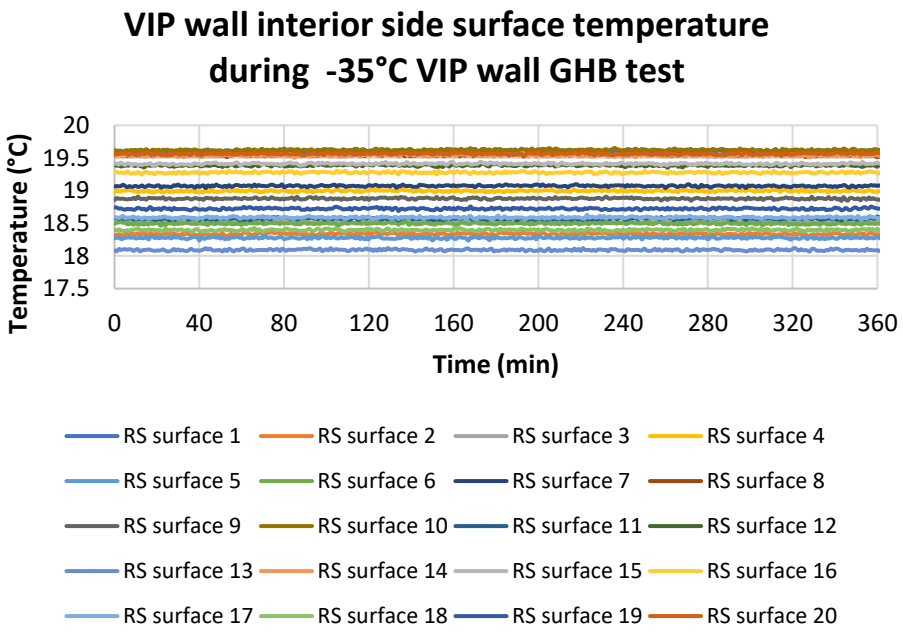


**Figure 81: Room side surface temperature raw data during -35°C experiment on the VIP wall specimen.**

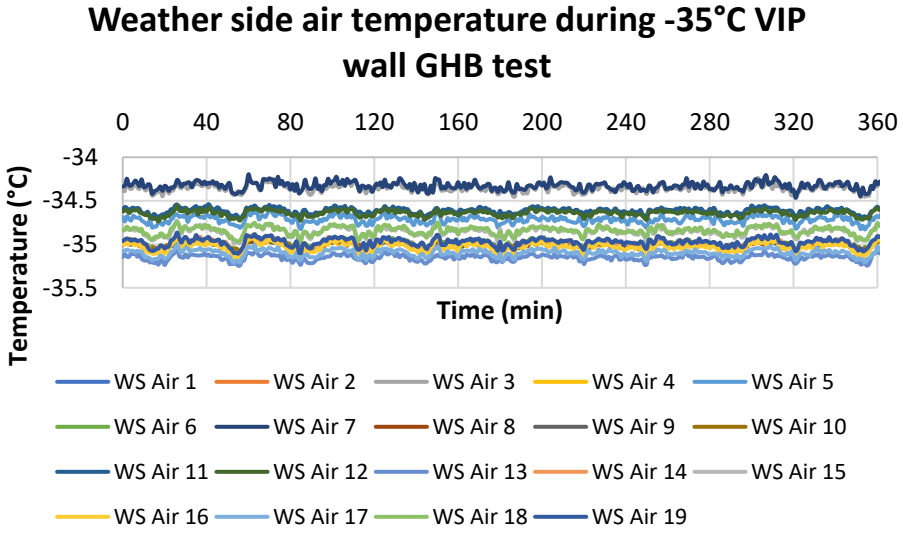


**Figure 82: Weather side air temperature raw data during -35°C experiment on the VIP wall specimen.**

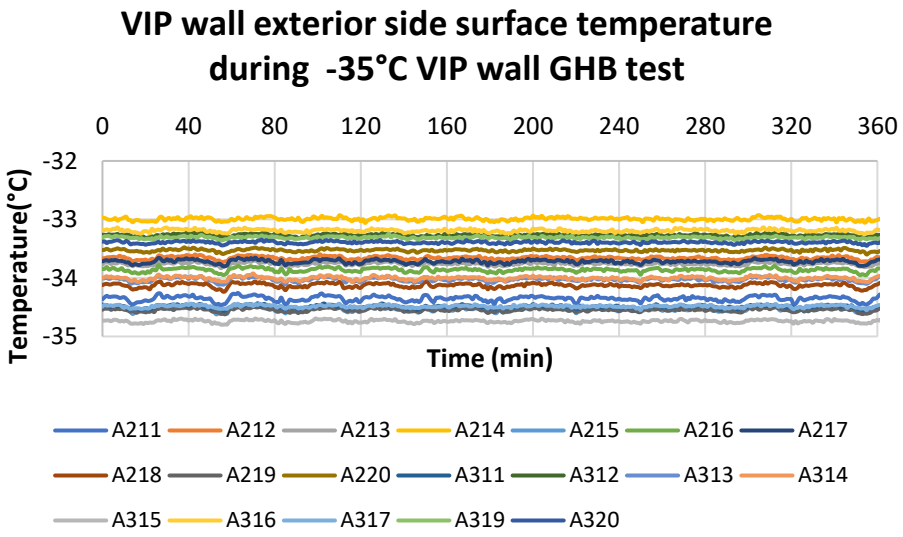


**Figure 83: Weather side surface temperature raw data during -35°C experiment on the VIP wall specimen.**

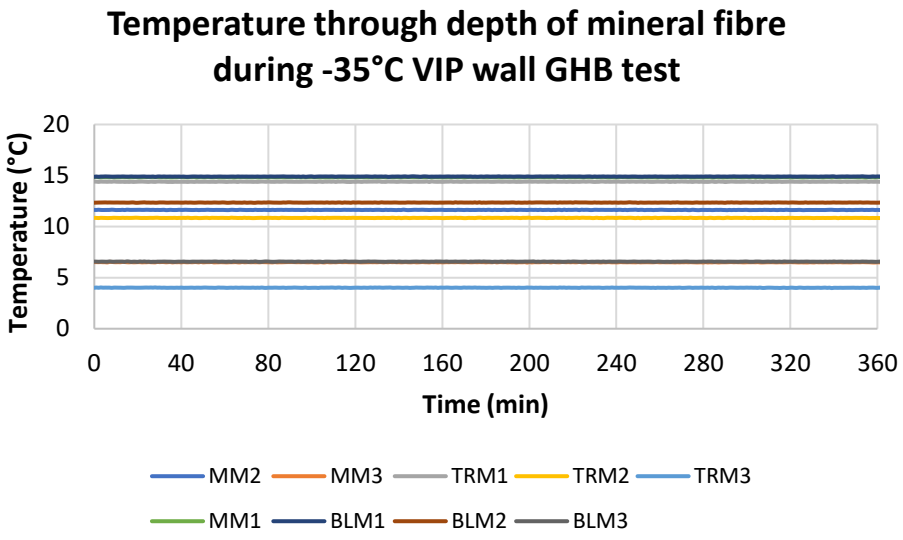


**Figure 84: Temperature through the depth of mineral fibre raw data during -35°C experiment on the VIP wall specimen.**

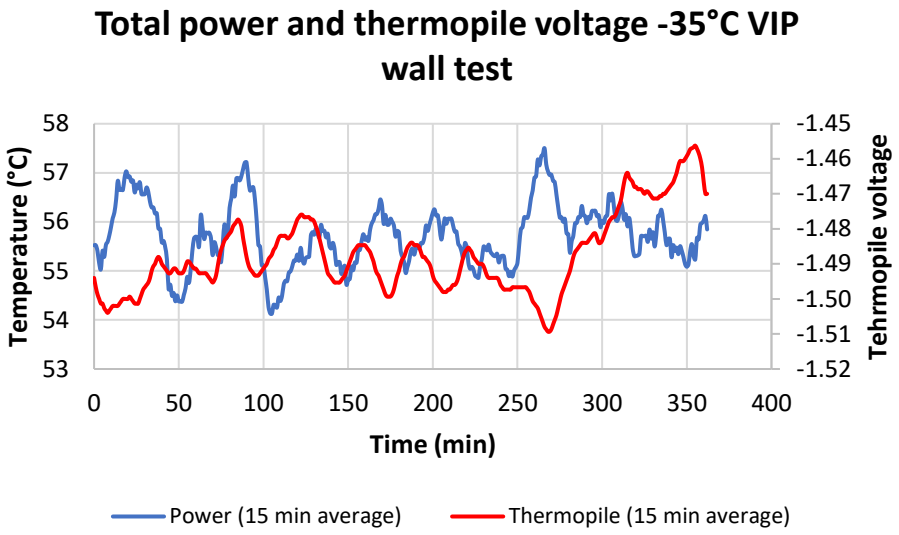


**Figure 85: Total heat input to the calorimeter and thermopile voltage raw data during -35°C experiment on the VIP wall specimen.**

Appendix E **Thermal resistance calculation uncertainty**

The following appendix presents the calculations used to determine the root sum square (RSS) uncertainty for each component used to calculate the thermal resistance determined using the GHB apparatus. The uncertainties required to determine the overall uncertainty for the thermal resistance equation consist of the temperature measurement uncertainty, the uncertainty on the power dissipation of the heater in the metering box, the uncertainty in the combined metering box and flanking loss and finally the uncertainty of the heat transfer through the wall specimen. The following sections present the uncertainty calculations for each parameter listed. The uncertainty of each parameter is combined in the final section to determine the overall uncertainty for the thermal resistance calculation.

## E.1 Temperature uncertainty

As discussed in Chapter 5, the temperatures are measured during the GHB test using thermocouples. The overall temperature uncertainty is therefore made up of the uncertainty due to the thermocouple material, the cold junction compensation sensor, and the Agilent DAQ reading of the thermocouple and cold junction compensation.

The thermocouple material is determined from the manufacturer specification of the thermocouple. The thermocouple type used in the GHB was the Omega Special Limits of Error (SLE) 24-gauge type T Class 1 thermocouples. The manufacturer quoted thermocouple accuracy is ±0.5°C (OMEGA Engineering inc., 2017). This accuracy is assumed to be the 95% confidence interval (2σ) based on the material composition of the

thermocouple, and its accuracy in relation to the IT90 calibration curve for a T type thermocouple (Nicholas & White, 1994).

The thermocouples are measured using an Agilent 34970a data acquisition unit. The range accuracy and reading accuracy for this digital multimeter are ±0.004% and ±0.005% respectively for the 100mV range. The range accuracy is the accuracy of the unit over the full range, in this case 100mV. The reading accuracy is the accuracy of the unit for the given sensor reading. The range and reading results are added to determine the total uncertainty for a given reading. The uncertainty on the combined range and reading accuracy for the thermocouples was determined by using the maximum uncertainty for a T-type thermocouple in the range of -50°C to +50°C (Nicholas & White, 1994). The values used to determine this uncertainty are presented in Table 35.

**Table 35: Combined range and reading uncertainty of Agilent DAQ.**

| T [°C] | Expected reading for IT90 Type T [µV] | Agilent DAQ uncertainty [µV} |
|---|---|---|
| -50 | -1819 | 4.091 |
| -25 | -940 | 4.047 |
| 0 | 0 | 4.000 |
| 25 | 992 | 4.050 |
| 50 | 2036 | 4.102 |
| µV/°C | 38.568 | 4.058 |
| **Uncertainty (± °C)** | | **0.105** |

In this temperature range, the T-type thermocouple is expected to have a calibration slope of 38.6 µV/°C. The values used to determine this slope were transcribed from the IT90 T type thermocouple chart (Nicholas & White, 1994). Combining these results in a total

uncertainty for the DAQ on a thermocouple reading of ±0.11°C. This uncertainty is used for both exterior temperatures of -20°C and -35°C.

## E.2 Cold junction compensation uncertainty

The thermocouple measurement method also requires comparison with a cold junction reference temperature. The cold junction reference in the GHB consists of an aluminum block in lab conditions maintained at 23±2°C. The aluminum block temperature is measured with an Omega Class A RTD (100 Ω), with an uncertainty of ±0.20°C. The expected readings were transcribed from the Omega RTD documentation. The values used to calculate this uncertainty are presented in Table 36.

**Table 36: Cold junction compensation RTD uncertainty**

| T [°C] | Expected resistance reading [Ω] | Uncertainty [°C] |
|---|---|---|
| **25** | 109.73 | 0.2 |
| **24** | 109.35 | 0.198 |
| **23** | 108.96 | 0.196 |
| **22** | 108.57 | 0.194 |
| **21** | 108.18 | 0.192 |
| **Average uncertainty [°C]** | | **0.196** |

The same Agilent DAQ is used for the cold junction RTD measurement. For the temperatures investigated the Agilent range and reading accuracy are ±0.01% and ±0.004% respectively. The Agilent DAQ adds an additional uncertainty of ±0.011Ω on the RTD reading. This corresponds to an additional uncertainty of ±0.04°C in the temperature range of 21°C to 25°C for the RTD used. The values used to determine the uncertainty for the Agilent DAQ on the RTD are shown in Table 37.

**Table 37: Cold junction compensation uncertainty**

| RTD reading [Ω/°C] | Agilent DAQ uncertainty [Ω] | Agilent DAQ uncertainty [°C] |
|---|---|---|
| **0.38** | 0.0144 | 0.0379 |
| **0.39** | 0.0144 | 0.0369 |
| **0.39** | 0.0144 | 0.0368 |
| **0.39** | 0.0143 | 0.0368 |
| **0.39** | 0.0143 | 0.0367 |
| **Agilent RTD reading average uncertainty (+/- °C)** | | **0.0370** |

The thermocouple material, DAQ, and cold junction uncertainties are combined in as a RSS to give an overall thermocouple uncertainty of ±0.55°C.

## E.3 Metering box heater uncertainty

The GHB monitors the heat input to the metering box by measuring the current supplied to and voltage dissipation of a DC heater. The current is determined by measuring the voltage dissipation across a calibrated resistor in series with the DC heater. The voltage dissipation of the DC heater is directly measured across the heater.

The voltage dissipation across the calibrated resistor is measured using the same Agilent DAQ as the thermocouples. The calibrated resistor is a 0.5Ω resistor, with an accuracy of 0.05%. The heater is provided power from a Kenwood PD56-10 power supply, which supplies a maximum of 10A and 56 V to the heater. The voltage dissipation across the heater is also measured using the Agilent DAQ. The total power (energy input) provided

by the heater to the calorimeter is determined by multiplying the current and voltage across the heater.

The range and reading uncertainty of the Agilent DAQ for the 10A of the power supply is ±0.0045% and ±0.0006%. This corresponds to an uncertainty of ±0.004836V.

The range and reading uncertainty of the Agilent DAQ for the 10A of the power supply is ±0.0035% and ±0.0005%. This corresponds to an uncertainty of ±0.000375A.

Combining these uncertainties results in an uncertainty on the total power measurement of ±0.0124%. Applying this uncertainty to the heat input to the metering box during the VIP wall tests, results in the uncertainties at each exterior temperature in Table 38.

**Table 38: Metering box heater uncertainty**

| Exterior temperature [°C] | Uncertainty [±W] |
|---|---|
| **-20°C** | 0.0084 |
| **-35°C** | 0.0069 |

## E.4 Combined metering box and flanking loss

As described previously, the combined metering box and flanking losses are determined through measuring the voltage generation of a thermopile wired between the metering box walls, and comparing the GHB results with the expected calibrated specimen results. The combined metering box and flanking loss is made up of two components, the slope and the offset. The uncertainty of the slope is determined from the uncertainty of the thermopile measurement. The uncertainty of the offset value is determined by comparing the thermal resistance of a calibrated specimen determined with the guarded hot box when the thermopile reads zero with the thermal resistance results for the same specimen in a heat flow meter apparatus. The uncertainty of this characterization is the combined uncertainty

of the thermocouples on each surface of the specimen, the DAQ measurement of the thermopile voltage, the heater uncertainty, and the calibrated specimen uncertainty. The thermocouple and heater uncertainty have been defined in the previous sections.

**Thermopile slope uncertainty:**

The thermopile to watts calibration has uncertainty due to the DAQ measurement of the thermopile voltage, the heater measurement uncertainty, and the uncertainty of the calibrated specimen results. From the thermocouple uncertainty analysis, the DAQ unit uncertainty in the millivolt range is ±4.1μV, which results in an uncertainty of ±0.007W for both -20°C and -35°C exterior temperatures.

**Offset uncertainty due to calibrated specimen:**

The calibrated specimen uncertainty is the uncertainty of the ASTM C518 heat flow meter apparatus, as well as the thermocouples and area measurement of the specimen in the guarded hot box. The uncertainty in the thermal resistance of the calibrated specimen determined with the heat flow meter apparatus used is ±2% (Lackey, Normandin, Marchand, & Kumaraman, 1994). The previously determined thermocouple uncertainty is 0.55°C. The uncertainty due to the area measurement is estimated to be ±0.0001 $m^2$ (±0.01m in each direction).

The overall uncertainty is determined as the uncertainty in the calculation of heat transfer expected to be measured in the GHB for the calibrated specimen with the

uncertainties of each component added in. The equation used to determine the expected heat transfer in the guarded hot box is given in Equation 18.

$$Q_{GHB} = \frac{\left(A * \left(T_{s,h} - T_{s,c}\right)\right)}{R_{cal}} \qquad \textbf{Equation 18}$$

The as measured values and their respective uncertainties for each component listed in Equation 18 are presented in Table 39. The expected heat transfer in the guarded hot box is determined from Equation 18 using the parameters not including any uncertainty and then a separate calculation is made to determine $Q_{GHB}$ by individually perturbing each variable to its maximum value including the uncertainty, as described in Moffat (Moffat, 1988). The values and results for Equation 18 for an exterior temperature of -20°C and -35°C are presented in Table 40 and Table 41, respectively. The results of the differences between each perturbed result and the average and the RSS uncertainty for the calibrated specimen for each exterior temperature are presented in Table 42.

**Table 39: Calibrated specimen uncertainty parameters**

| | Average | | Uncertainty (±) | Perturbed value | |
|---|---|---|---|---|---|
| | -20°C | -35°C | | -20°C | -35°C |
| $T_{s,c}$ | -19.81 | -34.56 | 0.55 | -20.36 | -35.11 |
| $T_{s,h}$ | 19.25 | 18.96 | 0.55 | 19.80 | 19.51 |
| $R_{cal}$ | 3.55 | 3.65 | 7.11E-02 | 3.62 | 3.72 |
| $A$ | 5.95 | 5.95 | 1.00E-04 | 5.95 | 5.95 |

**Table 40: Calibrated specimen results for Equation 18 -20°C**

| | Label | $R_{cal}$ | $A$ | $T_{s,c}$ | $T_{s,h}$ | $Q_{GHB}$ |
|---|---|---|---|---|---|---|
| Average values | 1 | 3.55 | 5.95 | -19.81 | 19.25 | 65.45 |
| $R_{cal}$ perturbed | 2 | 3.62 | 5.95 | -19.81 | 19.25 | 64.17 |
| $A$ perturbed | 3 | 3.55 | 5.95 | -19.81 | 19.25 | 65.45 |
| $T_{s,c}$ perturbed | 4 | 3.55 | 5.95 | -20.36 | 19.25 | 66.37 |
| $T_{s,h}$ perturbed | 5 | 3.55 | 5.95 | -19.81 | 19.80 | 66.37 |

**Table 41: Calibrated specimen results for Equation 18 -35°C**

| | Label | $R_{cal}$ | $A$ | $T_{s,c}$ | $T_{s,h}$ | $Q_{GHB}$ |
|---|---|---|---|---|---|---|
| **Average values** | 1 | 3.65 | 5.95 | -34.56 | 18.96 | 87.40 |
| **$R_{cal}$ perturbed** | 2 | 3.72 | 5.95 | -34.56 | 18.96 | 85.68 |
| **$A$ perturbed** | 3 | 3.65 | 5.95 | -34.56 | 18.96 | 87.40 |
| **$T_{s,c}$ perturbed** | 4 | 3.65 | 5.95 | -35.11 | 18.96 | 88.29 |
| **$T_{s,h}$ perturbed** | 5 | 3.65 | 5.95 | -34.56 | 19.51 | 88.29 |

**Table 42: Calibrated specimen uncertainty calculation**

| Difference | -20°C | -35°C |
|---|---|---|
| **2-1** | -1.28 | -1.71 |
| **3-1** | 0.00 | 0.00 |
| **4-1** | 0.92 | 0.90 |
| **5-1** | 0.92 | 0.90 |
| **RSS uncertainty [±W]** | 1.67 | 2.27 |

Following the same procedure, the uncertainty of the offset can be determined by perturbing the values in Equation 19. The uncertainty is then determined by taking the RSS of the results. The calculations for each perturbed value are presented in Table 43 and Table 44, for the -20°C and -35°C exterior temperatures respectively. The RSS uncertainty for the offset at each exterior temperature is shown in Table 45.

$$Q_{\text{offset}} = Q_{\text{t}} - Q_{\text{MB}} - Q_{\text{s}} \qquad \textbf{Equation 19}$$

**Table 43: Calibrated specimen results for Equation 19 -20°C**

| | Label | $Q_{\text{t}}$ | $Q_{\text{MB}}$ | $Q_{\text{s}}$ | $Q_{\text{offset}}$ |
|---|---|---|---|---|---|
| **Average values** | 1 | 67.69 | 0.63 | 65.45 | 1.61 |
| **$Q_{\text{t}}$ perturbed** | 2 | 67.70 | 0.63 | 65.45 | 1.62 |
| **$Q_{\text{MB}}$ perturbed** | 3 | 67.69 | 0.64 | 65.45 | 1.60 |
| **$Q_{\text{s}}$ perturbed** | 4 | 67.69 | 0.63 | 67.12 | -0.05 |

**Table 44: Calibrated specimen results for Equation 19 -35°C**

| | Label | $Q_t$ | $Q_{MB}$ | $Q_s$ | $Q_{offset}$ |
|---|---|---|---|---|---|
| **Average values** | 1 | 93.92 | 2.34 | 87.40 | 4.18 |
| **$Q_t$ perturbed** | 2 | 93.93 | 2.34 | 87.40 | 4.19 |
| **$Q_{MB}$ perturbed** | 3 | 93.92 | 2.36 | 87.40 | 4.17 |
| **$Q_s$ perturbed** | 4 | 93.92 | 2.34 | 89.06 | 2.51 |

**Table 45: Offset uncertainty calculation**

| Difference | -20°C | -35°C |
|---|---|---|
| **2-1** | 0.01 | 0.01 |
| **3-1** | -0.02 | -0.02 |
| **4-1** | -1.67 | -1.67 |
| **RSS uncertainty [±W]** | 1.39 | 1.39 |

The combined metering box and flanking loss uncertainty is ±1.39 W for both exterior temperature tests.

## E.5 Thermal resistance calculation uncertainty

The thermal resistance uncertainty calculation is completed using Equation 13 and perturbing each parameter with its uncertainty following the same procedure outlined previously. The calculations for each perturbed value are presented in Table 46 and Table 47, for the -20°C and the -35°C exterior temperatures respectively. The uncertainty on the calculated RSI from the GHB experiments conducted in this thesis are ±4.5% and ±3.3% for exterior temperatures of -20°C and -35°C respectively. The calculation values are presented in Table 48.

**Table 46: Thermal resistance results for Equation 13 -20°C**

| | Label | $A$ | $T_{amb,h}$ | $T_{amb,c}$ | $Q_t$ | $Q_{MB} + Q_{fl}$ | $R$ |
|---|---|---|---|---|---|---|---|
| **Average values** | 1 | 5.95 | 20.83 | -20.08 | 40.05 | -4.58 | 6.86 |
| **$A$ perturbed** | 2 | 5.95 | 20.83 | -20.08 | 40.05 | -4.58 | 6.86 |
| **$T_{s,h}$ perturbed** | 3 | 5.95 | 21.37 | -20.08 | 40.05 | -4.58 | 6.95 |
| **$T_{s,c}$ perturbed** | 4 | 5.95 | 20.83 | -20.63 | 40.05 | -4.58 | 6.95 |
| **$Q_t$ perturbed** | 5 | 5.95 | 20.83 | -20.08 | 40.06 | -4.58 | 6.86 |
| **$Q_{MB} + Q_{fl}$ perturbed** | 6 | 5.95 | 20.83 | -20.08 | 40.05 | -5.98 | 7.14 |

**Table 47: Thermal resistance results for Equation 13-35°C**

| | Label | $A$ | $T_{amb,h}$ | $T_{amb,c}$ | $Q_t$ | $Q_{MB} + Q_{fl}$ | $R$ |
|---|---|---|---|---|---|---|---|
| **Average values** | 1 | 5.95 | 20.88 | -34.87 | 55.33 | 6.89 | 6.84 |
| **$A$ perturbed** | 2 | 5.95 | 20.88 | -34.87 | 55.33 | 6.89 | 6.84 |
| **$T_{s,h}$ perturbed** | 3 | 5.95 | 21.43 | -34.87 | 55.33 | 6.89 | 6.91 |
| **$T_{s,c}$ perturbed** | 4 | 5.95 | 20.88 | -35.42 | 55.33 | 6.89 | 6.91 |
| **$Q_t$ perturbed** | 5 | 5.95 | 20.88 | -34.87 | 55.34 | 6.89 | 6.84 |
| **$Q_{MB} + Q_{fl}$ perturbed** | 6 | 5.95 | 20.88 | -34.87 | 55.33 | 8.28 | 7.05 |

**Table 48: Thermal resistance uncertainty**

| Difference | -20°C | -35°C |
|---|---|---|
| **2-1** | 0.00 | 0.00 |
| **3-1** | 0.09 | 0.07 |
| **4-1** | 0.09 | 0.07 |
| **5-1** | 0.00 | 0.00 |
| **6-1** | 0.28 | 0.20 |
| **RSS uncertainty [±W]** | 4.5% | 3.27% |

Appendix F **Parallel path method**

This appendix presents the values used to calculate the overall thermal resistance of the wall assembly using the parallel path method for each VIP thermal conductivity scenario investigated. As discussed, the parallel path method consists of dividing the frontal area of the wall into divisions based on differences in the substructure geometry. For the wall assembly investigated three divisions were used to determine the thermal resistance using the parallel path method. The parallel path calculation results for each division described in Figure 7 for the 004 w_air VIP thermal conductivity are presented as an example in Table 49 and Table 50. For the parallel path method, the only variable that changes between scenarios is the VIP thermal conductivity. The remaining calculation results for each section with the various VIP thermal conductivity scenarios are presented in Table 51.

**Table 49: Parallel path section breakdown**

| Section pp1 | RSI [$m^2K/W$] |
|---|---|
| XPS (2in) | 1.75E+00 |
| VIP (25mm) | 5.95E+00 |
| XPS (0.5in) | 5.26E-01 |
| Air space | 1.54E-01 |
| Mineral fibre (3.625 in) | 2.47E+00 |
| Gypsum (5/8 in) | 9.92E-02 |

| Section pp2 | RSI [$m^2K/W$] |
|---|---|
| XPS (2in) | 1.75E+00 |
| VIP (25mm) | 5.95E+00 |
| XPS (0.5in) | 5.26E-01 |
| Steel stud (0.0179in) | 9.47E-06 |
| Air space | 1.54E-01 |
| Mineral fibre (3.625in) | 2.47E+00 |
| Steel stud (0.0179in) | 9.47E-06 |
| Gypsum (5/8 in) | 9.92E-02 |

| Section pp3 | RSI [$m^2K/W$] |
|---|---|
| XPS (2in) | 1.91E-01 |
| VIP (25mm) | 5.95E+00 |
| XPS (0.5in) | 5.26E-01 |
| Steel stud | 1.92E-03 |
| Gypsum (5/8 in) | 9.92E-02 |

**Table 50: RSI total for each section**

| | pp1 | pp2 | pp3 | 004 w_air parallel path RSI |
|---|---|---|---|---|
| **RSI section total** | 11.0 | 11.0 | 6.8 | 11.0 |
| **Section area (m2)** | 5.24 | 0.70 | 0.01 | |
| **Area % of total** | 88.1% | 11.7% | 0.2% | |

**Table 51: Parallel path results for each VIP thermal conductivity scenario**

| VIP thermal conductivity | Section RSI [$m^2K/W$] | | | Total RSI [$m^2K/W$] |
|---|---|---|---|---|
| | pp1 | pp2 | pp3 | |
| **004 w_air** | 11.0 | 11.0 | 6.8 | 11.0 |
| **Manufacturer max** | 9.7 | 9.7 | 5.5 | 9.7 |
| **Lorenzati min** | 9.7 | 9.7 | 5.5 | 9.7 |
| **Lorenzati average** | 9.3 | 9.3 | 5.1 | 9.3 |
| **Lorenzati max** | 8.5 | 8.5 | 4.3 | 8.5 |
| **90 nm** | 9.9 | 9.9 | 5.8 | 9.9 |
| **300 nm** | 9.7 | 9.7 | 5.5 | 9.7 |

## Appendix G **Isothermal planes method**

The isothermal planes calculation method consists of dividing the wall into isothermal planes perpendicular to the interior to exterior temperature gradient. This method again uses the analogous electrical circuit, but this time divides the wall into sections which make use of the summation of resistors in parallel (Incopera, 2006) for each layer. The layers are solved first to determine the overall thermal resistance for each plane, then the planes are summated as resistors in series to determine the overall wall thermal resistance. Figure 8 depicts the isothermal planes method plane divisions for the wall assembly evaluated in this thesis. The parameters used to solve each plane thermal resistance and thereafter the total thermal resistance with the isothermal planes method are presented in Table 52 and Table 53. The tables are an example of the calculation method using the 004 w_air VIP thermal conductivity. For the isothermal planes calculation method, the only parameter which changes between scenarios is the VIP thermal conductivity. The outcomes of each plane and the total thermal resistance for each scenario are given in Table 54.

**Table 52: 004 w_air isothermal planes calculation example**

| Plane divisions | Material | Material RSI | Corresponding area % of plane | Total RSI per plane |
|---|---|---|---|---|
| **Plane 1** | **XPS (2in)** | 1.75E+00 | 100% | 1.75E+00 |
| **Plane 2** | **VIP (20mm)** | 5.95E+00 | 100% | 5.95E+00 |
| **Plane 3** | **XPS (0.6in)** | 5.26E-01 | 100% | 5.26E-01 |
| **Plane 4** | **Steel stud** | 9.47E-06 | 12% | 2.31E+00 |
| | **Air space** | 1.51E-01 | 88% | |
| | **Mineral fibre** | 2.47E+00 | 88% | |
| **Plane 5** | **Gypsum** | 9.92E-02 | 100% | 9.92E-02 |

**Table 53: 004 w_air RSI using the isothermal planes method**

| | 004 w_air [$m^2K/W$] |
|---|---|
| **Combined RSI** | 10.6 |

**Table 54: Results for each plane and total RSI for each VIP thermal conductivity scenario**

| VIP thermal conductivity | RSI total in each plane | | | | | Total RSI |
|---|---|---|---|---|---|---|
| | Plane 1 | Plane 2 | Plane 3 | Plane 4 | Plane 5 | |
| **004 w_air** | 1.8 | 6.0 | 0.5 | 2.3 | 0.1 | 10.6 |
| **Manufacturer max** | 1.8 | 4.7 | 0.5 | 2.3 | 0.1 | 9.4 |
| **Lorenzati min** | 1.8 | 4.7 | 0.5 | 2.3 | 0.1 | 9.4 |
| **Lorenzati average** | 1.8 | 4.3 | 0.5 | 2.3 | 0.1 | 9.0 |
| **Lorenzati max** | 1.8 | 3.5 | 0.5 | 2.3 | 0.1 | 8.1 |
| **90nm** | 1.8 | 4.9 | 0.5 | 2.3 | 0.1 | 9.6 |
| **300nm** | 1.8 | 4.7 | 0.5 | 2.3 | 0.1 | 9.4 |

Appendix H **Modified zone method**

This appendix presents that calculations in detail for the modified zone method of calculating thermal resistance in wall assemblies containing steel studs. This calculation method determines a thermally effected zone caused by the steel stud, which is larger than its nominal area. The modified zone method consists of determining the zone factor, from a chart correlation, and thereafter using that zone factor to calculate the additional area over which the steel stud effects the results. The zone factor is determined using the ratio of the thermal resistance of the first 25mm of sheathing exterior to the stud to the cavity insulation thermal resistance. Since the VIP is within the exterior 25mm of the steel stud, the thermally effected zone results differ for each VIP thermal conductivity scenario. As an example, the results of each step of the calculation method, as well as the final result for the 004 w_air VIP thermal conductivity are shown in Table 56 to Table 59. Results for the thermally effected zone width, and the overall thermal resistance for all other VIP thermal conductivity scenarios are shown in Table 60. The modified zone calculation steps listed below follow those outlined in Chapter 27 of ASHRAE Fundamentals (ASHRAE, 2013).

**Step 1:** Determine the zone factor ($z_f$) the zone factor is determined from Figure 9 and the ratio of the thermal resistivity ($1/\lambda$) of the sheathing materials to the thermal resistivity of the cavity insulation. The values used to determine the zone factor in this example are given in Table 55.

**Table 55: Zone factor**

| | Materials | Total thermal resistivity of materials (mK/W) |
|---|---|---|
| Thermal resistivity of sheathing ($r_A$) | XPS (12.5 mm) | 59.5 |
| | VIP (12.5mm) | |
| Cavity insulation ($r_{ins}$) | Mineral fibre | 27.8 |
| Ratio | | 2.1 |
| Zone factor ($z_f$), from curve fit of Figure 9 | | 1.9 |

**Step 2:** Calculate the width of the thermally effected zone ($W$, Equation 10). The values used to calculate the thermally effected zone width are given in Table 56.

**Table 56: Thermally effected zone width ($W$) calculation**

| | |
|---|---|
| Thickness of exterior insulating materials ($d_i$) | 8.75E-02 |
| Flange length ($L$) | 3.18E-02 |
| Thermally effected zone width ($W$) | 2.01E-01 |

**Step 3:** Calculate the thermal resistance of the sheathing materials (external) and the interior sheathing board (internal). The values used in this example are shown in Table 57.

**Table 57: Internal and external thermal resistance**

| | Components | R [m²K/W] | Combined R [m²K/W] |
|---|---|---|---|
| Exterior sheathing ($R_A$) | XPS (12.5 mm) | 0.43 | 8.1 |
| | VIP (25mm) | 5.95 | |
| | XPS (50 mm) | 1.75 | |
| Interior sheathing ($R_B$) | Gypsum (15.9 mm) | 0.10 | 0.1 |

**Step 4:** Calculate the thermal resistance of sections in the zone around the steel stud. The section includes both the steel stud, and a section to each side which is the cavity insulation. The section is divided such that there is a series of parallel heat transfer points, first through the cavity insulation and stud flange, then the cavity insulation and the stud

depth and finally again through the stud flange and cavity insulation. This is well illustrated in Chapter 27 of the ASHRAE Handbook of Fundamentals (ASHRAE, 2013). Calculating the combined thermal resistance of this section requires the thermal resistance of the stud flange, the stud web depth, the cavity insulation at the stud flange, and the cavity insulation along the stud depth. A schematic depicting the division for the heat transfer path through the thermally effect zone and the centre of the stud cavity is shown in Figure 86, the labels are consistent with those from Chapter 27 of the ASHRAE Handbook of Fundamentals (ASHRAE, 2013). The parameters used to solve the thermal resistance circuit for the 004 w_air are shown in Table 58.

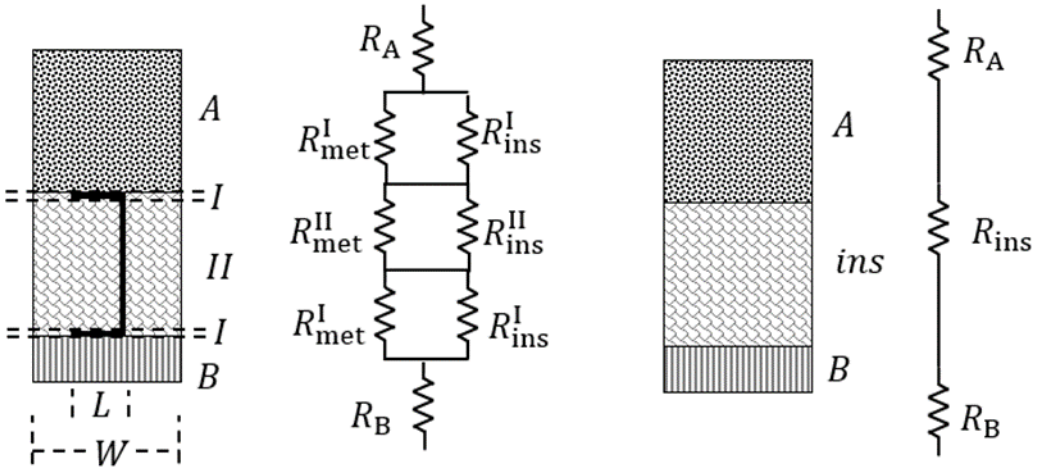


**Figure 86: Thermal resistance diagram for modified zone calculation method.**

**Table 58: Parameters for modified zone calculation method, from Figure 86**

| Parameter | Description | R [m²K/W] |
|---|---|---|
| $d_{II}$ | Depth of section II | 9.12E-02 |
| $d_I$ | Depth of section I | 4.55E-04 |
| $R^I_{ins}$ | Thermal resistance of insulation in section I | 2.53E+00 |
| $R^I_{met}$ | Thermal resistance of steel stud in section I | 1.90E-03 |
| $R^{II}_{ins}$ | Thermal resistance of insulation in section II | 2.53E-02 |
| $R^{II}_{met}$ | Thermal resistance of steel stud in section II | 1.89E-05 |

In zone $W$, the combined thermal resistance for section I and section II are determined with Equation **20** and Equation 21. The values for the resistances in the 004_w air example are shown in Table 59.

$$R_{\mathrm{I}} = \frac{R_{\mathrm{met}}^{\mathrm{I}} R_{\mathrm{ins}}^{\mathrm{I}} W}{d_{\mathrm{I}}(R_{\mathrm{ins}}^{\mathrm{I}} - R_{\mathrm{met}}^{\mathrm{I}}) + W R_{\mathrm{met}}^{\mathrm{I}}} \qquad \textbf{Equation 20}$$

$$R_{\mathrm{II}} = \frac{R_{\mathrm{met}}^{\mathrm{II}} R_{\mathrm{ins}}^{\mathrm{II}} W}{L(R_{\mathrm{ins}}^{\mathrm{II}} - R_{\mathrm{met}}^{\mathrm{II}}) + W R_{\mathrm{met}}^{\mathrm{II}}} \qquad \textbf{Equation 21}$$

**Step 5:** Determine the combined thermal resistance for each section and then the total thermal resistance of the wall assembly. The combined thermal resistance for the centre of cavity ($R_{\mathrm{cav}}$) and zone $W$ ($R_{\mathrm{W}}$) are determined by summing the resistances in each section, and are given in Equation **22** and Equation **23**. The total thermal resistance of the wall assembly is then calculated with Equation **24**. The resulting parameters for each equation are shown in Table 59.

$$\sum R_{\mathrm{cav}} = R_{\mathrm{A}} + R_{\mathrm{B}} + R_{\mathrm{ins}} \qquad \textbf{Equation 22}$$

$$\sum R_{\mathrm{W}} = R_{\mathrm{A}} + R_{\mathrm{B}} + R_{\mathrm{I}} + 2R_{\mathrm{II}} \qquad \textbf{Equation 23}$$

$$R_t = \frac{\sum R_{\mathrm{W}} \sum R_{\mathrm{cav}}\, s}{W(\sum R_{\mathrm{cav}} - \sum R_{\mathrm{W}}) + s \sum R_{\mathrm{W}}} \qquad \textbf{Equation 24}$$

**Table 59: Combined thermal resistances for each zone and total thermal resistance using modified zone calculation method.**

| Parameter | R [m²K/W] |
|---|---|
| $R_{I}$ | 4.19E-03 |
| $R_{II}$ | 1.20E-04 |
| $\sum R_{cav}$ | 1.08E+01 |
| $\sum R_{W}$ | 8.21E+00 |
| $R_{t}$ | 9.33E+00 |

Due to each VIP scenario having a different VIP thermal conductivity, the zone factor and zone width correspondingly change for each scenario due to changes in the combined exterior sheathing thermal resistance. This in turn changes the combined cavity and combined zone w thermal resistances, and therefore changes the total thermal resistance as well. The values for each of these parameters for all the VIP scenarios are shown in Table 60.

**Table 60: Parameters for modified zone calculations for each VIP thermal conductivity scenario.**

| VIP thermal conductivity scenario | $r_{A}$ | $r_{ins}$ | $\frac{r_{A}}{r_{ins}}$ | $z_{f}$ | $W$ | $\sum R_{cav}$ | $\sum R_{W}$ | $R_{t}$ |
|---|---|---|---|---|---|---|---|---|
| 004 w_air | 59.5 | 27.8 | 2.1 | 1.9 | 0.2 | 10.8 | 8.2 | 9.3 |
| Manufacturer max | 57.7 | 27.8 | 2.1 | 1.9 | 0.2 | 9.53 | 7.0 | 8.1 |
| Lorenzati min | 57.7 | 27.8 | 2.1 | 1.9 | 0.2 | 9.5 | 7.0 | 8.1 |
| Lorenzati average | 56.8 | 27.8 | 2.0 | 1.9 | 0.2 | 9.1 | 6.5 | 7.6 |
| Lorenzati max | 54.7 | 27.8 | 2.0 | 1.9 | 0.2 | 8.3 | 5.7 | 6.8 |
| 90nm | 58.1 | 27.8 | 2.1 | 1.9 | 0.2 | 9.7 | 7.2 | 8.3 |
| 300nm | 57.6 | 27.8 | 2.1 | 1.9 | 0.2 | 9.5 | 6.9 | 8.0 |

Appendix I **BRE 465 method**

The BRE 465 method uses the ratio between the results of the isothermal planes and parallel path calculation methods. The ratio between the two values is determined via a weighting factor ($p$), which is dependent on the steel stud details, as given in Equation 12. Since the weighting factor is geometry dependent, it is constant throughout all VIP thermal conductivity scenarios. The values used to calculate the weighting factor for the wall assembly investigated, and the weighting factor value, are given in Table 61.

The weighting factor is then used with the parallel path ($\boldsymbol{R_{max}}$) and isothermal planes ($\boldsymbol{R_{min}}$) result for each VIP thermal conductivity scenario to calculate the thermal resistance using Equation 11.

**Table 61: BRE 465 calculation method**

| Parameter (Equation 11) | Value |
|---|---|
| Stud spacing ($s$) [mm] | 406.4 |
| Stud depth ($d$) [mm] | 92.075 |
| Flange width ($w$) [mm] | 31.75 |
| p | 0.81 |
| $\frac{\boldsymbol{R_{min}}}{\boldsymbol{R_{max}}}$ | 0.97 |
| BRE 465 R [m$^2$K/W] | 10.9 |

## Appendix J **COMSOL settings for two-dimensional simulations**

This appendix presents the parameter and geometry settings for the 2D simulations conducted in COMSOL. The list of parameters used are presented and described in Table 62. The geometry specifications for each component are described in Table 63, and a schematic of the parameters list and geometry in COMSOL is presented in Figure 87.The geometry is by entering the x and y coordinates in COMSOL.

**Table 62: Parameters list for COMSOL simulations.**

| Parameter label | Parameter value | Parameter description |
|---|---|---|
| N | 0.001[in] | stud scaling parameter |
| A | 17.9*N | stud gauge |
| B | 0.25[in] | flange length |
| C | 1.25[in] | stud contact area |
| D | 3.625[in] | stud depth |
| ho_20 | 60.76[W/(m^2 *K)] | exterior heat flux for -20 calibration |
| hi_20 | 8.93[W/(m^2* K)] | interior heat flux for -20 calibration |
| ho_35 | 50.42[W/(m^2 *K)] | exterior heat flux for -35 calibration |
| hi_35 | 7.46[W/(m^2* K)] | interior heat flux for -35 calibration |
| Ti_20 | 20.79[degC] | interior temperature -20 experiment |
| Text_20 | -20.08[degC] | exterior temperature in -20 experiment |
| Ti_35 | 20.88[degC] | interior temperature -35 experiment |
| Text_35 | -34.87[degC] | exterior temperature in -35 experiment |
| hi | hi_35, Hi_20 | interior heat flux for simulation (_20 for -20 simulations, _35 for -35 simulations) |
| hext | ho_35, ho_20 | Exterior heat flux for simulation (_20 for -20 simulations, _35 for -35 simulations) |
| Ti | Ti_35, Ti_20 | interior air temperature used in simulations (_20 for -20 simulations, _35 for -35 simulations) |
| Text | Text_35, Text_20 | exterior air temperature used in simulations (_20 for -20 simulations, _35 for -35 simulations) |
| G | 7.20[mm] | air gap width between panels |

**Table 63:Two-dimensional geometry for COMSOL simulations.**

| | | x coordinate | y coordinate |
|---|---|---|---|
| **Gypsum panel** | | 0 | 0 |
| **Mineral fibre** | | 0 | 0.625[in] |
| **Cavity air space** | | 0 | 0.625[in]+89[mm] |
| **XPS interior** | | 0 | 0.625[in]+D |
| **XPS exterior** | | 0 | 0.625[in]+D+0.5[in]+25[mm] |
| **VIP** | | G/2 | 0.625[in]+D+0.5[in] |
| **VIP air gap** | | 1200[mm]+G/2 | 0.625[in]+D+0.5[in] |
| **VIP 1** | | 1200[mm]+G+G/2 | 0.625[in]+D+0.5[in] |
| **Air gap end** | | 0 | 0.625[in]+D+0.5[in] |
| **Steel stud vertical** | **1** | 0.625[in] | 0.625[in] |
| | **2** | 16[in]-A | 0.625[in] |
| | **3** | 32[in]-A | 0.625[in] |
| | **4** | 48[in]-A | 0.625[in] |
| | **5** | 64[in]-A | 0.625[in] |
| | **6** | 80[in]-A | 0.625[in] |
| | **7** | 96[in]-A | 0.625[in] |
| **Steel Stud bottom** | **1** | 0 | 0.625[in] |
| | **2** | 16[in]-C | 0.625[in] |
| | **3** | 32[in]-C | 0.625[in] |
| | **4** | 48[in]-C | 0.625[in] |
| | **5** | 64[in]-C | 0.625[in] |
| | **6** | 80[in]-C | 0.625[in] |
| | **7** | 96[in]-C | 0.625[in] |
| **Steel stud top** | **1** | 0 | 0.625[in]+D-A |
| | **2** | 16[in]-C | 0.625[in]+D-A |
| | **3** | 32[in]-C | 0.625[in]+D-A |
| | **4** | 48[in]-C | 0.625[in]+D-A |
| | **5** | 64[in]-C | 0.625[in]+D-A |
| | **6** | 80[in]-C | 0.625[in]+D-A |
| | **7** | 96[in]-C | 0.625[in]+D-A |
| **XPS end cap** | | 95.5[in]-(95.5[in]-1200[mm]-1200[mm]-G-G/2) | 0.625[in]+D |

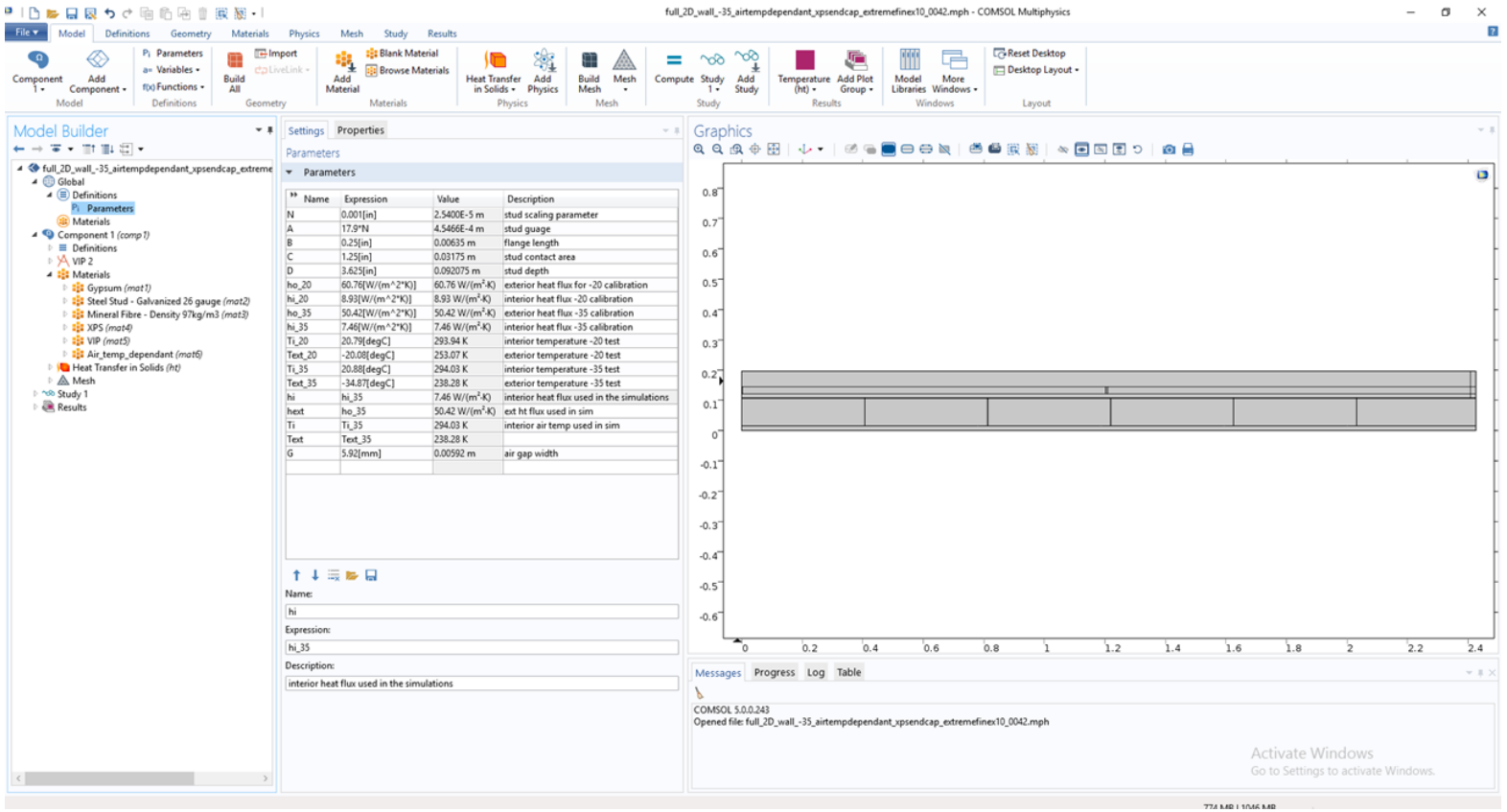


**Figure 87: COMSOL schematic of 2D simulations.**

Appendix K **Correction factors for COMSOL simulations**

This appendix presents the geometry parameters used to develop the correction factors in COMSOL, as well as the correlations for the correction factors derived from the COMSOL simulation results.

## K.1 Correction factor simulations geometry

The location of the material properties, interior and exterior boundary conditions, and the parameters are the same as the previous 2D simulations, except for parameter A, which is now 0.01 (ten times original gauge). The parameters to create the geometry are presented in Table 64. The geometry can be constructed by entering the x and y coordinates into COMSOL. A schematic depicting the geometry in COMSOL is presented in Figure 88.

**Table 64: Geometry details symmetry simulations**

| | Width | Height | x | y |
|---|---|---|---|---|
| **Gypsum** | 16[in] | 0.625[in] | 0 | 0 |
| **Mineral fibre** | 16[in] | 89[mm] | 0 | 0.625[in] |
| **Cavity air space** | 16[in] | D-89[mm] | 0 | 0.625[in]+(89[mm]) |
| **XPS interior** | 16[in] | 0.5[in] | 0 | 0.625[in]+D |
| **XPS Exterior** | 16[in] | 2[in] | 0 | 0.625[in]+D+0.5[in]+25[mm] |
| **VIP** | 8[in]-C/2-G/2 | 25[mm] | 0 | 0.625[in]+D+0.5[in] |
| **VIP air gap** | G | 25[mm] | 8[in]-C/2-G/2 | 0.625[in]+D+0.5[in] |
| **VIP** | 8[in]+G/2+C/2-G | 25[mm] | 8[in]-C/2-G/2+G | 0.625[in]+D+0.5[in] |
| **Steel stud bottom** | C | A | 8[in]-C | 0.625[in] |
| **Steel stud Vertical** | A | D | 8[in]-A | 0.625[in] |
| **Steel stud - top** | C | C | 8[in]-C | 0.625[in]+D-A |

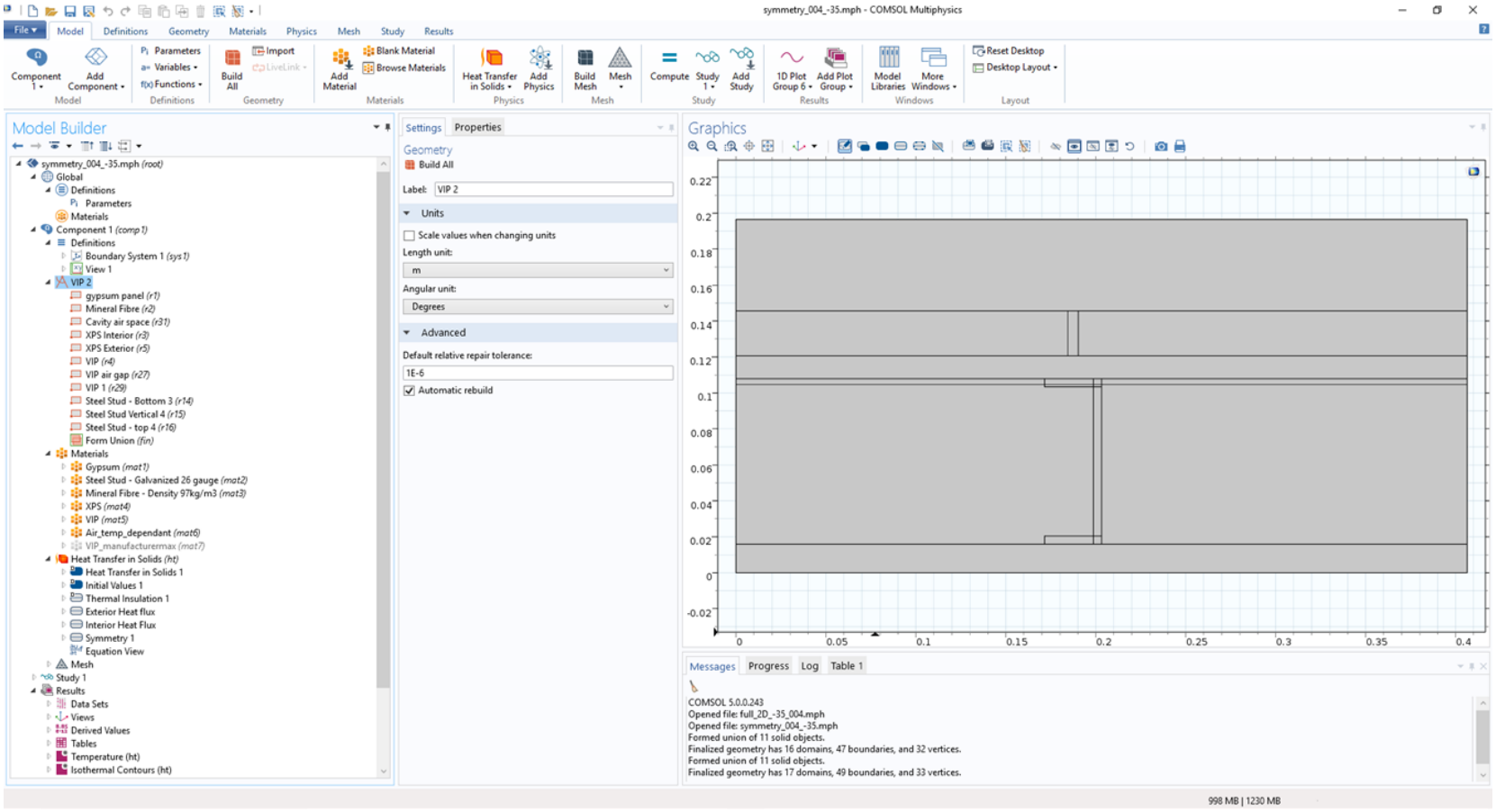


**Figure 88: Geometry for correction factor simulations in COMSOL.**

## K.2 Correction factor correlations

This appendix presents the results of the correction factor correlations for the 3D simulations of the VP wall. The correction factors presented here consist of the correlations used to curve fit the correction factors for the interior sheathing board surface, as well as the temperature through the depth of the mineral fibre.

The correction factors for the interior surface temperature are based directly on the difference in temperature between the sub-assembly results and the average of the full 2D geometry results. The correlations for the correction factors are presented in Figure 89, and Figure 90 for the -20°C and -35°C exterior temperatures respectively.

The correction factors for the temperature through the depth of the mineral fibre were also based directly on the temperature difference between the thermal symmetry with 10x gauge studs and the 2D full plan view simulation results. The correlations for the correction factors are presented in Figure 91, and Figure 92 for the -20°C and -35°C exterior temperatures respectively.

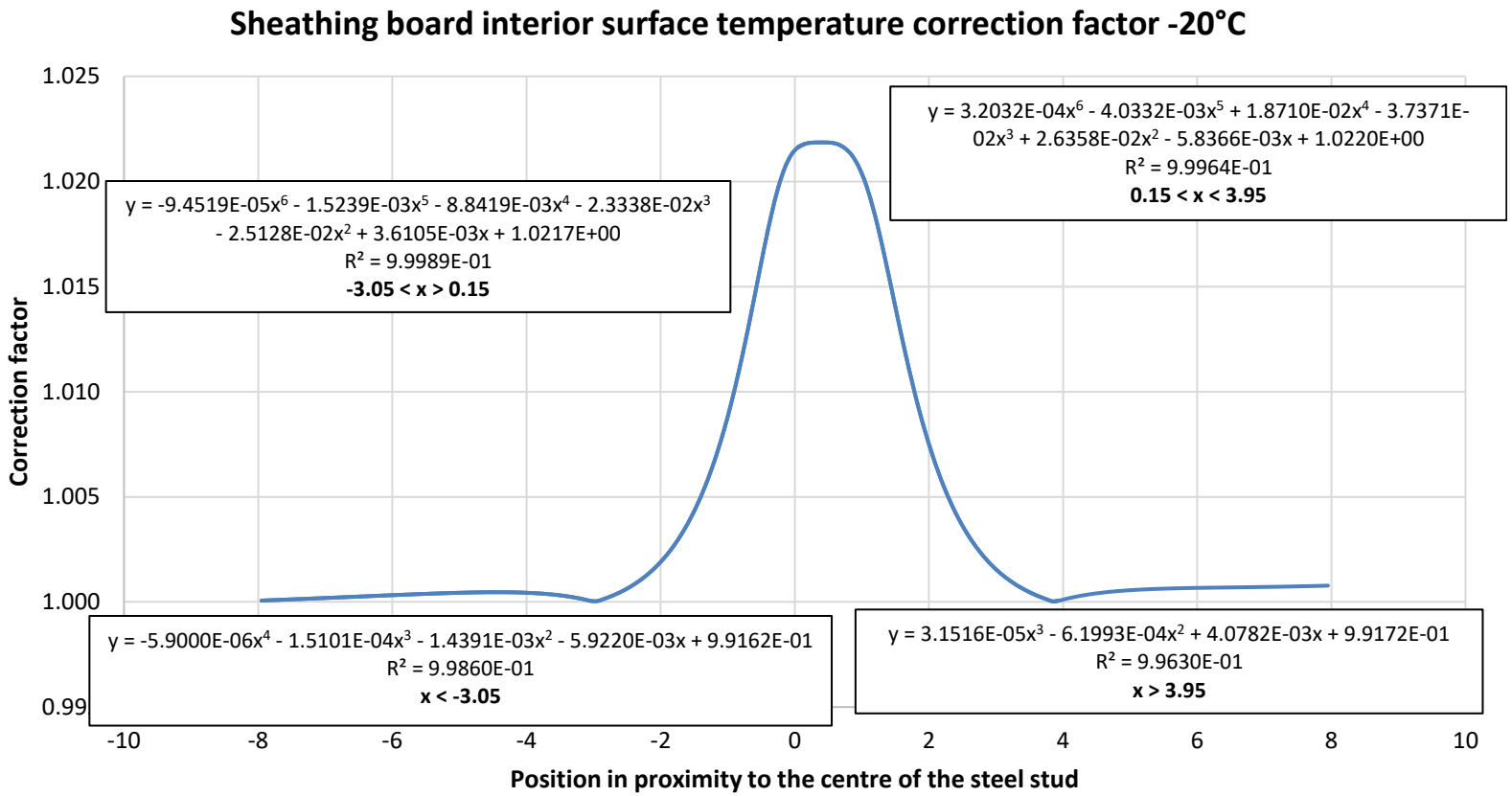


**Figure 89: Interior sheathing board surface temperature correction factor correlations for -20°C 3D simulations**

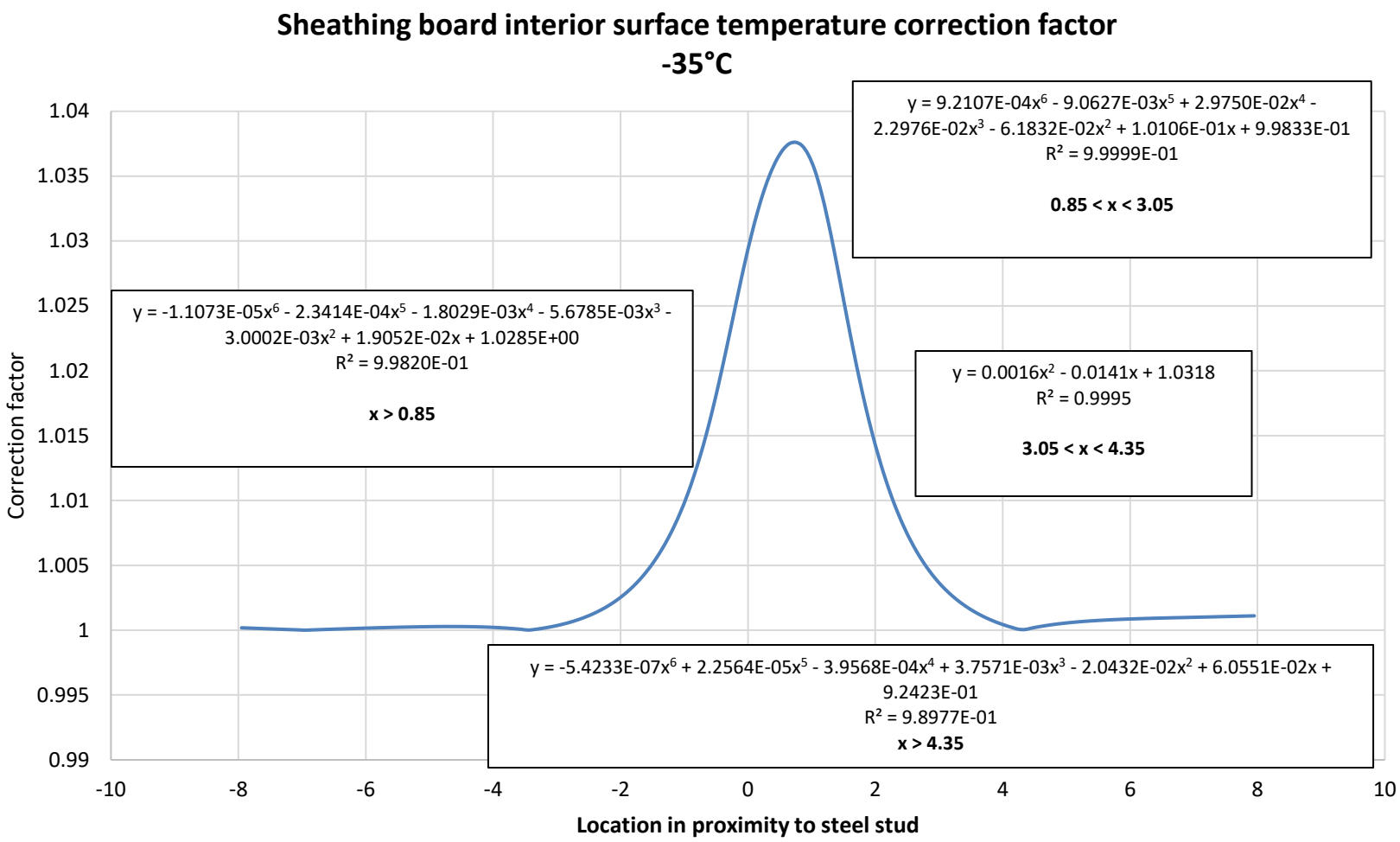


**Figure 90: Interior sheathing board surface temperature correction factor correlations for -35°C 3D simulations.**

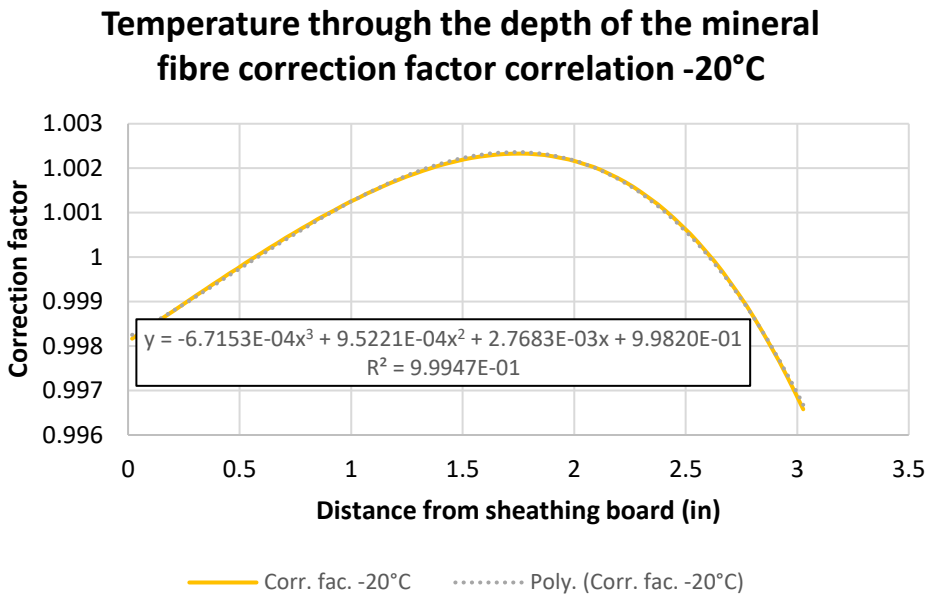


**Figure 91: Correction factor correlations for the temperature through the depth of the mineral fibre for the -20°C 3D simulations.**

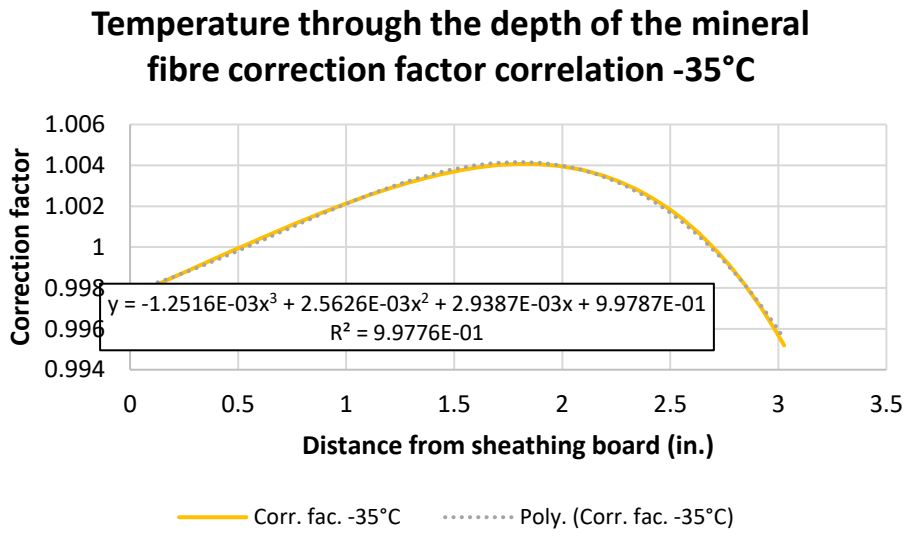


**Figure 92: Correction factor correlations for the temperature through the depth of the mineral fibre for the -35°C 3D simulations.**